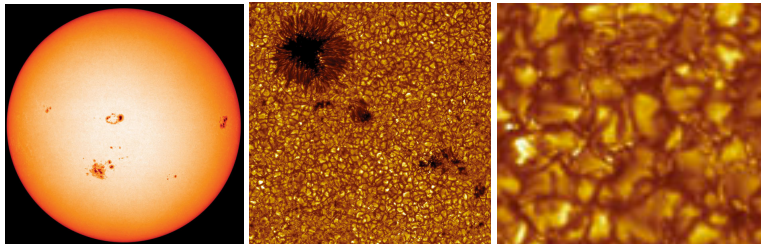


SOLAR SURFACE MAGNETISM:

SELECTED TOPICS



Irina Thaler

Image Cover: credits to Royal Swedish Academy of Sciences/Oddbjorn Engvold, Jun Elin Wiik, Luc Rouppe van der Voort, Institute of Theoretical Astrophysics of Oslo University

SOLAR SURFACE MAGNETISM: SELECTED TOPICS

ACADEMISCH PROEFSCHRIFT

ter verkrijging van de graad van doctor
aan de Universiteit van Amsterdam
op gezag van de Rector Magnificus
prof. dr. D.C. van den Boom
ten overstaan van een door het college voor promoties
ingestelde commissie,
in het openbaar te verdedigen in de Agnietenkapel
op donderdag 11 september 2014, te 14:00 uur

door

Irina Thaler

geboren te Kufstein, Oostenrijk

Promotor: prof. dr. H. C. Spruit

Overige leden: prof. dr. M. B. M. van der Klis
prof. dr. E. P. J. van den Heuvel
prof. dr. R. A. M. J. Wijers
dr. A. L. Watts
dr. J. Vink
prof. dr. M. Schüssler

Faculteit Natuurwetenschappen, Wiskunde en Informatica

This thesis is dedicated in loving memory to

my grandmother Klara Thaler

and to my parents,

Margrita Thaler and Georg Huber

*"Wir alle haben einmal unser Leben vorausgesehen. Unser geglüccktes Leben. Seitdem
tasten wir mit blinder Sehnsucht durch die Zeit."*
- ROBERT SCHNEIDER

Contents

1	Introduction	1
1.1	Magnetic Field Generation on the Sun	1
1.1.1	Global dynamo action- The solar cycle	1
1.2	Local Dynamo Action on the Solar Surface?	4
1.3	The Total Solar Irradiance Variation due to Magnetic Structures on Solar Surface	5
1.4	Sunspots	6
1.4.1	Life time of a sunspot?	7
1.4.2	What causes a sunspot to have a penumbra?	8
1.5	Summary of main results	9
2	Brightness of the Sun's small scale magnetic field: proximity effects	13
2.1	Brightness variation of the Sun	13
2.2	Causes of brightness variation	14
2.2.1	Observations	14
2.2.2	Simulations	15
2.3	Brightness of magnetic structures and their environment	16
2.3.1	Origin of magnetic brightenings	16
2.3.2	Dark rings and dark lanes	17
2.4	Calculations	19
2.4.1	Numerical methods	19
2.4.2	Setup	20
2.5	Results	21
2.5.1	Sources of darkening	23
2.5.2	Resolution dependence	27
2.5.3	Vertical velocities	27
2.6	Discussion and conclusions	28
3	Flux canceling in 3D radiative MHD simulations	39
3.1	Introduction	40
3.2	Three-dimensional magnetic fields	41

3.2.1	‘flux canceling’	42
3.2.2	Simulations	45
3.3	Calculations	45
3.3.1	Numerical methods	45
3.3.2	Setup	46
3.3.3	Analysis	49
3.4	Results	50
3.4.1	Initial vertical magnetic field with uniform $ B_z = 50$ G	50
3.4.2	Initial magnetic field fragmented into kG flux tubes	53
3.4.3	Dependence on initial field strength	54
3.5	Discussion and conclusions	56
4	Small Scale dynamos on the solar surface: dependence on magnetic Prandtl number	63
4.1	Introduction	64
4.2	Dynamos, fluctuating and non-, at low Pr_m	65
4.2.1	Transient behavior	66
4.2.2	Experimental evidence	67
4.2.3	Indications of solar small-scale dynamo action	67
4.3	Calculations	68
4.3.1	Numerical methods	68
4.3.2	Setup	69
4.3.3	Implementation of the magnetic Prandtl parameter in the STAGGER code	69
4.4	Results	71
4.5	Discussion and Conclusions	72
4.5.1	Relation between intrinsically weak and strong surface fields	73
4.5.2	Role of an imposed weak net flux	74
5	Sunspots	77
5.1	Why sunspots are interesting?	77
5.2	How do sunspots look below the surface- the anchoring problem	77
5.2.1	How do sunspots appear at the photosphere?	78
5.2.2	Sunspot modeling	80
5.2.3	Life time of a sunspot in simulations	80
5.3	Additional boundary force increases stability of a sunspot?	81
5.3.1	Numerical Methods	81
5.3.2	Set-up	82
5.3.3	Results and Discussion	84

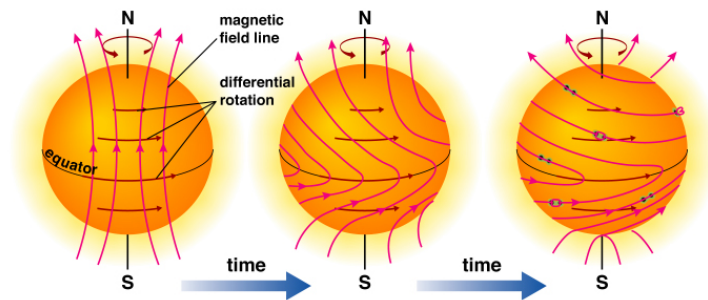
5.4	What causes a sunspot to have a penumbra?	88
5.4.1	Does a perturbation of the magnetic field in convection zone trigger the formation of a penumbra in the photosphere? . . .	89
5.4.2	Perturbation force description	89
5.4.3	Results and Discussion	90
	Nederlandse Samenvatting	97
	Acknowledgments	105

Chapter 1

Introduction

1.1 MAGNETIC FIELD GENERATION ON THE SUN

1.1.1 Global dynamo action- The solar cycle



Copyright © Addison Wesley

Figure 1.1: Illustration of solar cycle. left: initial start from a poloidal field, middle: winding up of magnetic field lines due to differential rotation, right: emergence of magnetic flux tubes due to Parker instability. after reversal of the toroidal field to the poloidal field due to the α -effect the cycle starts again with the left picture.

Observations show that the unsigned value of the magnetic flux varies by a factor of 3 from solar minimum to solar maximum and 95% of it is concentrated in the first 40°

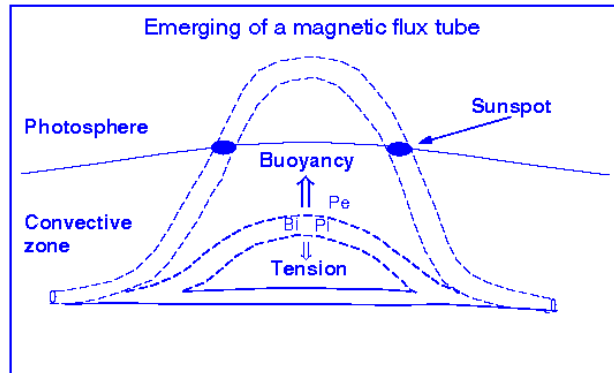


Figure 1.2: Flux tube emergence from the bottom of the convection zone when magnetic buoyancy overcomes magnetic tension force

equatorward (Howard 1974, Howard & Labonte 1981). This corresponds to a variation in the number of sunspots observed over this time period. The first sunspots in a cycle form at relatively high latitudes, then they appear at lower latitudes, so that at the end of the solar cycle they emerge close to the equator. Sunspots come in pairs, while the sunspot located in the northern hemisphere has the opposite polarity as the corresponding sunspot in the southern hemisphere. In the following solar cycle the polarities are reversed ('Hale's law'). Therefore the magnetic activity cycle is twice the sunspot cycle, so around 22 yr. These observations asked for a theoretical explanation. Here we focus on the approach taken by the conceptual dynamo models mainly developed by Babcock (1961) and Leighton (1969) as illustrated in Figure 1.1. The main problem in solar dynamo theory is how to convert a poloidal field into a toroidal one and vice versa in periodic way. Parker (1955b) pointed out that a dipole field can be regenerated in a rotating sphere due to the fact that uprising convection cells expand horizontally so that the Coriolis force rotates them clockwise in the northern hemisphere and counterclockwise in the southern hemisphere. This leads to a conversion of a poloidal into a toroidal field and vice versa. A toroidal field can additionally be produced by differential angular rotation with latitude ('differential rotation'). Babcock (1961) described the solar cycle in four stages, starting from an initial dipolar field, which due to differential rotation winds up field lines. Now it is generally agreed that this has to happen at the base of the convection zone, since from helioseismology it is known that in the radiative zone rotation is homogenous at all latitudes (Beck 2000) and in the convection zone no magnetic field could be stored due its unstable stratification. Since the density in-

side a magnetic flux tube is lower than in the non-magnetic surroundings, the magnetic flux tube rises when magnetic buoyancy is large enough to overcome magnetic tension forces, as pictured in Fig.1.2. This is the case if the length of the magnetic flux tube is exceeding twice the scale height of the medium (Parker 1955a). The field strength at which the magnetic flux tube is expected to become unstable has been shown in numerical simulations to be $10^5 G$ (Schüssler et al. 1994). This is also the field strength expected from 1D calculations using the thin flux approximation (Caligari et al. 1995, D'Silva & Choudhuri 1993) to have the correct time scale of emergence as well as the correct heliographic-latitude range and tilt of active-region axes (Caligari et al. 1998).

According to Babcock the reversal of the dipolar field takes place due to the poleward migration of the following polarity sunspot, which is closer to the poles (a consequence of the α -effect), where it neutralizes the existing flux and sets the initial field for the new cycle.

The time scale of the solar cycle is set by the time over which a certain amount of magnetic flux emerges and how long it takes for it to disappear again. From observations it is known that once there, the magnetic flux disappears from view again within about 10 days (Howard & Labonte 1981). There are several reasons for flux disappearance. Observationally magnetic flux is already undetectable if there is sufficient mixing of opposite polarity magnetic field within an area which can spatially not be resolved by current instruments. The physical reasons for flux canceling are either that the magnetic field is dragged below the surface by the convective flow ('submergence'), or that the magnetic field lines of opposite polarity get close enough to each other to reconnect. The process of magnetic flux canceling on the solar surface has commonly been mathematically described as a diffusion process. In this picture magnetic field lines of one polarity diffuse due to the advection by the random motion of the convective flow into a region of opposite polarity, like molecules of one species would diffuse and therefore mix with molecules of another species due to the Brownian motion. This approach has certainly its limitations, since it treats the magnetic field as a passive scalar advected by the fluid. Nevertheless it is a commonly used working assumption with which one can derive a diffusion coefficient for the magnetic flux canceling. The observationally measured range of diffusion coefficients determined in that way reaches from $\eta \approx 60 \text{ km}^2 \text{ s}^{-1}$ (Berger et al. 1998) to $600 \text{ km}^2 \text{ s}^{-1}$ (Sheeley 1992). This wide range of measured values suggests that in the picture of a random fluid motion determining the magnetic flux canceling process something might be missing. As magnetic fields have no ends they extend below the photosphere and are very likely to be anchored to the bottom of the convection zone. The influence of this 'anchoring' effect on the magnetic flux canceling process is studied with 3D MHD simulations extending to different depths in Chapter 3. Furthermore the influence of the initial field strength on the time scale of the magnetic flux canceling is investigated there.

1.2 LOCAL DYNAMO ACTION ON THE SOLAR SURFACE?

Livingston & Harvey (1971) discovered an intrinsically weak small-scale internetwork field on the Sun. It is spread approximately uniformly across the solar disk, and seems to be independent of the solar cycle. Durney et al. (1993) and Petrovay & Szakaly (1993) suggested that this component is produced by small scale dynamo action, locally near the solar surface. Local dynamo action means a magnetic field amplification without the need of any shear or differential rotation but only due to the convective motion of the fluid itself. Alternatively, the weak field component could represent fragments of active regions rising through the convection zone, or being a by-product of the decay of active regions (e.g. Spruit et al. 1987). In this 'decay' hypothesis a correlation between the quiet sun magnetic field and the solar cycle would be expected. The fact that this is not evident in the observations would therefore require that the decay from the large scale magnetic field to the smallest scales exceeds the solar cycle time, in this interpretation. Parnell et al. (2009) find that the magnetic flux distribution between $10^{17} - 10^{23}$ Mx can be described by a single power law function. This would indicate that the whole field is produced by the same process. Since weak fields tend to be compressed to strong fields by the granulation flow, there is the possibility that (some fraction of) the intrinsically strong small scale magnetic field, which is also observed to be unrelated to the sunspot cycle, results from a small scale dynamo mechanism.

The origin and possible variation of the strong field component is of special interest due to its brightness contribution to the Total Solar Irradiance (Schnerr & Spruit 2011, Foukal et al. 2006, Afram et al. 2011, Thaler & Spruit 2014a), and it will be further discussed in Section 1.3 and in Chapter 2.

Local dynamo action is taking place if the magnetic field amplification by fluid motion is larger than the magnetic diffusion counteracting it, but in the limit of large conductivity both of them are exponentially growing processes and which of them wins, is hard to estimate (Finn & Ott 1988). It has been only recently been acknowledged that macroscopic MHD behavior could actually depend on the fluid properties. These can be described by the magnetic Prandtl number Pr_m , which is defined as the ratio of viscosity over magnetic diffusivity or in other words the magnetic Reynolds number R_m divided by the Reynolds number Re . The reason for the strong dependence on Pr_m has been discussed in terms of the ordering of the viscous and resistive length scales (cf. Moffatt 1961). For $Pr_m \gg 1$, the viscous length scale, where the field stretching takes place, is much larger than the resistive one, which plays then a negligible role (Batchelor 1950, Schekochihin et al. 2004). The situation is quite different for $Pr_m \ll 1$, when the resistive scale is much larger than the viscous scale. The latter one is the regime present on the solar surface, since the magnetic Prandtl number there is 10^{-5} . On earth these conditions are not easily reproducible, not in laboratory experiments

nor in numerical simulations. In liquid sodium experiments by Monchaux et al. (2007) dynamo action has been achieved for the relevant Pr_m , but using a much lower magnetic Reynolds number of $R_m \approx 50$ than present on the sun ($R_m \approx 10^{12}$), furthermore the experimental setup might have influenced the results (further explanation given in Chapter 4). For incompressible MHD simulations with a flow generated by an randomly acting external large scale force, Schekochihin et al. (2007) were able to obtain dynamo action down to $Pr_m \approx 0.1$, but the growth rate is still declining going to lower Pr_m . Magnetic Prandtl numbers $Pr_m \approx 1$ are accessible with realistic 3D MHD solar surface simulations, and for these values small scale dynamo action has been found (Vögler, & Schüssler 2007, Pietarila Graham et al. 2010). In terms of dynamo behavior, $Pm = 1$ still belongs to the large magnetic Prandtl number limit, however. A range in magnetic Prandtl numbers and Reynolds R_m have been investigated in their paper, but results were still somewhat inconclusive for the combination of large R_m and small Pr_m . In view of the inconclusive results discussed above, the question whether low- Pr_m small scale dynamo action is to be expected on the solar surface is still open. In Chapter 4 we follow up on these results, explicitly testing the dependence of local dynamo action on the magnetic Prandtl parameter Pr_m for realistic solar surface simulations.

1.3 THE TOTAL SOLAR IRRADIANCE VARIATION DUE TO MAGNETIC STRUCTURES ON SOLAR SURFACE

As illustrated in Figure 1.3, the brightness of the Sun (Total solar irradiance at earth orbit, TSI) varies over its 11-yr magnetic cycle by around 0.08% (Foukal et al. 2006) due to the brightness contribution of the magnetic features on its surface. This variation is too small to have a direct effect on the Earth's climate. Magnetic brightness changes of both signs are present (reduction in spots and pores, increase in small structures); their net effect on TSI cancels to about 80%, with a small positive increase remaining. Since there is no theory for what determines the relative surface coverage of dark and bright magnetic structures, the current theoretical understanding of brightness mechanisms is still insufficient for extrapolations of the TSI record to the past or to the future. In addition to the magnetic structures related to solar cycle, there are small scale magnetic features (diameter around 200 km) of an intrinsically strong magnetic field component present on the solar surface, which are thought to be independent of the solar cycle and are maybe produced by local dynamo processes as already mentioned in Section 1.2 and further described in Chapter 4. Its brightness contribution to the total TSI has been estimated to be 0.15% in an elaborate study by (Schnerr & Spruit 2011) using data taken with the Swedish Solar Telescope. About the possible long term variation of the

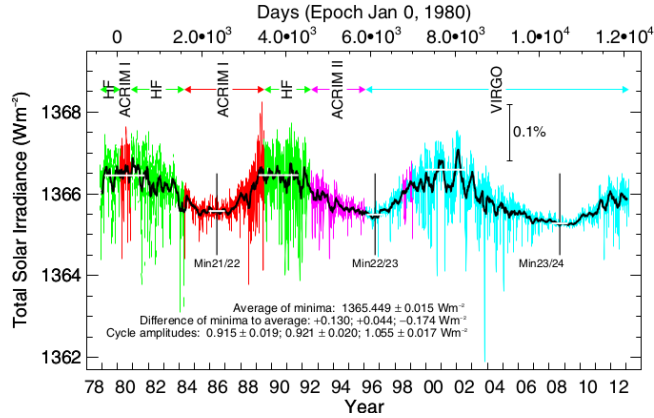


Figure 1.3: Total Solar Irradiance variation measured by radiometers on different space platforms (ACRIM, HF, VIRGO). Figure taken from Physikalisch-Meteorologisches Observatorium Davos (PMOD), World Radiation Center

intrinsically strong small scale magnetic field is not much known, since the small scale magnetic field has only recently been resolved in observations and direct measurements of the Sun's global output (with space based instruments) are available only for the past 30 years. A systematic trend over this period, if present, is below the variation between individual cycles. Therefore it would be useful to determine the brightness contribution of the small scale magnetic field currently present on the sun, so that one could guess if its possible variation could significantly change the TSI and as a consequence influence the Earth's climate. As one project of this Phd thesis the brightness contribution of this small scale magnetic structures has been investigated by the means of realistic solar surface simulations as described in Chapter 2.

1.4 SUNSPOTS

As strong magnetic features sunspots are easy detectable indicators of global solar dynamo processes and as their temperature is around 2000K below the average solar surface temperature, sunspots directly influence the total solar irradiance. Though the current variations of the total solar irradiance during on sunspot cycle are not large enough to have any direct effect on the earth's climate, as already pointed out in Section 1.3, we do not understand solar cycle processes well enough to extrapolate to the past

or future. And therefore, understanding what determines the life time of a sunspot as well as what determines their ratio between penumbra/umbra is inevitable to be able to predict solar irradiance variations.

Recently it has become possible to perform realistic 3D MHD simulations with a realistic equation of state of pores (Bercik et al 2003, Cameron et al. 2007, Kitiashvili et al. 2010) as well as of a sunspot umbra (Schüssler & Vögler 2006), stripes of sunspots (Heinemann et al. 2007, Rempel et al. 2009b) as well as of whole sunspots (Rempel et al. 2009a, Rempel 2011b). As further described in Chapter 5, we also performed 3D MHD simulations of sunspot stripes to investigate two different scientific questions further described below.

1.4.1 Life time of a sunspot?

As magnetic fields are divergence-free, field lines have no ends and are intrinsically three-dimensional. This means field lines continue above and below the observed surface. The commonly accepted picture about how a sunspot looks like below the surface, is that it persists as one magnetic flux tube, which is anchored at the base of the convection zone (already implicit in Cowling 1953, and developed by Babcock 1963, Leighton 1969, Spruit & Roberts 1983). What limits then its life time, are fluting instabilities which lead to nonmagnetic material to enter the sunspot area and finally disperse the sunspot. In realistic 3D MHD sunspot simulations the dispersion of a sunspot is faced earlier than in observations because simulation boxes have typically vertical extensions of 1/20 of the convection zone layer or less. Since the convective time scale increases with depth, this means that in simulations the magnetic flux tube is anchored at a altitude level where the convective time scale is much shorter than at the base of the convection zone and therefore the destruction of the sunspot is expected earlier than observed on the sun. Current sunspot models are very successful in describing the sunspot fine structure at the photosphere. Nevertheless many questions considering their subsurface structure, as the origin of the moat flow, which is a large scale outflow surrounding sunspots on a photospheric level, first discovered by Sheeley (1969), Harvey & Harvey (1973), and its possible connection to the Evershed flow, are still open. This is connected to the fact that commonly used simulation times of 3-8h (Rempel 2011a, Rempel 2012, Rempel et al. 2009a, Rempel et al. 2009b) are too short for this flow patterns to develop without the influence of the initial set-up. It has been shown by Rempel (2011b), that a vertical extension of the simulation box does prolong the life time of a sunspot, but this goes at the cost of much higher computational power. Following up this idea, in Chapter 5 we investigated the question, if an additional force at the lower boundary holding the magnetic field lines together, prolongs the life time

of the sunspot, while the computational expense stays the same.

1.4.2 What causes a sunspot to have a penumbra?

Sunspots vary a lot in their form and size. They can extend to a diameter of 50Mm or more where the umbra, the central dark area, is usually contributing around 20% to the total spot diameter. The penumbra is seen as a brighter ring surrounding the dark umbra, having around 75 % of the heat flux of the normal granulation, leading to a temperature of 5275K. Although lots of observations are available from this region, there is still a lot of debate going on about the theoretical understanding of the penumbra structure based on observations. The reason for that are rapid changes of the inclination angle of the magnetic field (Beckers & Schröter 1969; Lites et al. 1990; Schmidt et al. 1992; and Title et al. 1993) as well as of the Evershed flow with depth (Sanchez Almeida & Lites 1992). The smallest sunspots having primitive penumbras have fluxes of 2×10^{20} Mx and radii of only 1.8Mm, but there are as well examples of pores which survive to radii up to 3.5Mm and magnetic fluxes of 7×10^{20} Mx. This means there is a regime of magnetic fluxes and radii for which both pores and sunspots exist, though most of the pores with $R > 2$ Mm develop a penumbra (Bray & Loughhead 1964). To understand under which circumstances a sunspot gets a fully developed penumbra and when it stays a pore, is not only interesting from a basic physics point of view. Total solar irradiance reconstructions use total sunspot areas and assume a constant penumbra/umbra ratio (Foukal & Lean 1990). If this assumption is not valid, there might be consequences for solar cycle theory, solar irradiance reconstruction and for the penumbra formation theory. Therefore it would be good to have a more profound theoretical understanding of the conditions under which a penumbra forms and on what its horizontal extension depends on. (Simon & Weiss 1970, Spruit 1976, Simon et al. 1983) had developed pore models which assume that as soon as the magnetic flux increases, the magnetic field gets more inclined towards the vertical and finally forms a penumbra. Rucklidge et al. (1995) assume that at some critical value θ_c and some critical radius, any perturbation of the pore leads to the formation of a penumbra because then its the only stable solution. It is indicated by observations, that the subsurface structure of a sunspot does influence its behavior, since it has been shown that larger sunspots are moving around a bit in longitude and latitude (Gizon et al. 2009, Gizon et al. 2010) before they stabilize at a certain position which can take a few days (Mazzucconi et al. 1990). The observed settling process is often interpreted as notion of anchoring in deep layers (Moradi et al. 2010). Following this idea, it could be that perturbations of the magnetic field in the subsurface of the sunspot trigger the formation of a penumbra. This hypothesis has been investigated in Chapter 5 by performing a 3D MHD

simulation of a sunspot and testing the influence of an additional force perturbing the magnetic field deeper down in the convection zone.

1.5 SUMMARY OF MAIN RESULTS

- **Brightness contribution of the small scale magnetic field on the sun:** The photospheric quiet sun magnetic field is contributing $\Delta F = (-0.34 \pm 0.07)\%$ to the total bolometric flux. Realistic 3D solar surface simulations performed by Thaler & Spruit (2014a), identified indirect brightness contributions such as the suppression of convection nearby magnetic obstacles, which have recently also been detected in observations (Kobel et al. 2012), and the dark ring effect as dominating over the positive direct brightness contribution of the magnetic structures themselves.
- **Magnetic Flux canceling on the solar surface:** The time scales involved in the disappearance of magnetic flux between regions of opposite polarity on the solar surface depend on the magnetic field strength. This is due to the fact that the attractive magnetic force increases with the field strength, which leads to reconnection and magnetic retraction of the magnetic field below the surface.
- **Magnetic Flux canceling on the solar surface:** Though the intrinsic kG strength magnetic field concentrations connects the surface to deeper layers by magnetic forces and one would expect that the depth of the anchoring of the magnetic field influences the flux disappearance process, only a very mild influence on the effective rate of magnetic flux canceling has been found.
- **Small scale dynamo action at low magnetic Prandtl numbers:** Studying magnetic field amplification as a function of the numerical magnetic Prandtl parameter Pr_m in realistic solar surface simulations showed that at a Pr_m of around one a shut down of dynamo action takes place. This does not crucially depend on numerical resolution, which can be used as a proxy for the Reynolds number.
- **Small scale dynamo action at low magnetic Prandtl numbers:** In our realistic solar surface simulations where local dynamo action was taking place, no evidence was found that a compression of the generated weak magnetic field component leads to the strong magnetic field component. This is probably due to the fact, that the field is of mixed polarity, so that further compression would lead to flux canceling.

REFERENCES

- Afram, N., Unruh, Y. C., Solanki, S. K., Schüssler, M., Lagg, A., Vögler, A. 2011, *A&A*, 526, A120
- Babcock, H. W., 1961, *ApJ*, 133, 572
- Babcock, H. W., 1963, *ARA&A*, 1, 41
- Batchelor, G. K., 1950, *Royal Society of London Proceedings Series A*, 201, 405-416
- Beck, J. G., 2000, *Sol. Phys.*, 191, 47-70
- Beckers, J. M., Schröter, E. H., 1969, *Sol. Phys.*, 10, 384-403
- Bercik, D. J., Nordlund, A., Stein, R. F., 2003, *ESA Special Publication*, 517, 201-206
- Berger, T. E., Löfdahl, M. G., Shine, R. A., Title, A. M., 1998, *ApJ*, 506, 439-449
- Bray, R. J., Loughhead, R. E., 1964, *Sunspots*
- Caligari, P., Moreno-Insertis, F., Schussler, M. 1995, *ApJ*, 441, 886-902
- Caligari, P., Schuessler, M., Moreno-Insertis, F. 1998, *ApJ*, 502,481
- Cameron, R., Schüssler, M., Vögler, A., Zakharov, V., 2007, *A&A*, 474, 261-272
- Cowling, T. G., 1953, *Solar Electrodynamics*, ed. G. P. Kuiper, 532
- Durney, B. R. , De Young, D. S., Roxburgh, I. W., 1993,*Sol. Phys.*, 145, 207-225
- Finn, J. M. & Ott, E., 1988, *Phys. Rev. Lett.*, 60, 760-763
- Foukal, P. & Lean, J., 1990, *Science*, 247, 556-558
- Foukal, P., Fröhlich, C., Spruit, H., Wigley, T. M. L., 2006, *Nature*, 443, 161-166
- Gizon, L., Schunker, H., Baldner, C. S. , Basu, S., Birch, A. C., Bogart, R. S., Braun, D. C., Cameron, R., Duvall, T. L., Hanasoge, S. M., Jackiewicz, J., Roth, M., Stahn, T. ,Thompson, M. J., Zharkov, S., 2009, *Space Sci. Rev.*, 144, 249-273
- Gizon, L., Schunker, H., Baldner, C. S. , Basu, S., Birch, A. C., Bogart, R. S., Braun, D. C., Cameron, R., Duvall, T. L., Hanasoge, S. M., Jackiewicz, J., Roth, M., Stahn, T. ,Thompson, M. J., Zharkov, S., 2010, *Space Sci. Rev.*, 159, 257-258
- Harvey, K., Harvey, J., 1973, *Sol. Phys.*, 28, 61-71
- Heinemann, T., Nordlund, Å., Scharmer, G. B., Spruit, H. C., 2007, *ApJ*, 669, 1390-1394
- Howard, R. 1974, *Sol. Phys.*, 38, 59-67
- Howard, R., Labonte, B. J. 1981, *Sol. Phys.*, 74, 131-145
- Kitiashvili, I. N., Kosovichev, A. G., Wray, A. A., Mansour, N. N., 2010, *ApJ*, 719, 307-312
- Kobel, P., Solanki, S. K., & Borrero, J. M. 2012, *A&A*, 542, A96
- Leighton, R. B., 1969, *ApJ*, 156, 1
- Lites, B. W., Skumanich, A. , Scharmer, G. B., 1990, *ApJ*, 355, 329-341
- Livingston, W. & Harvey, J., 1971, *IAU Symposium*, 43, 51
- Mazzucconi, F ,Coveri, C., Godoli, G., 1990, *Sol. Phys.*, 125, 269-276
- Moffatt, H. K., 1961, *Journal of Fluid Mechanics*, 11, 625-635

- Monchaux, R., Berhanu, M., Bourgoïn, M., Moulin, M., Odier, P., Pinton, J.-F., Volk, R., Fauve, S., Mordant, N., Pétrélis, F., Chiffaudel, A., Daviaud, F., Dubrulle, B., Gasquet, C., Marié, L., Ravelet, F., 2007, *Phys. Rev. Lett.*, 98, 044502
- Moradi, H., Baldner, C., Birch, A. C., Braun, D. C., Cameron, R. H., Duvall, T. L., Gizon, L., Haber, D., Hanasoge, S. M., Hindman, B. W., Jackiewicz, J., Khomenko, E., Komm, R., Rajaguru, P., Rempel, M., Roth, M., Schlichenmaier, R., Schunker, H., Spruit, H. C., Strassmeier, K. G., Thompson, M. J., Zharkov, S., 2010, *Sol. Phys.*, 267, 1-62
- Parker, E. N., 1979, *ApJ*, 234, 333-347
- Parker, E. N., 1955, *ApJ*, 121, 491
- Parker, E. N., 1955b, *ApJ*, 122, 293
- Parnell, C. E., DeForest, C. E., Hagenaar, H. J., Johnston, B. A., Lamb, D. A., Welsch, B. T., 2009, *ApJ*, 698, 75-82
- Petrovay, K. & Szakaly, G., 1993, *A&A*, 274, 543
- Pietarila Graham, J., Cameron, R., Schüssler, M., 2010, *ApJ*, 714, 1606-1616
- Rempel, M., Schüssler, M., Cameron, R. H., Knölker, M., 2009a, *Science*, 325, 171
- Rempel, M., Schüssler, M., Knölker, M., 2009b, *ApJ*, 691, 640-649
- Rempel, M., 2011a, *ApJ*, 729, 5
- Rempel, M., 2011b, *ApJ*, 740, 15
- Rempel, M., 2012, *ApJ*, 750, 62
- Rucklidge, A. M., Schmidt, H. U., Weiss, N. O., 1995, *MNRAS*, 273, 491-498
- Sanchez Almeida, J., Lites, B. W., 1992, *ApJ*, 398, 359-374
- Schekochihin, A. A., Cowley, S. C., Taylor, S. F., Maron, J. L., McWilliams, J. C., 2004, *ApJ*, 612, 276
- Schekochihin, A. A., Iskakov, A. B., Cowley, S. C., McWilliams, J. C., Proctor, M. R. E., Yousef, T. A., 2007, *New Journal of Physics*, 9, 300
- Simon, G. W. & Weiss, N. O., 1970, *Sol. Phys.*, 13, 85-103
- Simon, G. W., Weiss, N. O., Nye, A. H., 1983, *Sol. Phys.*, 87, 65-75
- Schmidt, W., Hofmann, A., Balthasar, H., Tarbell, T. D., Frank, Z. A., 1992, *A&A*, 264, L27-L30
- Schnerr, R. S., & Spruit, H. C. 2011, *A&A*, 532, A136
- Schüssler, M., Caligari, P., Ferriz-Mas, A., Moreno-Insertis, F., 1994, *A&A*, 281, L69-L72
- Schüssler, M., Vögler, A., 2006, *ApJ*, 641, L73-L76
- Sheeley, Jr., N. R., 1969, *Sol. Phys.*, 9, 347-357
- Sheeley, N.R., 1992, *A.S.P. Conf. Series*, 27, 562
- Spruit, H. C., 1976, *Sol. Phys.*, 50, 269-295
- Spruit, H. C., Roberts, B., 1983, *Nature*, 304, 401-406
- Spruit, H. C., Title, A. M., van Ballegoijen, A. A., 1987, *Sol. Phys.*, 110, 115-128
- Title, A. M., Frank, Z. A., Shine, R. A., Tarbell, T. D., Topka, K. P., Scharmer, G., Schmidt, W., 1993, *ApJ*, 403, 780-796

Thaler, I. & Spruit, H. C. 2014a, A&A in press

Vögler, A., Schüssler, M., 2007, A&A, 465, L43-L46

Chapter 2

Brightness of the Sun's small scale magnetic field: proximity effects

Irina Thaler & H. C. Spruit

A&A, accepted, 2014

2.1 BRIGHTNESS VARIATION OF THE SUN

The brightness of the Sun (Total solar irradiance at earth orbit, TSI) varies over its 11-yr magnetic cycle, by an amount of order 0.08% (cf. Fröhlich 2006). Such a variation is too small to have a direct effect on the Earth's climate, even if in addition to the 11-yr cyclic variation there were a systematic effect of this order sustained over centuries. Direct measurements of the Sun's global output (with space based instruments) are available only for the past 30 years, however. A systematic trend over this period, if present, is below the variation between individual cycles. This has raised the question whether the cause of variation is understood well enough to extrapolate the effects detected so far to longer time scales in the past and into the future. The mechanisms by which magnetic fields influence the brightness of the solar surface have been known qualitatively for several decades (Spruit 1977, hereafter S77, Chiang & Foukal 1983, Spruit 1991). Detailed quantitative understanding has now become possible through advances in realistic 3D numerical MHD simulations of magnetic surface structures such as sunspots and small scale magnetic fields structures (Carlsson et al. 2004, Keller et al. 2004, Steiner 2005, Pietarila Graham et al. 2009). Magnetic brightness changes of both signs are present (reduction in spots and pores, increase in small structures); their net effect on TSI cancels to about 80%, with a small positive increase remaining. Since

there is no theory for what determines the relative surface coverage of dark and bright magnetic structure, the current theoretical understanding of brightness mechanisms is still insufficient for extrapolations of the TSI record. Irrespective of this uncertainty, a good grasp of the brightness of the small scale magnetic field, as the main contributor to TSI variation, is called for. In addition to the known mechanisms that cause small magnetic structures to increase the bolometric brightness of the solar surface, they also have effects on their non-magnetic surroundings. Such effects have not been studied much. We call them ‘proximity effects’, and assess their possible importance for the net brightness variation of the Sun.

2.2 CAUSES OF BRIGHTNESS VARIATION

2.2.1 Observations

TSI correlates closely with identifiable magnetic structures on the surface. Composite long term records of observables such as areas covered by sunspots, active region fields and ‘active network’ statistically explain over 90% of the observed variance in TSI (e.g. Fröhlich & Lean 2004, Wenzler et al. 2006, Ball et al. 2012). This can be seen as evidence that the only detectable contribution to TSI variation are the local brightness contrasts of magnetic structures themselves, and that measurements of areas covered by these structures can thus be used as ‘proxies’ for TSI variation. The statistical success of the correlation with surface structures, however, involves adjustment of free amplitude parameters for the proxies. Since it does not provide physical explanations of the effects either, it does not have much predictive power. Its use for extrapolations outside the time span of TSI measurements is therefore uncertain. A source of concern in interpreting the TSI record are possible longer term brightness variations of the quiet surface regions that are not covered by the proxies used. At the level of sensitivity needed, brightness measurement of magnetically quiet areas is not possible from the ground, due to limited photometric accuracy. The space based measurements of TSI are sufficiently sensitive, but do not resolve any structures on the solar disk. Sufficient photometric accuracy has been achieved at $\sim 5'$ resolution by the balloon-borne Solar Bolometric Imager experiment (SBI, Foukal & Bernasconi 2008). It has not found indications for significant brightness variations outside areas covered by magnetic fields. On smaller scales, arcseconds and less, brightness contributions from the immediate nonmagnetic environment of magnetic structures might be present that have escaped detection so far. Reports of changes in granulation related to magnetic activity, for example, have a long history. Macris et al. (1955, 1984) measured a decrease of granulation size with increasing solar activity. These results

were not universally accepted, but more local changes in granulation in individual active regions are well documented. Granules appear smaller, with lower flow speeds ('anomalous' granulation, Macris 1979, Schmidt et al. 1988, Title et al. 1986, 1992, Kobel et al. 2012). A plausible cause for these differences would be geometrical constraints imposed on the convective flow by nearby magnetic structures. Given these clearly detectable changes in the morphology of granulation, it would be somewhat surprising if the mean brightness of granulation were not affected as well, at some level (Spruit 1998). One might expect that the convective heat flux would be reduced by magnetic flow constraints, for example, and granules correspondingly darker. This would constitute a complication to be accounted for in the interpretation of TSI variations. Direct detection of such effects at the required levels of a fraction of a percent is observationally quite challenging, but has recently become possible using space-based data (Kobel et al. 2012). The direct effect of magnetic fields on the other hand, i.e. the local brightness of points on the surface where a magnetic signal is present, can be measured rather reliably. At the low levels of magnetic activity in quiet network the field consists of a small-scale mixture of opposite polarities. Identifying magnetic brightness changes in such regions therefore requires high spatial resolution. A conceptually straightforward measurement consists of adding up the contributions from magnetic bright points identifiable at the available spatial resolution (Sánchez Almeida et al. 2010). This provides a lower limit since it underestimates the contribution from poorly resolved magnetic patches, and because these patches occur preferentially in regions that are darker than average: the intergranular lanes. Schnerr & Spruit (2011) present a detailed study that takes these factors into account and does not rely on a feature identification process. Some of the magnetically quietest regions were studied, where the (unsigned) magnetic flux density is about 10G. At this flux level, a net magnetic brightness increase (at 630nm) of $\approx 0.15\%$ was found at disk center in data from the Swedish 1-m Solar Telescope (resolution $0''.2$), and $\approx 0.10\%$ in lower resolution data from the Hinode satellite. These measurements only quantify the brightness in the magnetic field itself; brightness changes that might be present in the immediate nonmagnetic neighborhood of the magnetic structures are not included. The results therefore may represent *overestimates* of the magnetic brightening in quiet regions.

2.2.2 Simulations

The small scale magnetic field is one of the obvious applications of realistic 3D MHD simulations, since they need to cover only relatively small areas of solar surface. The high spatial resolution required for convergence of the numerical simulations with observations has been achievable for almost a decade (Keller et al. 2004, Carlsson et

al. 2004, Steiner 2005, de Pontieu et al. 2006). Detailed comparison with observations, e.g. in de Pontieu et al. (2006), shows the remarkable degree of agreement that realistic simulations achieve in practically all aspects of the observations at the photospheric level. This gives confidence that more subtle questions like the proximity effect of anomalous granulation are within reach with current present computational resources. The required statistical accuracy can be achieved by either simulating a sufficiently large area of magnetically affected granulation, or by following it over a sufficient number of granule life times. Afram et al (2011) studied the center-to-limb variation (CLV) of magnetic brightening of small scale magnetic structures with a realistic 3D MHD simulation. The result agrees with the qualitative predictions from the ‘flux tube’ picture above and with the observed CLV of active regions. The net effect on the (bolometric) brightness of the solar surface was not highlighted explicitly in this work. As we find below, this is probably because it is a smaller effect, for which larger areas and/or a long integration times are required than for a test of the CLV.

2.3 BRIGHTNESS OF MAGNETIC STRUCTURES AND THEIR ENVIRONMENT

2.3.1 Origin of magnetic brightenings

The reduced gas pressure in magnetic structures at the surface locally depresses the optical depth unity level (the ‘local photosphere’). This causes changes in surface brightness in two different ways. The reduced opacity causes a lateral influx of heat into the structure which starts to dominate the energy balance in sub-arcsecond size structures. Secondly, the geometric distortion of the local photospheric surface has an effect on the center-to-limb variation in surface brightness. When seen at an angle, i.e. at positions away from the center of the solar disk (Fig. 2.1), the walls of the structure are seen more nearly face-on, making them bright compared with the limb-darkened photosphere around it (the ‘bright wall effect’, Spruit 1976, hereafter S76). This explains the increase of facular contrast observed towards the solar limb. It can be interpreted as a reduction of limb darkening caused by an increase of surface roughness. Because of the geometrical nature of the effects, the details of both also depend on the size of the structure. This is illustrated in Fig. 2.1. A small structure (less than $0''.5$) at disk center is bright because of the sideways influx of radiation from the surrounding convection zone. Seen at an angle, the interior becomes obscured by the disk-center wall, while the limb side wall appears bright by its contrast with the limb-darkened surroundings. Fig. 2.4 shows the effect as seen in the numerical simulations reported below. In a

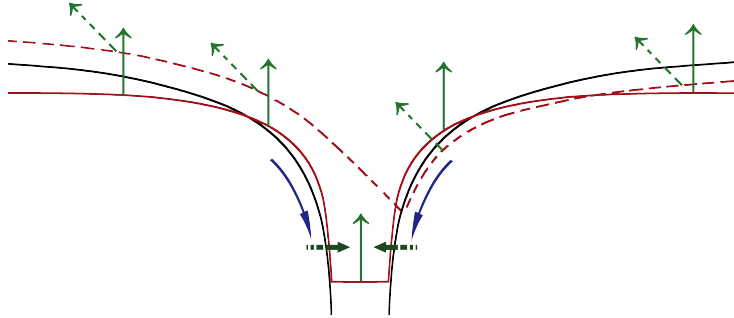


Figure 2.1: Brightness changes in and around a magnetic ‘flux tube’ (schematic). Black: boundary of the magnetic structure. Red: $\tau = 1$ surfaces for viewing angles $\mu = 1$ (solid) and $\mu = 0.7$ (dashed). Green arrows: direction of the specific intensity from the $\tau = 1$ surfaces for these angles. At $\mu = 0.7$ the ‘bright wall effect’ is visible towards the solar limb (right side of the figure), in the region where the broken line lies below the solid line. At the disk center (left) side, the interior of the tube is obscured by the wall of the tube. Lateral influx of heat into the flux tube (heavy broken arrows) cool the surroundings, causing enhanced downflow (blue arrows) around the structure.

larger structure (pore, $\sim 1''$) interference of the magnetic field with convective energy transport from below causes its center to be dark (as in sunspots). Because of its greater width, its walls flare out more nearly horizontally over its surroundings. The opacity reduction effect increases the heat flux from this region. This brightness contribution turns out to be the dominant contributor to magnetic brightening away from disk center (Steiner 2005). It explains the rather large area affected ($\gtrsim 0''.5$), compared with the small area expected from the height (~ 150 km) of the walls of a narrow flux tube (see the sketch in Fig. 2.1). See the observations at

http://www.solarphysics.kva.se/gallery/movies/2004/gband_10May2004_AR_limb.mpg. Since smaller structures self-obscure away from disk center, the main brightness contribution towards the solar limb is actually from larger structures (pores) that are dark at disk center (see this in the images at

http://www.solarphysics.kva.se/gallery/movies/2004/gcont_13May2004.avi and S76 Fig. 11).

2.3.2 Dark rings and dark lanes

The sideways radiative flux into a small magnetic structure derives in part from its immediate surroundings. This results (S76) in the presence of a ‘dark ring’ in its im-

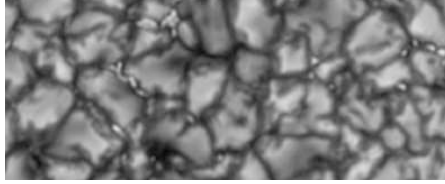


Figure 2.2: Intensity image (630 nm continuum) of small scale magnetic fields at the disk center, as seen at $\approx 0''.15$ resolution (Swedish 1-m Solar Telescope). Image width is $20'$ (14.5 Mm). The magnetic brightenings between granules are surrounded by narrow dark rims: the ‘dark ring’ effect (see Fig. 2.1 for interpretation).

mediate non-magnetic environment. The theory predicted that this compensation is only partial, such that the small scale field acts as a net leak in the surface through which an excess heat flux escapes from the convection zone (S77). The effect is predicted to be local, restricted to the immediate environment of the magnetic structures, not compensated by opposite brightness changes elsewhere on the solar surface: ‘what you see is what you get’ (S77, Chiang & Foukal 1983, S91, S97). The effect is clearly seen in high-resolution continuum images, see the example in Fig. 2.2. Quantitative assessment of the dark ring effect on the net brightness enhancement due to the magnetic field requires realistic numerical simulations. Measurement of the brightness effect of the small scale magnetic field is complicated by the fact that most of it is located in the intergranular lanes. Structures in intergranular lanes can add a positive brightness contribution even when they appear as darker than the mean nonmagnetic photosphere, at a given spatial resolution. Their effect on average brightness is determined by their contrast relative to a comparable nonmagnetic location in the intergranular lanes. The effect of this ‘dark lane bias’ can be studied quantitatively by measuring the mean brightness of pixels of a given flux density \bar{B} (absolute value of the field strength averaged over the pixel) as a function of \bar{B} . Fig. 2.3 shows this for observations made with the Swedish 1-m Solar Telescope (SST). The average (unsigned) flux density in the observation was 10 G. As expected, brightness increases with the amount of magnetic flux in the pixel, except at flux densities below 100 G, where brightness first drops as a function of \bar{B} . The shape of the curve can be understood in terms of the dark lane bias: magnetic fields congregating in intergranular lanes (in particular at the vertices between several granules). At the very lowest flux densities (below ≈ 5 G) the surface brightness is higher than the average by some 2%. This is a consequence of the fact that magnetic fields preferentially populate intergranular lanes. The very lowest fields therefore avoid the lanes somewhat, causing a bias towards regions which are

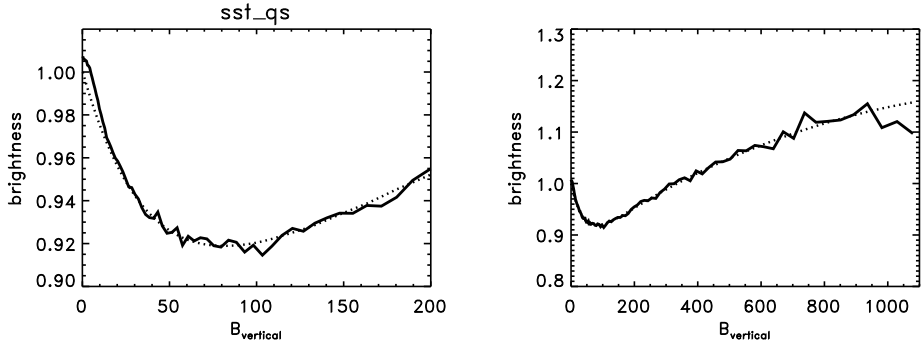


Figure 2.3: Right panel, solid line: brightness as a function of flux density in a quiet region observed at 630 nm with the SST. Dotted: model fit as described in Schnerr and Spruit 2011. Left panel: same data on an expanded scale.

brighter than average. With increasing flux density, the bias shifts towards the intergranular lanes, causing the curve to drop below the average. The trend then reverses with increasing flux density, which selects pixels centered on the bright areas of larger, resolved, structures. [At even larger flux densities the curve dips down again, because in the field studied the largest field strengths occur in even larger, darker concentrations resembling pores, cf. Frazier (1971)]. From the model fit in Fig. 2.3 the brightening can be deduced, corrected for the dark lane bias. For this observation, this yields a net magnetic magnetic of 0.15%, at a mean flux density of 11 G.

2.4 CALCULATIONS

2.4.1 Numerical methods

For the numerical simulations we used the 3d magnetohydrodynamics code STAGGER, developed by Galsgaard & Nordlund (1996). The code integrates the time-dependent magnetohydrodynamics equations with a 6th order finite difference scheme using 5th order interpolations for the spatial derivatives. The time evolution uses a 3rd order Runge-Kutta scheme. For every time step the radiative transfer equation is solved at every grid point in the three-dimensional box assuming local thermodynamic equilibrium. This is done by using a Feautrier-like scheme along the rays with two μ angles plus the vertical and four ϕ angles horizontally, which adds up to nine angles in total. The wavelength dependence of the absorption coefficient is represented by four

opacity bins. A more detailed description on the opacity binning scheme used is given in Collet et al. (2011). Further details about the code performance can be found in Beeck et al. (2012).

2.4.2 Setup

For our simulations we used a simulation box of horizontal extent 18 Mm x 18 Mm with a resolution of 25 km and a vertical extent of 3.15 Mm extending 465 km above the photosphere and 2.7 Mm into the convection zone. The grid is nonequidistant in the vertical direction, with grid spacing varying between a minimum of 7 km near the photosphere to 32 km at the lower boundary. The horizontal boundaries are periodic while the vertical boundaries are open and transmitting. The entropy of the inflowing material at the bottom boundary is fixed and the same in all three simulations. The magnetic field is kept vertical at the bottom, allowing field lines to move horizontally there. As a magnetic boundary condition a potential field is implemented at the top boundary. The purely hydrodynamic simulation run was started from an already thermally relaxed snapshot. This simulation was run for 960 min. The initial condition for the second simulation is again a thermally relaxed snapshot, taken from the nonmagnetic run, but with a uniform vertical magnetic field of 50 G added. Since the Lorentz force in this field vanishes, adding such a field is consistent with the hydrodynamic part of the initial conditions. Due to the periodic boundary conditions, the horizontal mean of the vertical field component stays constant in time at all depths. In the third simulation the uniform initial field was increased to 100 G. The initial condition in this case is a snapshot at the end of the non-magnetic run, different from that of the 50 G simulation but statistically equivalent. Since the time step in the magnetic simulations is determined by the Alfvén speed in the atmosphere, computational expense increases roughly with the initial field strength. The 50 G run was evolved for 300 min, the 100 G simulation for 120 min. Except for the initial conditions as described, the parameters controlling input physics and numerical setup are identical in all three runs.

Resolution tests

To test the resolution dependence of our results, we took one hydrodynamical snapshot from the setup described above using three different horizontal resolutions, once the standard one with 720x205x720 grid points and a horizontal resolution of $\Delta x=25$ km, once half the resolution using 360x205x360 grid points and a horizontal resolution of $\Delta x=50$ km, and once double the resolution of $\Delta x=12.5$ km using 1440x205x1440 grid

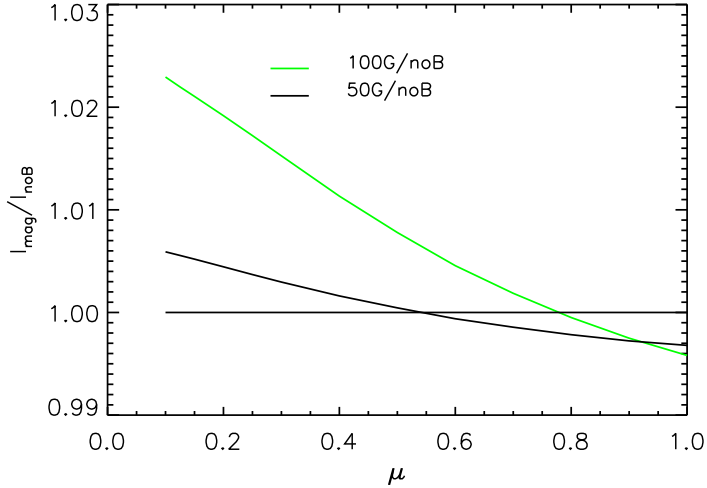


Figure 2.4: Time and area-averaged center-to-limb variation of brightness in 630 nm continuum, relative to the non-magnetic simulation.

points horizontally. For this snapshots a uniform vertical magnetic field of 50G was implemented and all three simulations were then ran for 25 min.

2.5 RESULTS

Fig. 2.6, shows a snapshot of the 100 G mean field simulation at 4 viewing angles. The smallest scales in the magnetic structures disappear from view already around $\mu = 0.82$ (35° from disk center), resulting in a somewhat fuzzier impression. The dependence on μ shows the characteristic 'bright wall effect' that becomes conspicuous at $\mu \lesssim 0.7$. Fig. 2.4 shows the center-to-limb variation of the surface-averaged continuum brightness relative to that of the nonmagnetic simulation. At least 12 snapshots taken 10 min apart of each other were used for each simulation.

The positive contrast towards the limb is as expected from the bright wall effect. At disk center, however, the contrast is negative, on average. Though statistical fluctuations in granulation and the 5-minute oscillation can occasionally yield a positive mean brightness at disk center, the time-average is stably negative around disk center. This disagrees with the results reported by Afram et al. (2011) (their Fig. 8), which imply

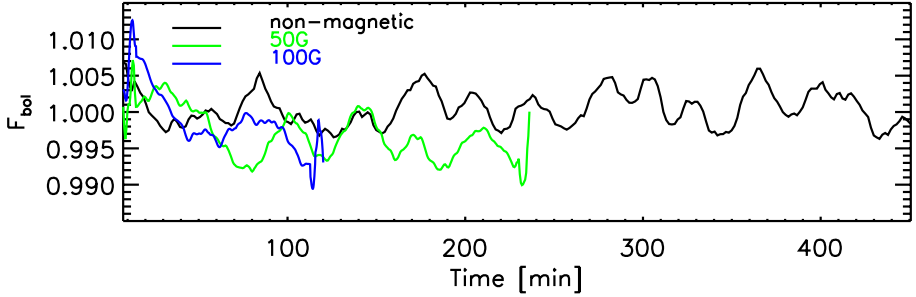


Figure 2.5: Time evolution of the bolometric flux, averaged over the 18 Mm simulation area, running means over 15 min. 100G simulation (blue), 50G simulation (green) and the non-magnetic simulation (black). Fluxes normalized to the mean of the non-magnetic run.

a net positive brightening at disk center by as much as 1% even for 50 G mean field. This is probably in conflict with observations.

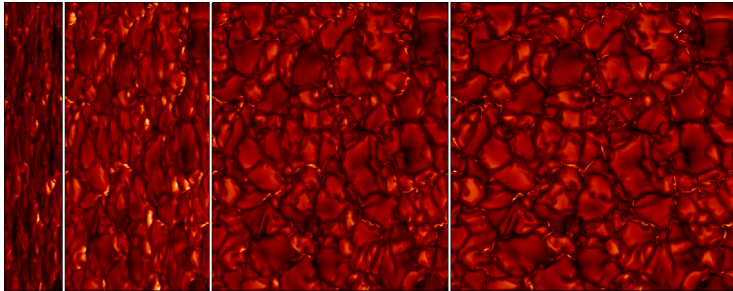


Figure 2.6: Snapshot images from the 100G simulation, showing the emergent specific intensity in the continuum at 630 nm, at viewing angles (left to right) $\mu = 0.2, 0.5, 0.82,$ and 1.0 . Height of the image is 18 Mm. (Center-to-limb variation of average brightness has been removed).

The time evolution of the bolometric surface flux of the three simulation runs is shown in Figure 2.5. Initially, Lorentz forces are absent, the magnetic field has no effect on the flow, and the flux level is unaffected. With time, the field gets concentrated into the intergranular lanes, and the Lorentz forces start having an effect on the flow. After a few granule turnover times (20 min, say) the magnetic field and the flow pattern have settled to a state which accommodates the magnetic constraints. This explains the drop in brightness of the magnetic simulations over the first couple of turnover times.

The measured difference between the 50G simulation and the non-magnetic simulation is $\Delta F_{50G-noB} = (-0.34 \pm 0.07)\%$, and $\Delta F_{100G-noB} = (-0.27 \pm 0.09)\%$ in the 100G simulation. The error bars in these numbers were computed by assuming that the average life time of a granule is 10 min, and using this to evaluate the number of independent points in the curves. To find out how this darkening comes about a closer look at the results is needed.

2.5.1 Sources of darkening

The darkening effect seen in Fig. 2.5 is the opposite of the expected magnetic brightening effect, showing that the simulations include effects that have not been detected so far in the observations (see however Kobel et al. 2012). As a plausibility check on the calculations, we invoke the procedure used in Schnerr and Spruit (2011) for measuring magnetic brightening in weak fields from high-resolution observations (see sect. 2.3.2). The result of applying this procedure to the simulations is shown in Fig. 2.8. The model fit (dotted line, cf. sec. 2.3.2) predicts a net magnetic brightening of 0.7% for the mean flux density of 50 G of the simulation. Assuming that the effect is proportional to the filling factor of the magnetic concentrations, this number translates to 0.12% for a flux density of 10 G. This agrees well with the number found for the observations in Schnerr and Spruit (2011), where the procedure yielded a brightening of 0.15% in an area with a mean unsigned flux density of 11 G.

The Schnerr & Spruit procedure is actually biased towards positive brightness contributions. It corrects for the dark lane bias (thereby increasing the inferred magnetic brightening), but does not account for the proximity effects (which reduce it). Inspection of an image gives a qualitative impression of the amplitude and spatial extent of darkening near magnetic concentrations.

Measuring proximity effects

To quantify the proximity effects we need a way to average out the individual random brightness variations near the concentrations. We do this first by simply superposing and averaging a large number of subareas centered on magnetic pixels from the time series of images. Call this the image superposition method. Our selection criteria for centering are a vertical magnetic field strength above 1 kG and a ratio between the horizontal field strength to the total field strength below 0.5, as the magnetic field in the center of the magnetic structures is nearly vertical. Magnetic concentrations consist of clumps of neighboring pixels satisfying these criteria. Since the darkening effects investigated plausibly scale approximately linearly with the amount of magnetic flux,

this selection adds the correct weight to the individual pixels in a magnetic concentration. No attempt is made to determine the ‘centers’ of the clumps, which in theory might yield a better measure of distance from a concentration. In practice, this would not help much since the clumps are actually narrow filaments. Unavoidably, their random orientation causes a certain horizontal averaging of the resulting image. The fine dark edges around the crinkles seen in Figs. 2.2, 2.6 are completely smeared out.

Figure 2.7 (top panel) shows an example snapshot with the magnetic areas selected. The contours of the upflows are shown in gray. The green lines indicate areas with a field strength higher than 1 kG, while the blue colored regions show the pixels belonging to magnetic concentrations according to our selection criteria. Figure 2.9 (left panel) shows the average of a 2000 km wide area centered on the selected magnetic pixels, from the 50 G simulation. As expected, there is a conspicuous positive brightness contribution in the center of the magnetic structure, for 50 G simulation reaching up to a factor of 1.16 of the average bolometric flux value.

As a next step we choose representative nonmagnetic areas to which the environment of the magnetic element can be compared. We use the nonmagnetic simulation for this. The areas selected for comparison should be as similar as possible to the ones where the field collects in the magnetic simulations. The typical environment magnetic structures sit in are the stagnation points of convective flows. As a practical definition of stagnation points we choose those pixels where the convergence $\sigma = -\text{div } \mathbf{v}_h$ of the horizontal velocity \mathbf{v}_h is larger than a minimum σ_{\min} . Its value is chosen such that the number of pixels selected is the same as the number selected in the magnetic image. This yields $\sigma_{\min} = 0.049\text{s}^{-1}$ for the 50 G simulation. This is then our guess of the points where magnetic fields would concentrate if a magnetic field were present. For the 100 G simulation, where the magnetic pixels occupy a larger area, a value $\sigma_{\min} = 0.039\text{s}^{-1}$ in the nonmagnetic images matches their larger number.

A representative example of the convergence points selected in this way is shown in Fig. 2.7 (bottom panel). The average brightness image resulting from this selection is shown in Fig. 2.9 (middle panel). The center shows the darkening expected from an intergranular region. The brightness increases with distance from the stagnation point, to a value near the average of the non-magnetic surface. This image contains our estimate of the dark lane bias that is present in the magnetic image in the left panel. The difference between the two (right panel) shows the magnetic brightness image corrected for the dark lane bias. It includes the sum of the proximity effect on nearby granulation and the dark rings. Due to the averaging over a large sample, the images are nearly axisymmetric. The remaining inhomogeneities give an impression of the noise level in the result.

The dashed lines in Figure 2.11 (top panel) show the axisymmetric average of the right panel of Fig. 2.9, plotted as a function of distance from the centering pixel. The

fluxes are normalized by the time and area-averaged flux F_0 of the nonmagnetic simulation. In black are the results from the 50 G simulation, in green the 100 G simulation. The average brightness excess at the center of the magnetic elements is lower in the 100 G simulation than in 50 G simulation. This probably reflects the contribution of larger concentrations, whose properties start approaching those of pores. The intensity decrease due to the dark lanes is also less pronounced in the 100 G simulation. This leads to a lower integrated intensity effect of the magnetic element environment in the case of the 100 G simulation compared to the 50 G simulation. A slightly different view is given in the left panel of Fig. 2.10, showing a 1-D section across the center of the averaged magnetic element, comparing the 50 G and 100 G simulations. The other two panels show the corresponding profiles of field strength and vertical velocity.

The middle panel of Fig. 2.10 shows that the vertical magnetic field strength in the center of the magnetic elements is slightly higher in the case of the 100 G simulation than in the 50 G simulation. This difference increases with distance to the center of magnetic structure. As the average amount of magnetic flux in the concentrations is larger in 100 G simulation than at 50 G, this is just an indication that the brightness per unit magnetic flux decreases somewhat with size. The main contribution to the intensity excess of the magnetic elements is the bright wall effect, which becomes conspicuous near the limb (Fig. 2.6). Near disk center the positive contribution is mainly the brightening seen when looking down into the magnetic elements themselves (cf. S76). As the ratio of the perimeter to the area of the magnetic structures decreases with their size, the effect of the bright walls decreases as well. Because the dark ring effect is a direct consequence of the bright wall effect, it also decreases with increasing size of the magnetic structures. The combination leads to an smaller overall intensity excess for magnetic structures of larger size, and explains the difference between the 100 G and the 50 G simulation.

A more sensitive measurement

Since the image superposition method described above produces a significant smearing of fine structure, an alternative procedure for quantifying the average brightness effects in the environment was devised. The selection of magnetic points on which to center the images is as before, but instead of superposing the entire surrounding image, the pixels used for constructing the average are restricted by the additional condition that they do not also satisfy the magnetic selection criterion.

Call this the nonmagnetic neighborhood selection. With correction for the dark lane bias as before, the resulting variation of bolometric flux with distance is shown in Fig. 2.11 (top panel, solid lines). Compared with Fig. 2.10 the environment of the magnetic point is now resolved much better. This is due to the narrow elongated structure

of magnetic concentrations. The additional selection emphasizes nearby pixels along the structure. The price is somewhat lower statistics, especially close to the center, but owing to the large area and time covered by the simulations the average remains well defined. Fig. 2.11 (bottom panel) shows the effect on average brightness within a distance r from the magnetic points. For large r , it approaches the mean brightness effect measured on the whole area of the simulation (-0.27% and -0.34% for the two simulations). It converges to this average roughly at a distance of 1.5 Mm.

Dependence on the analysis method

The analysis method described in section 2.5.1 is insensitive to the fact that magnetic structures have different sizes and therefore different horizontal extensions away from the center of the magnetic elements. This is the case since the values at each radius, shown as solid lines in Figure 2.11, are averages over grid points which have the same distance from the last point qualifying as “center of the magnetic element”. The indicated indifference of our method could smear out important signatures in our results. For this reason we divided the magnetic elements in small and large ones and studied their behaviour. “Large patches” were defined as the largest 25% of the magnetic elements in the sample and the rest were referred to as small ones. We were then looking at the different behaviour of small and large patches by comparing their bolometric intensity as a function of radius, as shown at the top of Fig. 2.12. Close to the center of the magnetic elements the bolometric flux for small (dashed lines) and large (solid lines) patches looks very much the same, but at about 250-300 km away from the center of the magnetic elements they start to behave differently. The bolometric flux of the smaller patches slowly returns at this distance to the average bolometric flux value of the simulation, while the bolometric flux of the larger patches remains below the mean flux, which is thought to be due to the larger geometrical constraint overimposed on the convection by large magnetic elements compared to the smaller ones. To test how sensitive our method is to changes in the selection criteria, we modified the ratio of the horizontal field strength to the total field strength γ , which was initially set to $\gamma < 0.5$, to $\gamma < 1/6$, while the vertical field strength criteria was left to be above 1 kG. The difference in the bolometric flux over radius between the two γ values, as depicted at the top of Fig. 2.12, showing the $\gamma < 1/6$ case in green and the $\gamma < 0.5$ case in black, can be better understood by looking at the bottom of Fig. 2.12, which displays the horizontal field strength as a function of distance from the center of the magnetic elements. From this figure it is evident, that the $\gamma < 1/6$ selection criteria detects the center of the magnetic elements more precisely, while the $\gamma < 0.5$ criteria selects regions which are already at the outer edge of the central regions of the magnetic elements. This leads to

the effect that the bolometric brightness excess at the center of the magnetic elements is higher for $\gamma < 1/6$, but it also shows that the negative brightness contribution in the surroundings of the magnetic elements, which is attributed to the dark ring effect and the convection suppression, is less pronounced for the stricter γ criteria. This is probably due to the fact that we are probing more non-magnetic intergranular lanes in the case of the $\gamma < 0.5$ criteria.

Changing the selection criteria for “large” and “small” patches in a way that the larger half of the sample counts as “large patches” and the smaller half as “small patches” didn't lead to any significantly different results compared to the previous 25%-75% division into “large” and “small” patches.

2.5.2 Resolution dependence

Fig 2.13 shows the bolometric flux over radial distance from the center of the magnetic elements for three different horizontal resolutions of $\Delta x=12.5$ km, 25 km and 50 km for one snapshot after 25 min run time of a simulation with an initially uniform vertical magnetic field of 50G. Comparing the different resolutions it becomes obvious, that the change from the 25 km resolution to 12.5 km resolution mainly affects the brightness excess at the center of the magnetic elements, which changes from 14% to 19% above the bolometric flux mean value, while the dark ring effect is amplified by only 1%. Switching from 50 km resolution to $\Delta x=25$ km affects almost equally the brightness contribution from the dark ring region as well as the center of the magnetic elements, leading to an amplification of these effects by around 5% switching to the higher resolution. But one has to be careful comparing the bolometric flux over radius for different numerical resolutions like this. Even though the same initial snapshot was used for the different spacial resolutions, a different spacial resolution also implies resolving different physical length scales, which leads to different granulation patterns. The change of the granulation pattern introduces a statistical fluctuation of the bolometric flux which can not be disentangled from the numerical resolution effect, unless one has long enough runs times to get a grasp of the statistical fluctuations and a accurate measurement of the mean values and their errors for the three different resolutions. However this is beyond the scope of this work, since it requires a very high computational effort.

2.5.3 Vertical velocities

The dark ring occurs due to radiative cooling of the surroundings of the magnetic elements. Due to this cooling enhanced downdrafts are expected. The effect is seen in the

right panel of Fig. 2.10, though the very narrow structure of the downdrafts has been smeared out considerably by averaging process. The average downflow speeds are consequently also less pronounced in the 100 G simulation than in the 50 G simulation.

As was done in Fig. 2.11 for the bolometric flux, the effect of the magnetic fields on their surroundings can also be seen in the vertical velocity amplitudes near magnetic concentrations. We compare them with the velocities in similar regions in a non-magnetic simulation. They are selected on the basis of flow convergence (the locations where the small scale magnetic field is expected to collect), with the same selection process as used for the bolometric flux difference. The result (Fig. 2.14) shows that the downflows are stronger around the magnetic elements, as expected. With increasing distance the average velocity becomes dominated by upflows in the surrounding granulation. Up to a distance of about 700 km, the upflow speeds are markedly lower around magnetic elements. Beyond this distance the sign of the difference reverses. The velocity difference (bottom panel) peaks around -1.1 km/s, at a distance of ≈ 300 km. Note the similarity of these difference curves to the bolometric flux differences in Fig. 2.11 (top).

2.6 DISCUSSION AND CONCLUSIONS

The effect of the small scale magnetic field on (bolometric) brightness appears to have three distinct components: the brightness of the magnetic structure itself (composed of the bright interior of the structure at disk center, and the ‘bright wall effect’ towards the limb), plus the two proximity effects it has on its surroundings: the ‘dark ring’ resulting from the influx of radiation into the magnetic concentration, and the interference of magnetic concentrations with the nearby convective flow.

The most conspicuous component is the bright wall effect, easily measurable as a brightening in active regions when seen near the solar limb. It has also been reproduced convincingly in realistic 3-D MHD simulations such as Carlsson et al. (2004), De Pontieu et al. (2006), and the present ones (cf. Fig. 2.6). The $0''.1 - 0''.2$ narrow dark rings are also conspicuous in high resolution continuum images near disk center, but are less easily quantifiable because of the variable shapes of the structures (‘crinkles’). Finally, the effect on the surrounding convective flow pattern is well known from observations, but its effect on brightness is hard to detect smeared out over too large an area to be measurable at the photometric accuracy of ground based observations. It has been detected however, in data from Hinode (Kobel et al. 2012).

Perhaps surprisingly, the negative contribution of the proximity effects turns out to dominate the photospheric brightness change. The net brightness effect is thus the opposite of the standard prediction (S77). Observationally, the effect of magnetic con-

centrations on nearby convective flows is easily detectable through changes in granulation morphology and vertical velocities ('anomalous granulation', cf. Title et al. 1986, 1992, Kobel et al. 2012). Concerns that these changes could also affect energy transport and hence surface flux have been around for some time (e.g. Spruit 1998). They were not discussed much, possibly because the effect was not large enough to be detected with ground based photometric accuracy. Our simulations also show changes in vertical velocities near magnetic concentrations. The spatial coincidence of these changes with changes in bolometric flux support the interpretation that the net darkening is caused by interference with the convective heat flux near magnetic concentrations. The effect appears to take place in a rather narrow region, extending from the intergranular lane to somewhat into the surrounding granule.

The magnetic concentrations are larger on average in the 100 G simulation than at 50 G. Their effect on the surrounding flows is correspondingly somewhat larger (Fig. 2.14 bottom panel). The net negative effect on bolometric brightness does not differ much in the 50 G simulation. We interpret this as a consequence of the compensating bright wall effect. Its increase towards the limb is most prominent in larger concentrations that are less affected by self-obscuration away from disk center. This is evident in the disproportionately larger brightness increase of the 100 G simulation towards the limb compared with the 50 G result (Fig. 2.4). It can also be seen qualitatively in the CLV of the images in Fig. 2.6.

This leaves the question how the observed positive correlation of Total Solar Irradiance (TSI) with the small scale field comes about. The most likely explanation is that the simulations underestimate the contribution of chromosphere and upper photosphere. A major contribution of the chromosphere to TSI has in fact already been inferred from the wavelength dependence of solar irradiance variability. Unruh et al. (1999) concluded that the photosphere contributes negligibly to TSI variation, compared with the chromosphere. More recently, Ball et al. (2012) estimate the photospheric contribution at 18%.

Empirical models for the mean stratification in active regions such as Vernazza et al. (1973) already indicated the presence of heating processes starting around the temperature minimum. This has been interpreted as evidence of some form of magnetic heating. Our calculations necessarily miss most of this contribution because of the use of a potential field as upper boundary condition. This forces the field near the upper boundary to its lowest energy state, from which no energy can be extracted. Proper inclusion of magnetic dissipation in simulations like the present ones is very demanding, because of the time step limitations resulting from the high Alfvén speed in the chromosphere. Simulations with methods adapted to this situation may be needed, such as have been developed by Gudiksen and Nordlund (2005) for the coronal heating problem.

Furthermore the influence of numerical resolution on our results would have to be investigated more carefully. The test we performed, gave us a hint that a numerical resolution dependence exists, which could lead to an unproportional change in the brightness excess at the center of the magnetic elements compared to the change in darkening due to the dark ring effect for different resolutions. But to be able to quantify the overall brightness contribution at different spacial resolutions, it would be required to do long simulation runs to get statistically significant results for the bolometric flux mean values, which is however beyond the scope of this work because of its high computational resources needed.

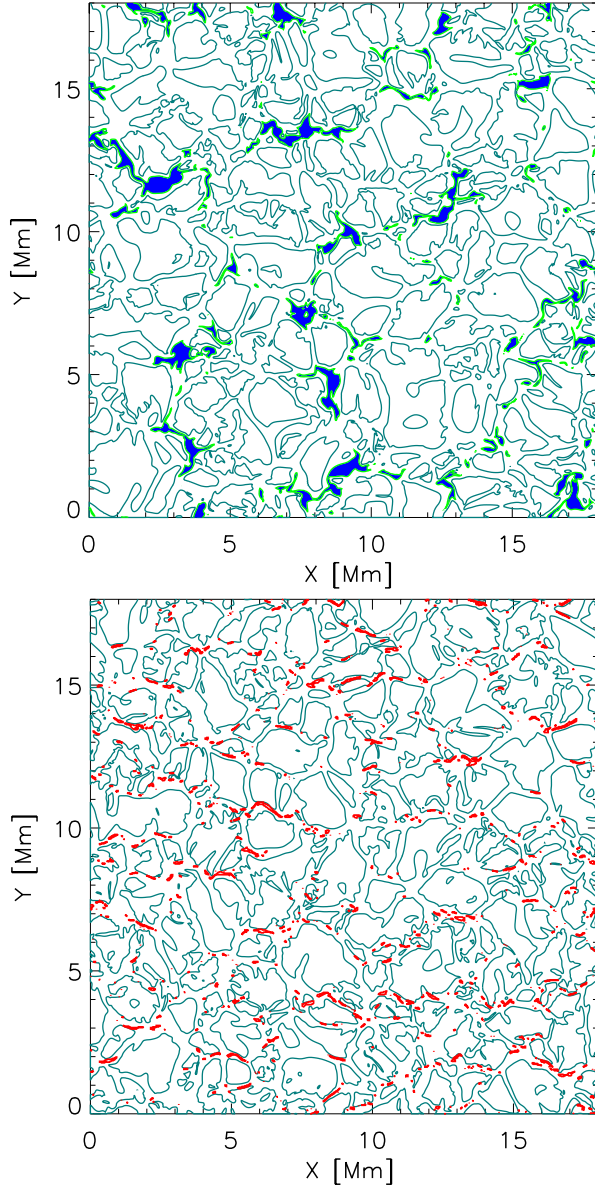


Figure 2.7: Magnetic and stagnation point selection. The grey contours (at $v_z = 0$) enclose the upflows. Top panel: snapshot from the 100 G simulation. Green contours are at a vertical field strength of 1kG, the blue contours enclose the centering pixels of our magnetic structures. Bottom panel: a snapshot from the nonmagnetic simulation. Pixels (red) show the regions of flow convergence used as reference ($-1/\text{div } \mathbf{v}_h < 26$ s).

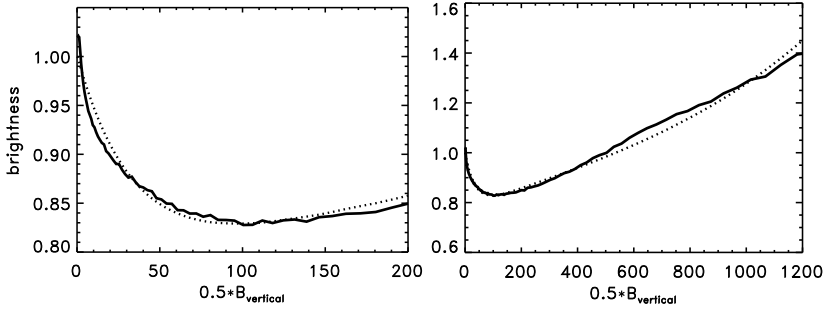


Figure 2.8: As in Fig. 2.3, for the 50G simulation. The field strength scale shown corrects approximately for the difference in field strength at the nominal photosphere in the simulations (around 500 nm continuum optical depth unity) and the effective measurement level in the 630.25 nm Line used in the observations.

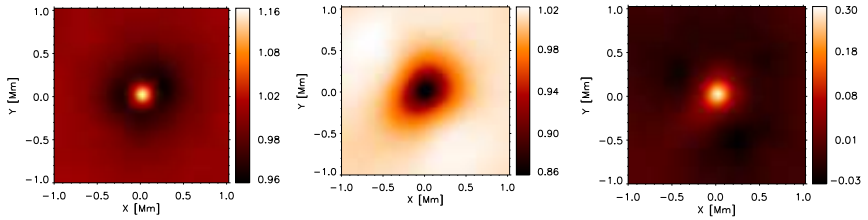


Figure 2.9: Average brightness variation near magnetic structures in the 50 G simulation (left). Middle panel shows the equivalent in control areas (the stagnation points of the convection flow as seen in the non-magnetic simulation). The difference (right) shows the net brightness effect of the magnetic concentrations.

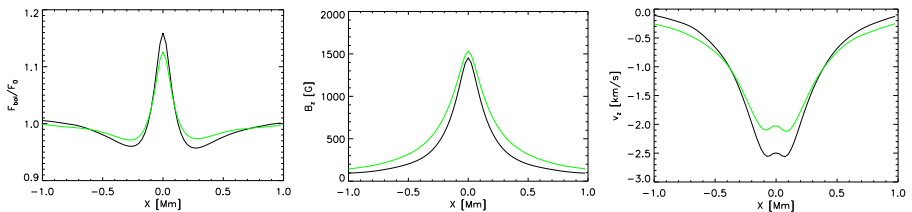


Figure 2.10: Left: bolometric flux (normalized by the average flux F_0 of the nonmagnetic simulation). Middle: vertical magnetic field strength. Right: downflow velocity. All variables are shown along a straight line across the center of the averaged magnetic element. Green: 100 G simulation, black: 50 G.

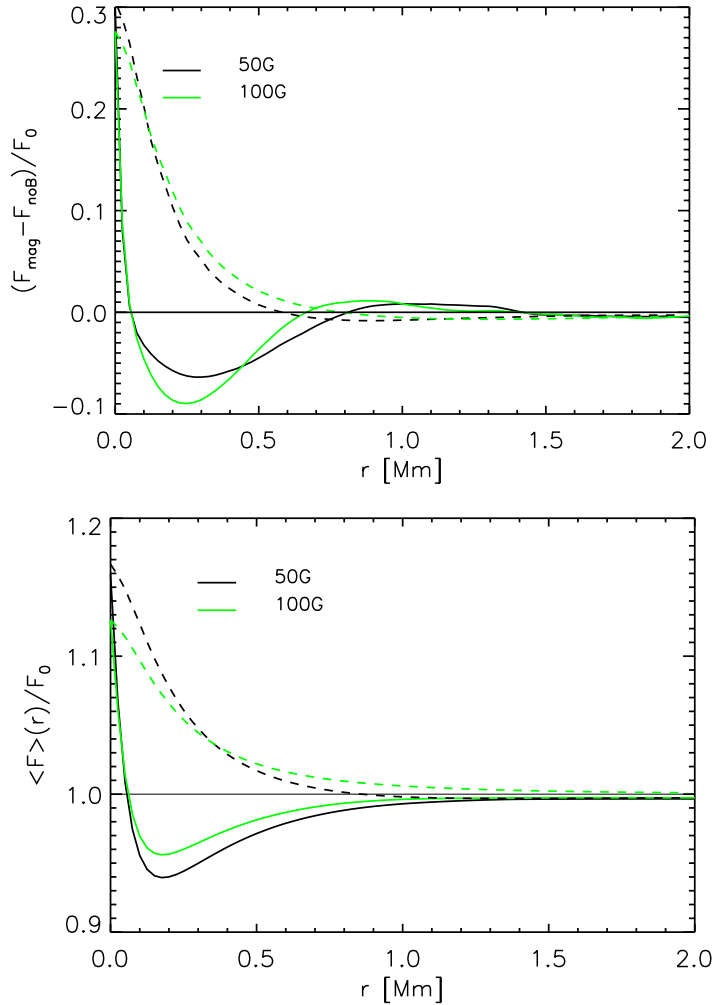


Figure 2.11: Top, solid lines: variation of bolometric flux as a function of distance r from a magnetic concentration, corrected for dark lane bias, and using the nonmagnetic neighborhood selection method (see text). Dashed: same but using the image superposition method of Fig. 2.9. Bottom: same data, but showing the average brightness inside the distance r . Green: 100 G simulation, black: 50 G simulation.

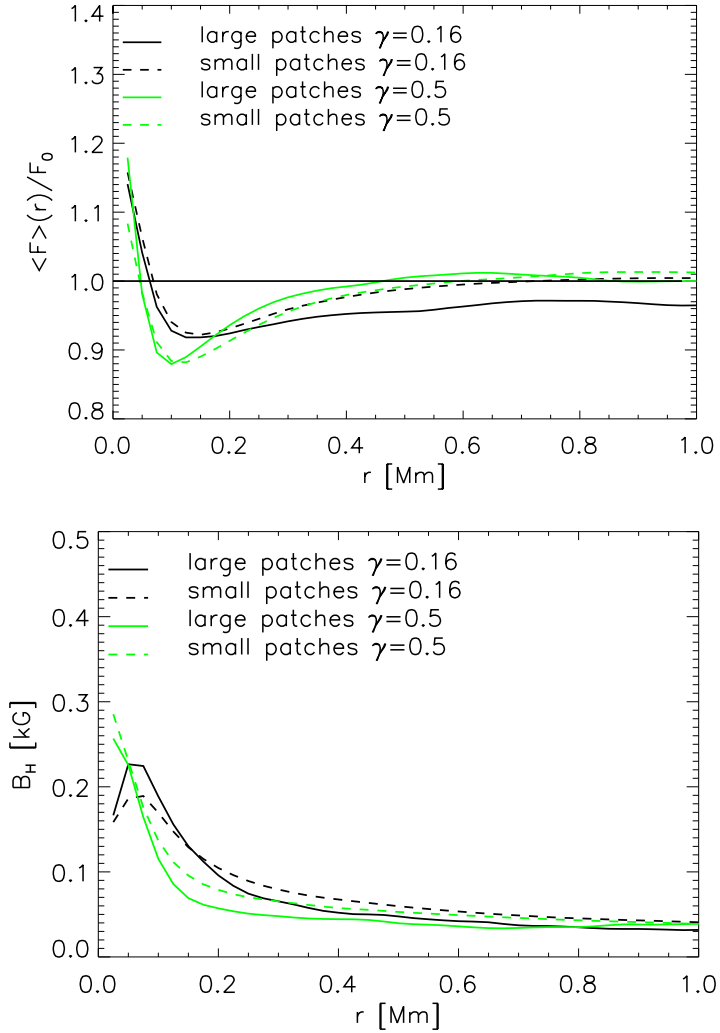


Figure 2.12: Top: bolometric flux, Bottom: horizontal field strength, as a function of distance from the magnetic elements for small (dashed lines) and large (solid lines) magnetic elements for two different selection criteria for magnetic elements, taking either a ratio of the horizontal field strength over the total field strength $\gamma < 0.5$ (green) or $\gamma < 1/6$ (black) additionally to the criteria of a vertical magnetic field strength above 1kG.

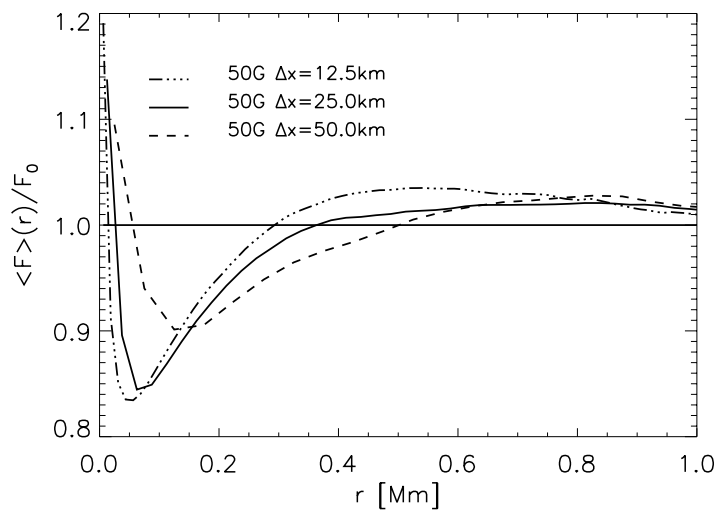


Figure 2.13: bolometric flux as a function of distance for the 50G simulation for the horizontal resolutions $\Delta x = 12.5\text{ km}$ (dotted dashed line), 25 km (solid line) and 50 km (dashed line) for one snapshot after 25 min simulation time

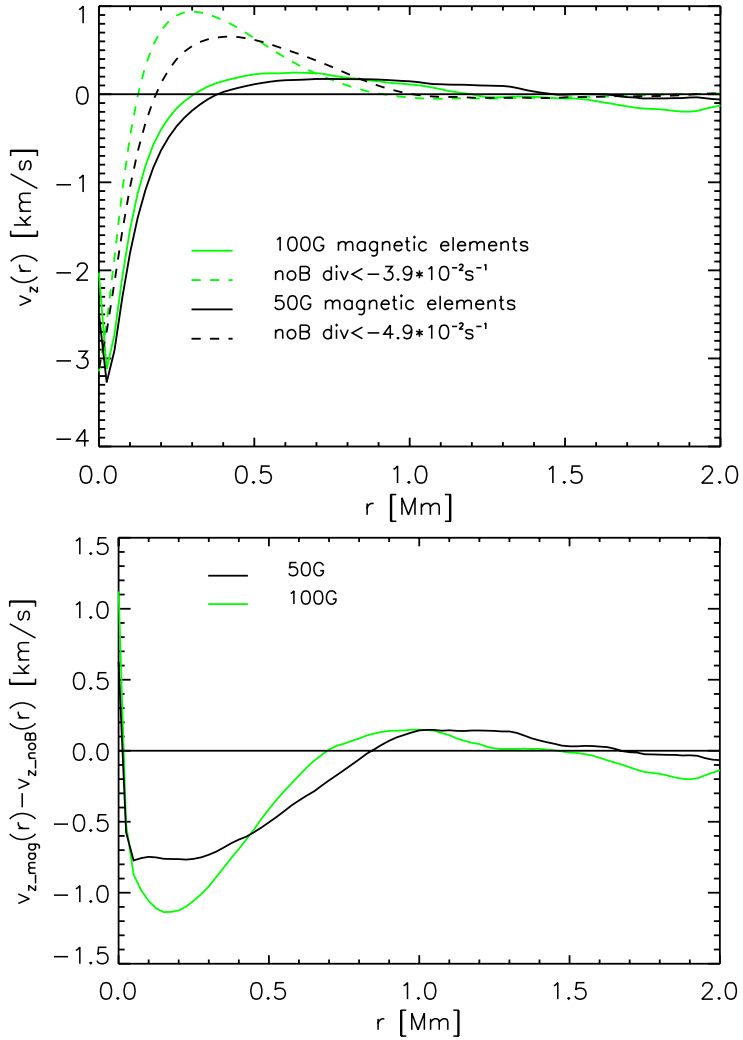


Figure 2.14: Top: average vertical velocity $\langle v_z \rangle$ as a function of distance from magnetic elements (solid) compared with $\langle v_z \rangle$ near flow convergence points of the nonmagnetic simulation (broken). Bottom: difference between the two, showing the proximity effects on vertical velocities.

REFERENCES

- Afram, N., Unruh, Y. C., Solanki, S. K., Schüssler, M., Lagg, A., Vögler, A. 2011, *A&A*, 526, A120
- Ball, W. T., Unruh, Y. C., Krivova, N. A., et al. 2012, *A&A*, 541, A27
- Beeck, B., Collet, R., Steffen, M. and Asplund, M., 2012, *A&A*, 539, 121
- Carlsson, M., Stein, R. F., Nordlund, Å., & Scharmer, G. B. 2004, *ApJ*, 610, L137
- Collet, R., Hayek, W., Asplund, M. and Nordlund, Å., 2011, *A&A*, 528, 32
- Chiang, W.-H., & Foukal, P. 1983, *Sol. Phys.*, 97, 9
- De Pontieu, B., Carlsson, M., Stein, R., et al. 2006, *ApJ*, 646, 1405
- Foukal, P., & Bernasconi, P. N. 2008, *Sol. Phys.*, 248, 1
- Frazier, E. N. 1971, *Sol. Phys.*, 21, 42
- Fröhlich, C. 2006, *Space Sci. Rev.*, 125, 53
- Fröhlich, C., & Lean, J. 2004, *A&A Rev.*, 12, 273
- Galsgaard, K., & Nordlund, Å. 2004, *A&A*, 419, 13445
- Gudiksen, B.V., & Nordlund, Å. 2005, *ApJ*, 618, 1020
- Keller, C. U., Schüssler, M., Vögler, A., & Zakharov, V. 2004, *ApJ*, 607, L59
- Kobel, P., Solanki, S. K., & Borrero, J. M. 2012, *A&A*, 542, A96
- Macris, C., & Elias, D., 1955, *Ann. Astroph.* 18, 143
- Macris, C., 1979, *A&A*, 78, 186
- Macris, C. J., Muller, R., Rösch, J., & Roudier, T. 1984, in *Small-Scale Dynamical Processes in Quiet Stellar Atmospheres*, S.L. Keil (ed.), National Solar Observatory, Tucson, p265
- Pietarila Graham, J., Danilovic, S., & Schüssler, M. 2009, *ApJ*, 693, 1728
- Sánchez Almeida, J., Bonet, J. A., Vitičić, B., & Del Moro, D. 2010, *ApJ*, 715, L26
- Schmidt, W., Grossmann-Doerth, U., & Schröter, E. H. 1988, *A&A*, 197, 306
- Schnerr, R. S., & Spruit, H. C. 2011, *A&A*, 532, A136
- Spruit, H. C. 1976, *Sol. Phys.*, 50, 269 (S76)
- Spruit, H. C. 1977, *Sol. Phys.*, 55, 3 (S77)
- Spruit, H. C. 1991, in *The Sun in Time*, Sonett, Giampapa & Mathews (eds.), University of Arizona Press, p118–158 (S91)
- Spruit, H. C. 1998, in *New Eyes to See Inside the Sun and Stars* (IAU Symposium no. 185), Deubner et al. (eds.), p103
- Steiner, O. 2005, *A&A*, 430, 691
- Title, A. M., Tarbell, T. D., Acton, L., Duncan, D., & Simon, G. W. 1986, *Advances in Space Research*, 6, 253
- Title, A. M., Topka, K. P., Tarbell, T. D., et al. 1992, *ApJ*, 393, 782
- Unruh, Y. C., Solanki, S. K., & Fligge, M. 1999, *A&A*, 345, 635
- Vernazza, J. E., Avrett, E. H., & Loeser, R. 1973, *ApJ*, 184, 605
- Wenzler, T., Solanki, S. K., Krivova, N. A., & Fröhlich, C. 2006, *A&A*, 460, 583

Chapter 3

Flux canceling in 3D radiative MHD simulations

I. Thaler & Henk Spruit

Submitted to A&A

3.1 INTRODUCTION

The magnetic flux which emerges in new active regions throughout a sunspot cycle has largely disappeared from view again at the next minimum. The emergence of active regions at the surface is conspicuous even at moderate spatial resolution, but the process by which it disappears has proved much harder to observe. This is even more striking on shorter time scales. In active complexes, where new active regions continue to emerge within a limited region over periods weeks to months, the total flux seen in synoptic magnetograms remains rather stable. From observations of such regions Howard & Labonte (1981) deduced that newly erupted flux disappears from view in about 10 days. The implication is that magnetic flux somehow ‘cancels’ against opposite polarities within the confines of the complex, on this time scale. Direct observations individual active complexes have confirmed this (for impressive examples see Rabin et al. 1984, Kálmán 2001).

The invisibility of the canceling process at the resolution of routine magnetograms implies that it takes place on very small spatial scales. On scales of the order of an arcsecond, canceling of opposite polarities in a mixture is observed to be quite effective (Martin et al. 1985, Kubo et al. 2010a, see also Yang et al. 2012).

Most models developed to account for the evolution of the surface magnetic field on larger scales treat it as a scalar field governed by a two-dimensional diffusion equation. In this procedure, newly forming active regions have to be exempted from diffusion. Their emergence looks almost like diffusion, but with the arrow of time reversed: small scale mixtures of opposite polarity separate themselves out into large scale bipolar active regions¹. In a diffusion view, a negative value of the diffusion coefficient would have to be arbitrarily assumed in regions where flux is observed to be emerging.

Small-scale displacements of identifiable magnetic concentrations have been used to derive observational values for diffusion coefficients. These displacements are dominated by granulation and supergranulation flows. The assumption is made that the evolution of average magnetic fields on larger spatial scales can be described by an effective diffusion based on such random displacements. On the scale of granular flows the values obtained by ‘magnetic bright point tracking’ are $D = 70 - 90 \text{ km}^2\text{s}^{-1}$ from SOHO/MDI magnetograms (Hagenaar et al. 1999). Somewhat lower values, $D \approx 60 \text{ km}^2\text{s}^{-1}$ have been reported from higher resolution observations with the Swedish Vacuum Solar Telescope (Berger et al. 1998). For supergranular flows the inferred diffusion coefficients range from $120 - 230 \text{ km}^2\text{s}^{-1}$ using cross correlation techniques

¹For a nice example see the ‘Hinode trilobite’:
http://science1.nasa.gov/media/medialibrary/2007/09/18/18sep_trilobite_resources/Hinode_lower.mov

(Wang 1988, Komm et al. 1995), and $140 - 300 \text{ km}^2\text{s}^{-1}$ using object tracking (Smithson 1973, Mosher 1977, Schrijver & Martin 1990).

The evolution of large scale magnetic patterns during the solar cycle is classically attributed to the effect of granulation and supergranulation (Leighton 1969). Diffusion coefficients required to match the dispersal of the large scale field, of order $600 \text{ km}^2\text{s}^{-1}$ (Sheeley 1992) differ from the small-scale measurements. Inclusion of the effect of a meridional circulation reduces the discrepancy (Wang et al. 1991). Even apart from the seemingly negative diffusion in emerging flux regions, the remaining variation in numbers suggests that other factors are at work besides the observed convective flows.

Because magnetic fields are divergence-free, field lines have no ends and are intrinsically three-dimensional. Field lines continue above and below the observed surface, and Lorentz forces propagate along their entire length. It would be very surprising if the evolution of the surface magnetic field could be reduced to effects of the flows observed at surface. To the extent that field lines are ‘anchored’ in deeper layers, for example, their evolution is governed by conditions in those layers, rather than by surface observables. With the advent of realistic 3-D MHD simulations of the solar photosphere it has become possible to study the physics underlying the dispersal of magnetic fields in a much more comprehensive way than is possible from observations. As a step in this direction we study here the dependence of ‘flux canceling’ on conditions in the deeper layers of the simulation, and on the mean strength of the field.

To quantify the canceling rates, we extract ‘effective diffusion coefficients’ from the simulations, that is, numbers that in a simple 2-D diffusion model would yield the same decay rates of unsigned flux. The actual 3-D magnetohydrodynamic canceling process actually bears almost no relation to such a simple view, or to other turbulent diffusion models. This reflects itself in the measured values being far from constant, depending not only on time but also on all other factors such as horizontal length scale, depth of the simulation box, and the initial mean flux density. Our expectation is that the dependence on these factors will help, on the one hand in conceptualizing the processes at work, and on the other in interpreting observed canceling rates.

3.2 THREE-DIMENSIONAL MAGNETIC FIELDS

Turbulent diffusion models based on displacements of field lines by convective flows would need to accommodate negative as well as positive diffusion coefficients. This is in conflict with the MHD equations, however, which are invariant to a change of sign of the magnetic field vector. A consequence of this invariance is that there is no flow, however complex, that can separate magnetic polarities out of a random mixture.

The observations show that the separation process taking place in flux emergence

ignores all convective flows in the area (Vrabc 1974). The emergence process is driven instead by forces in the magnetic field itself. It is to be understood as the result of a bundle of magnetic field rising through the surface (as proposed first by Cowling 1953). Numerical simulations of such a rising bundle (Isobe & Shibata 2004, Cheung et al. 2010) reproduce the separation process convincingly. The separation process of the opposite polarities is a combination of the magnetic buoyancy bringing the field to the surface (the ‘rising tree’ picture, Vrabc 1974, Zwaan 1978, 1985) and the unbalanced magnetic tension in the part of the horizontal field strand that remains below the surface (Moreno Inertis et al. 1994).

The difficulty of including the emergence process in models for surface field evolution, other than by ad hoc engineering procedures, illustrates the importance of the connection of the surface field with its roots in deeper layers: the three-dimensional, solenoidal nature of the magnetic field. Given this connection, one should expect that it plays a role also in regions where no new flux emerges. It follows that the evolution of the large scale field at the surface is not determined just by the observed displacements such as granulation, supergranulation, and meridional circulation, but also by unobservable things deeper down.

The degree to which deeper layers contribute depends on the strength of their magnetic connection to the surface. This connection is determined by the intrinsic field strength of the magnetic concentrations, rather than an average (unsigned) flux density at the surface. At a strength of 50 G the connection is weak, but at the intrinsic strength of magnetic concentrations, of the order 1-2 kG, the Alfvén speed is higher than convective flow speeds down to depths of several Mm. At such depths the field strength in the magnetic elements may actually be even higher than at the surface, and the connection even stronger.

The size of the region over which the diffusion acts is also important. If the length scale on which the polarities are mixed is small, anchoring at a large depth is unlikely to affect the rate of canceling as seen at the surface. On the other hand, if the horizontal distance of interest is large, hundreds of Mm, say, anchoring effects as deep as the base of the convection can become relevant for the evolution of the surface field.

3.2.1 ‘flux canceling’

This subsection contains some theoretical considerations relevant to the interpretation of the results reported below, in particular their dependence on mean field strength (the ‘average unsigned flux density’) in sect. 3.4.3.

Mixing vs. canceling

At low spatial resolution, a mixture of opposite polarities becomes undetectable long before the small scale structures that make up the mix have physically disappeared. To detect physical disappearance (‘canceling’) the spatial resolution has to be high enough to resolve the small scale structures themselves. Kubo et al. (2010b) infer that the process takes place below the sub-arcsecond resolution of the Hinode/SOT instrument.

Mixing and canceling involve different physics. Mixing due to displacements of magnetic elements along the surface does not change the ‘unsigned flux’ $|B_z|$ crossing the surface. The displacements can be due to convective flows in which the elements are embedded, or to magnetic forces: magnetic tension and magnetic buoyancy.

Actual canceling, a reduction $|B_z|$, involves reconnection: the exchange of field line directions at a point where bundles of opposite direction physically touch. This can happen at any point along the bundles: there is no a priori reason why it would take place exactly at the surface where observations are made. Reconnection, a fundamentally three-dimensional process, cannot be meaningfully represented by a two-dimensional ‘canceling’ picture. If opposite bundles first touch below the photosphere, they reconnect into two hairpins one of which is pulled down by the magnetic tension at the bend in the pin, the other upward. The same happens if the reconnection takes place above the photosphere. The two cases would look much the same in a high-resolution magnetogram (Fig. 2 in Zwaan 1987).

The difference between mixing and canceling is academic in a turbulent diffusion view, in which the evolution of the field is seen as a cascading process of decreasing length scales. Guided by experience in ordinary hydrodynamics, the net rate of mixing and magnetic dissipation in this view is assumed to be independent of the length scale on which the actual reconnection takes place. This view would then apply when the field strength is low enough, such that Lorentz forces can be neglected compared with the characteristic hydrodynamic forces².

The effect of field strength

At the intrinsic kG strength of the small scale magnetic field, magnetic forces cannot be ignored for the discussion of canceling. High-resolution observations of small scale

²The presence of the Alfvén velocity as a characteristic length-independent speed invalidates this view. At sufficiently small length scales, the velocities implied by a Kolmogorov cascade become smaller than the Alfvén speed. At and below this length scale the tension force in the magnetic field cannot be ignored (Goldreich and Sridhar, 1997). In addition, the assumption made in turbulence models that physics at large scales does not depend on the dissipation scale, is in conflict with evidence that magnetic dissipation on microscopic scales (as measured by the magnetic Prandtl number) has a direct effect on the larger scales (cf. Schekochihin et al. 2004, 2007, Fromang and Papaloizou 2007).

flux elements for example show that their displacements do not match the flows in the granulation around them (Kubo et al. 2010a).

The effects are different in the high- β environment below the photosphere and the low- β atmosphere. Below the surface, the magnetic elements are separated from each other by low-field strength plasma; they do not exert forces on each other unless they are brought into direct contact.

This is different in the low- β atmosphere. The Alfvén speed in the atmosphere of a typical active region field strength of 50 G is so high that reconnection is fast compared with the time scale on which the magnetic elements move around. As a result, the atmospheric field is in a quasi-static state close to the lowest energy configuration: the potential field determined by the distribution of the vertical field component at the surface, as actually is observed in the chromosphere. The forces between neighboring magnetic structures in such a field are like those between bar magnets: they sense each other already at some distance, bundles of opposite polarity attract each other via this potential field above the surface.

The changes in magnetic energy associated with these changes do not turn up as dissipation in the atmosphere. Instead, the changes in magnetic energy in the atmosphere are accounted for by the work done against the forces acting at the foot points. Much like the magnetic energy in the vacuum field around neighboring bar magnets. This explains why only modest evidence of magnetic energy release in the atmosphere is found in canceling events ³.

Retraction

When the attraction has brought elements of opposite polarity together to a distance of the order of their diameter, the force becomes strong enough for magnetic tension to pull to the hairpin below the surface. This process of ‘retraction’ has been invoked intuitively as the main cause of the observed cancellation in mixed polarity regions (e.g. Rabin et al. 1984, Topka et al. 1986, Kálmán 2001). Since the attractive force increases as the square of the field strength, one should expect that effective diffusion coefficients used to model canceling will turn out to depend on the mean absolute field strength in the area (the ‘unsigned flux density’).

³The Poynting flux is often invoked as a measure of the magnetic energy flux that is available for heating of the atmosphere. It is not a reliable measure of actual magnetic heating, however, since it includes not only dissipation of energy, but also a change in magnetic energy content unrelated to dissipation. As a result, it can even be negative (downward). The magnetic energy content of the atmosphere above two neighboring flux tubes of opposite polarity, for example, decreases as the two are brought together. The Poynting flux is downward, the corresponding energy delivered to the footprints. The attractive force between the two goes into kinetic energy below the boundary.

3.2.2 Simulations

Cameron et al. (2011) studied the rate of canceling of opposite polarities at the surface with 3-D radiative MHD simulations extending to 800 km below the surface. Their simulations start with a vertical field of uniform strength, in a 2×2 checkerboard pattern of positive and negative polarities. The simulations follow the decay of the (unsigned) flux density in an area of $6 \times 6 \text{ Mm}^2$. An effective diffusion coefficient of $D \approx 340 \text{ km}^2\text{s}^{-1}$ was measured. This is then a diffusion rate that would apply to field dispersal and cancelation, provided only the flows down to a depth of the order of half a granule contribute and anchoring effects below this depth are absent.

With the calculations reported below we measure effective diffusion rates in simulations extending to significantly greater depths below the surface. The purpose is to determine how they depend on the degree to which the field is concentrated into kG bundles (sect. 3.4.2), and on the mean unsigned flux density in the area (sect. 3.4.3).

3.3 CALCULATIONS

3.3.1 Numerical methods

The numerical simulations were realized with the 3d magnetohydrodynamics code STAGGER developed by Galsgaard & Nordlund (1996). The code solves the time-dependent magnetohydrodynamics equations by a 6th order finite difference scheme using 5th order interpolations for the spatial derivatives, while the time evolution is done using a 3rd order Runge-Kutta scheme. For every time step the radiative transfer equation is solved at every grid point assuming local thermal equilibrium. This is done by using a Feautrier-like scheme along the rays with two μ -angles plus the vertical and four ϕ -angles horizontally, which adds up to nine angles in total. The wavelength dependence of the absorption coefficient is taken into account by the opacity binning method (Nordlund 1982, Skartlien 2000). The equation of state table used for all simulations except the 200 G, 500 G, 1000 G setup, was calculated using a standard program for ionization equilibria and absorption coefficients (Gustafsson 1973). For the 200 G, 500 G, 1000 G setup the equation of state table used is further described in Beeck et al. (2012). The horizontal boundaries are periodic, while on the top and bottom we have open transmitting boundaries. The effective temperature of the surface is controlled in the standard way (Galsgaard & Nordlund 1996) by adjusting the entropy of inflowing material at the lower boundary. The magnetic field is kept vertical at the lower boundary. At the top a potential field extrapolation is implemented as boundary condition.

3.3.2 Setup

As mentioned in the introduction, observations show that magnetic fields of different polarities not always tend to diffuse and cancel out, but just under certain conditions. As argued in sect. 3.2 above, the rate of flux canceling seen at the surface must depend on the conditions found deeper down in the convection zone.

We tested how the time scale of the diffusion process changes, depending on how deep the magnetic field lines are anchored in the convection zone. The field is allowed to move horizontally at the lower boundary of the simulation box. The anchoring effect is studied by simply varying the depth of this boundary. The effect found thus includes only the magnetic connection down to this depth. By omitting magnetic stresses due to the continuation of the field into even deeper layers, this yields a lower bound on the anchoring effect.

We choose one setup with a vertical extent of 10 Mm and one of 2.85 Mm measured from the photosphere downwards into the convection zone. In both of these we tested if the diffusion coefficient changes when the magnetic field is already fragmented into kG flux tubes before starting the diffusion process. These fragmented magnetic field simulations are compared with those in which the absolute value of the field strength is initially uniform. A third variable tested for its effect is the strength (average flux density) of the initial field. In all cases the initial field varies across the box in a pattern of stripes of alternating polarity.

Uniform initial $|B_z|$ of 20 G, 50 G and 100 G

For the simulations with an initially uniform vertical magnetic field strength of $B_z = 50$ G, the simulations were run in a box of $48 \text{ Mm} \times 6 \text{ Mm}$ in the horizontal and 2.85 Mm or 10.5 Mm respectively in the vertical direction. The box in both cases extends to 474 km above the photosphere. Each of these simulations was run for two different horizontal resolutions, 25 km and 100 km. The vertical resolution is the same in both cases, varying from a maximum resolution of 11 km around around the photosphere to 34 km at 3 Mm and 55 km at 10 Mm depth. As initial condition for the hydrodynamics the result of a standard field-free simulation is used, relaxed to a statistically steady state. As initial magnetic field configuration, two different setups were used. In one, the magnetic simulation started by adding a vertical magnetic field of uniform strength $|B_z| = 50$ G in stripes of alternating polarities of 3 Mm width. In the box of 48 Mm this results in 16 stripes of $3 \text{ Mm} \times 6 \text{ Mm}$. In the other setup, the stripes of alternating polarity had a width of 6 Mm, while the vertical magnetic field used was still $|B_z| = 50$ G. The Lorentz force in this field vanishes initially, so that the transition from the hydrodynamic initial condition is smooth. Every simulation ran for 60 minutes of solar

time. For the simulations with an initial field strength of $|B_z| = 20$ G and $|B_z|=100$ G, a similar simulation set up as for the 50 G simulations was used, except that the vertical box size was restricted to a vertical depth of 2.85 Mm and a horizontal resolution of 100 km.

Initial field fragmented into kilo-Gauss fields

In this setup we first construct a field which is already gathered into magnetic kG-flux tubes before the we let the diffusion process set in. This is done with a simulation similar to the above, but for a vertical magnetic field of uniform polarity. The horizontal average vertical field strength is thus constant in time. This is done in a box of 3 Mm \times 6 Mm. This simulation is evolved until the magnetic field has accumulated in the downflows at all depth levels, and a vertical magnetic field strength of at least a 1kG has been reached for some magnetic structures even at the bottom of the simulation box. For the 10.5 Mm simulation this took around 6 hours of solar time, for the 2.85 Mm simulation about 2.3 hours. The diffusion simulation was then set up by doubling the 3 \times 6 Mm² simulation to 6 \times 6 Mm² horizontal extent, and inverting the magnetic field polarity in one of the 3 \times 6 Mm² stripes. The horizontal resolution is 25 km, the vertical resolution as described in 3.3.2.

In this construction, there are always some field lines that cross the boundary between the two polarities, since the horizontal boundary conditions are periodic. The divergence of the magnetic field does not vanish there after the polarity change. The problem can be minimized by adjusting the boundary where the polarity is changed to a location where it does not cut across a strong magnetic concentration. In addition the $\text{div } \mathbf{B}$ cleaning routine of the STAGGER code was used for the first couple of seconds of the simulation.

The initial magnetic field configurations for the 10.5 Mm-deep simulation are shown in Fig. 3.1 at the nominal depth $z = 0$ of the photosphere, and at 2.85 Mm and 10 Mm below the photosphere. The initial states for the 2.85 Mm simulation are shown in Fig. 3.2 for the photosphere and at 2.85 Mm below the photosphere. In both cases three different initial conditions are shown, to be used for statistical averaging of the results in the later analysis.

Uniform initial $|B_z|$ of 200 G, 500 G, 1000 G

For measurements of the effective diffusion coefficient dependence on the initial magnetic field strength we used a slightly different setup: a box of 12 \times 12 Mm² horizontal and 3.4 Mm depth, 474 km of which above the photosphere and 2.7 Mm below. The horizontal resolution is 100 km, while the vertical resolution varies from 13 km near

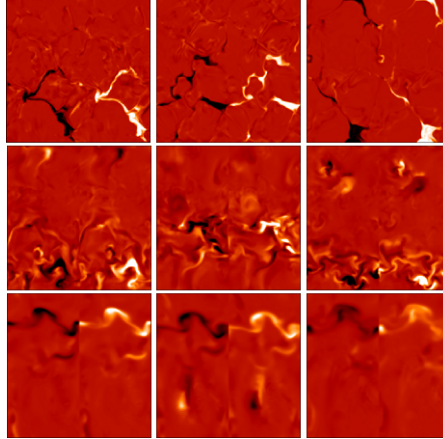


Figure 3.1: Three different initial magnetic field configurations (top from left to right) for simulation runs having an initial magnetic field fragmented into kG flux tubes before the diffusion process sets in. Horizontal cuts at $z = 0$ (top row), 2.85 Mm (middle) and 10 Mm (bottom row). Vertical extent of the simulation 10.5 Mm.

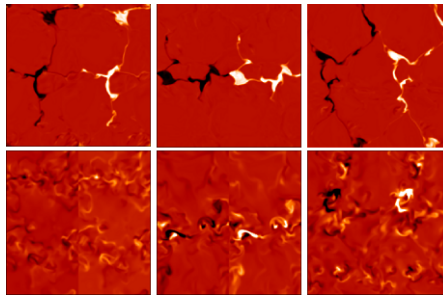


Figure 3.2: As in Fig. 3.1, but for the 2.85 Mm-deep simulation. Horizontal cuts at $z = 0$ (top row) and 2.85 Mm (bottom).

photosphere to 60 km at the lower boundary. The sign of the initial magnetic field changes in stripes of 3 Mm width, yielding four stripes of 3 Mm by 12 Mm of alternating positive and negative polarity. We used set-ups for three different initial vertical magnetic field strengths: $B_{\text{vert}}=200$ G, 500 G and 1000 G. All simulations ran for 60 minutes solar time. This setup uses an equation of state further described in Beeck et al. (2012).

3.3.3 Analysis

The canceling process is studied from the evolution of the vertical component of the magnetic field at the nominal photosphere $z = 0$ of the simulations, $B_z(x, y, t)$. Let x be the direction in which the polarity of the stripes varies, and let \bar{B} be the average in the other horizontal coordinate, y :

$$\bar{B}(x, t) \equiv \langle B_z \rangle_y. \quad (3.1)$$

By gradual mixing of opposite polarities as well as by actual canceling (sect. 3.2.1), the profile of \bar{B} as a function of x smears out with time, and decays in amplitude. An effective diffusivity is measured by comparing this with the time dependence of a matching one-dimensional diffusion problem with an assumed constant diffusion coefficient D . If $B_f(x, t)$ is the field strength of this matching problem, it is governed by the standard diffusion equation

$$\frac{\partial B_f}{\partial t} = D \frac{\partial^2 B_f}{\partial x^2}. \quad (3.2)$$

The initial condition is the striped pattern used in the simulations, with amplitude B_0 and period of length L (two adjacent stripes of opposite polarity, and origin $x = 0$ at the boundary between polarities). The solution of (3.2) is then

$$B_f = \frac{4}{\pi} B_0 \sum_{n=1}^{\infty} \frac{1}{2n-1} \sin(k_n x) e^{-k_n^2 D t}, \quad (3.3)$$

where

$$k_n = (2n-1)2\pi/L. \quad (3.4)$$

This is compared with \bar{B} determined from the simulations and the best fitting value of D determined. This value is a function of t because of the statistical fluctuations in the simulations, but more importantly because the evolution of the field is not a simple 2-D diffusion process. In addition to a different time dependence, the measured values of D are expected to depend on the depth z_b of the lower boundary of the simulations and amplitude B_0 of the initial flux density.

The process of determining best fit values of $D(t, z_b, B_0)$ is done in two different ways. In the straightforward way, which we call ‘direct’, the values of $D(t)$ are determined by matching the profile of $B_f(x)$ to that of $\bar{B}(x)$ by a least-squares process. An example of the resulting best fit is shown in Fig. 3.3.

In the ‘indirect’ method, absolute values $|B|$ are used for the comparison. Their integral over x declines with time due to mixing and canceling of polarities. The comparison with the analytic model yields values for $D(t)$. This process is not exactly

equivalent to the direct method. The action of convective flows produces an initial amplification of the field through ‘wrapping up’ of field lines. This adds some small-scale flux of mixed opposite polarity. The amplification process does not change the net flux through the surface, hence cancels out in the direct method. It has to be accounted for in the indirect method, though.

3.4 RESULTS

3.4.1 Initial vertical magnetic field with uniform $|B_z| = 50$ G

Direct analysis

We applied the direct analysis method to the simulation runs with lower boundary at 2.85 Mm and 10.5 Mm depth, described in section 3.3.2, starting from uniform vertical magnetic field of 50 G, alternating in polarity in stripes of 3 Mm width. Fig 3.4 shows the resulting effective diffusion coefficients for the horizontal resolutions of the 25 km (black lines) and 100 km (green lines) and the two different box depths. After an initial transient of about 10min, which can be attributed to the magnetic field amplification process due to turbulent stretching, the measured effective diffusion coefficient stays almost constant for all simulation runs. The values range from $400 - 600 \text{ km}^2 \text{ s}^{-1}$. The effective coefficients for the simulation run with the higher horizontal resolution of 25 km are slightly lower than with a horizontal resolution of 100 km. This shows that at 100km resolution numerical diffusion still plays a role. The depth of the simulation box does not seem to have a strong influence on the effective coefficients.

Indirect analysis

The evolution of the absolute value of the vertical component, $|B_z|$ is determined not only by the diffusion process, but also by the magnetic field strength amplification due to turbulent flows. In order to quantify this effect and to compensate for it a comparison simulation is run for an initially uniform vertical field without polarity changes, but otherwise identical conditions. The evolution of the surface average of $\langle |B_z| \rangle_u$ in this simulation is shown in Fig. 3.5. As expected from interaction with the convective flow, the amplification effect initially increases rapidly and saturates after a few granule turnover times.

As long as the field is sufficiently weak the amplification is a multiplicative effect (proportional to the initial value). Assuming this to be the case, the corresponding diffusion simulation can be corrected simply for this effect by dividing the mean $\langle |B_z| \rangle$ by the value $\langle |B_z| \rangle_u$ from the comparison.

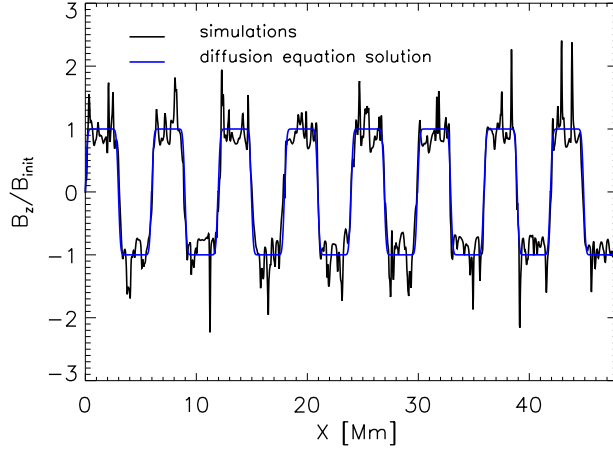


Figure 3.3: Square wave after 1.5 min solar time in a box of 2.85 Mm vertical extent and horizontal resolution of 25 km. The best fit diffusion coefficient is $D = 140 \text{ km}^2 \text{ s}^{-1}$.

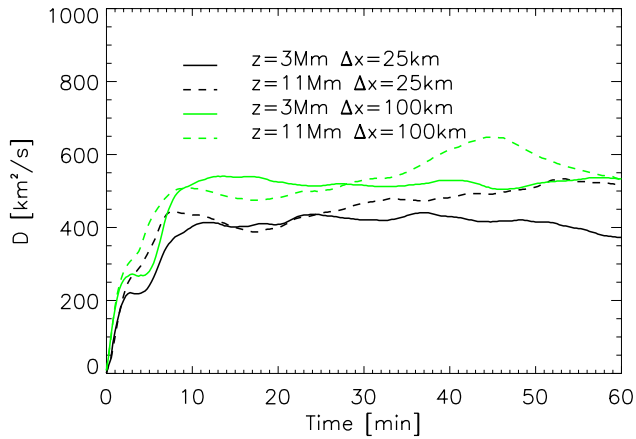


Figure 3.4: Effective diffusion coefficient measured by fit to expression (3.3), (direct analysis method). Vertical initial field $|B_z| = \text{cst.} = 50 \text{ G}$. Dashed lines: box depth 10.5 Mm, solid: box depth 2.85 Mm. Green: horizontal resolution 100 km, black 25 km.

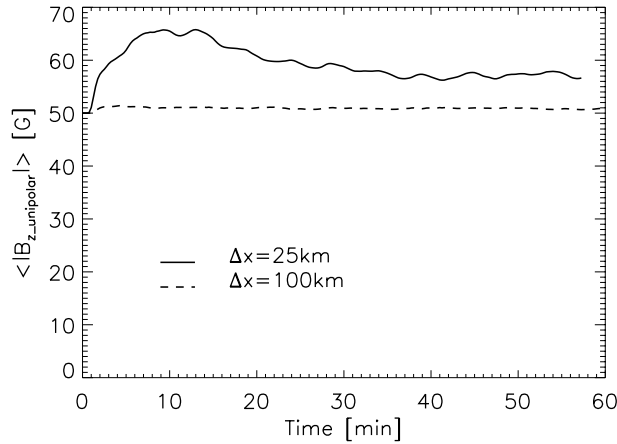


Figure 3.5: Amplification of the mean unsigned flux density by field line stretching in an initially uniform vertical field of 50 G.

Fig. 3.6 shows the evolution of $\langle |B_z| \rangle$ for the simulation of 2.85 Mm vertical extent (black). Overplotted in color are the analytic solutions for 5 different values of the diffusion coefficient. The diffusion coefficients that match vary between 50–250 $\text{km}^2 \text{s}^{-1}$. Simulations in the box of 10.5 Mm depth yield similar values, 20–250 $\text{km}^2 \text{s}^{-1}$. In comparison to the diffusion coefficients obtained with the direct analysis, these are about a factor two lower. At the lower horizontal resolution of 100 km the measurements yield values of 250–400 $\text{km}^2 \text{s}^{-1}$ for both depths of the simulation box. This shows that at least for the unfragmented simulations the depth of the simulation box does not seem to play a role for the diffusion coefficients obtained. This behavior did not match with our expectations, since the freedom of the magnetic field lines to move around should be increasingly limited, the deeper down they are anchored in the convection zone. This lead us to conclude that the spatial scales at which the restoring force would be felt strongly enough are larger than the 3 Mm width of the stripes we simulated the diffusion process for. Therefore we additionally analyzed, as shown in Fig. 3.7, the time evolution of the horizontally averaged vertical magnetic field $\langle |B_z| \rangle$ at the photosphere for a unipolar stripe length of 6 Mm (black, $L=12$ Mm) for a vertical box size of 2.85 Mm (solid) and 10.5 Mm (dashed). For comparison the case of a unipolar stripe length of 3 Mm (green, $L=6$ Mm) is shown there as well. However, no significant difference between the 10.5 Mm and the 2.85 Mm simulation run for $L=12$

Mm is seen, leading in both cases to effective diffusion coefficients of $D = 300 - 600 \text{ km}^2 \text{ s}^{-1}$. The decay time scales seen in Fig. 3.7 are about 3 times longer for $L=12 \text{ Mm}$ than at 6 Mm , instead of the factor 4 predicted by a simple diffusion model.

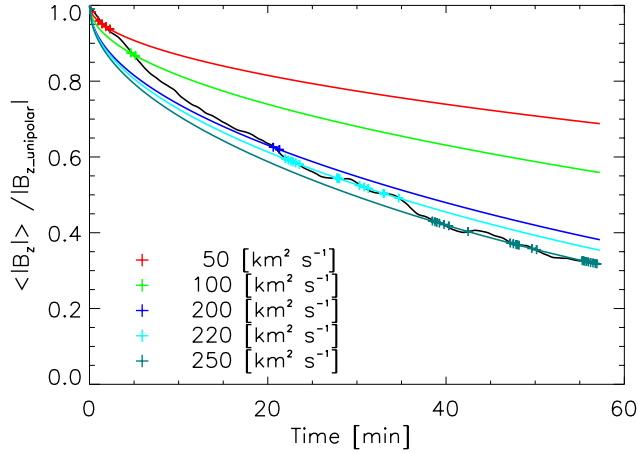


Figure 3.6: Measurement of effective diffusion coefficients by the indirect method. Black: time evolution of the average vertical field strength in a box of 2.85 Mm depth. Initial magnetic field $|B_z| = 50 \text{ G}$, polarity stripe width 3 Mm , horizontal resolution 25 km . Colors: expression (3.3) for 5 values of the assumed diffusion coefficient. Symbols mark the intersection points with the numerical evolution shown in Fig. 3.8.

3.4.2 Initial magnetic field fragmented into kG flux tubes

Fig 3.8 compares results for initial conditions in which the magnetic field is already fragmented into kG flux tubes with those from the uniform initial condition. For the time evolution of the fragmented simulations an average of the three magnetic field representations pictured in Fig. 3.1 and Fig. 3.2, has been taken. Apart from the different initial condition, the simulations are the same as before. The fragmented simulations are normalized by their initial field strength, while the non fragmented simulations are normalized by their unipolar equivalent to correct for the turbulent amplification component (see above). The figure show that the depth of the simulation box does not appear play a major role for the range of parameters covered by the simulations.

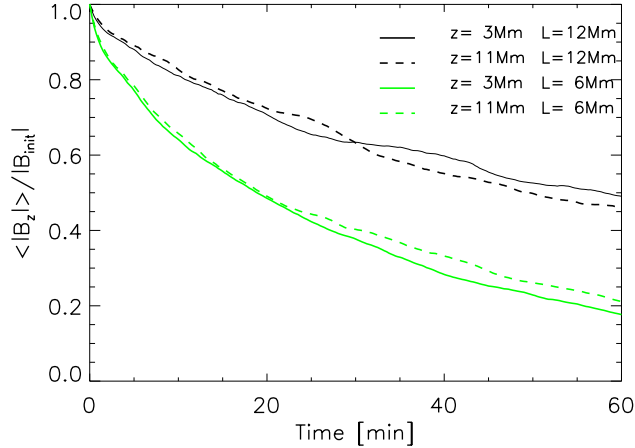


Figure 3.7: Comparison of $\langle |B_z| \rangle$ for a unipolar stripe length of 3 Mm (green, $L=6$ Mm) versus 6 Mm (black, $L=12$ Mm) for a vertical box size of 2.85 Mm (solid) and 10.5 Mm (dashed).

The diffusion coefficients measured with the indirect method the fragmented magnetic field simulation range from $20 - 120 \text{ km}^2 \text{ s}^{-1}$ in the box depth of 2.85 Mm, while for the 10.5 Mm simulation they range from $20 - 60 \text{ km}^2 \text{ s}^{-1}$ (Fig 3.9). The diffusion coefficients for the 10.5 Mm simulation are a bit lower than the ones for the 3 Mm simulation. It is not clear if this can be interpreted as an indicator for a depth dependence, since the statistical fluctuations due to the small box sizes are still large. Nevertheless the values of the diffusion coefficients derived from the fragmented magnetic field simulations are about $100 \text{ km}^2 \text{ s}^{-1}$ lower than for the uniform magnetic field configuration case, which brings them in the range of values observationally obtained for granular flows ($60 - 90 \text{ km}^2 \text{ s}^{-1}$).

3.4.3 Dependence on initial field strength

To test the dependence of the effective diffusion coefficients on field strength, we used simulations with initially vertical fields $|B_{\text{init}}|$ of uniform strength ranging from 20 G to 1000 G. The pattern of alternating polarity stripes of 3 Mm is used as before (Section 3.3.2). Fig. 3.10 shows the decay of the average surface field strength $|B_z|(t)$. Fig 3.11 shows the indirect analysis, which leads to values of $D = 500 - 830 \text{ km}^2 \text{ s}^{-1}$ within the first 60 min of solar time. Comparing this to Fig 3.6 shows that the diffusion coefficients

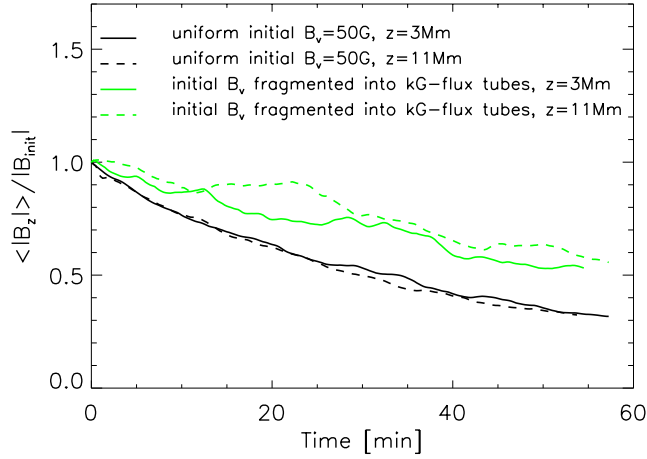


Figure 3.8: Evolution of the mean flux density at the surface for different initial magnetic field configurations and vertical box sizes. Dashed: box depth 10.5 Mm, solid 2.85 Mm. Green: initial magnetic field fragmented into kG-flux tubes. Black: uniform magnetic field configuration of 50 G. Curves corrected for convective amplification effect (see text).

for $|B_{init}| = 500$ G are about a factor two higher than in the 50 G case ($50 - 250 \text{ km}^2 \text{ s}^{-1}$). The striking dependence on field strength can also be seen directly in Fig. 3.10. The decay times of $|B_z|$ to 50% of $|B_{init}|$ are [25, 19, 15, 10, 7, 3] min for $|B_{init}| = [20, 50, 100, 200, 500, 1000]$ G, respectively.

The direct and indirect analysis yield similar results. In the case of $|B_{init}| = 1000$ G the peak effective diffusion coefficient reaches $2600 \text{ km}^2 \text{ s}^{-1}$ during the first couple of minutes. The other simulation runs clearly show how higher initial field strengths lead to higher initial effective diffusion coefficients.

A simple diffusion model one would predict that the diffusion process is independent of the initial field strength, which is clearly not the case here. Comparison of $|B_{init}| = 20$ G with the 50 G case shows that a noticeable dependence is present already a field strength $\approx 50\text{G}$, the value marking the conventional definition of the boundary of active regions. As discussed in 3.2.1, this can be attributed to the dominance of the magnetic field energy density in the atmosphere. The analogy would be to two parallel bar magnets of opposite polarities, where one pole of each is covered by the plasma of the convection zone, while the other pole reaches up through the photosphere. Above the surface the opposite polarities attract each other, but the parts buried in the convec-

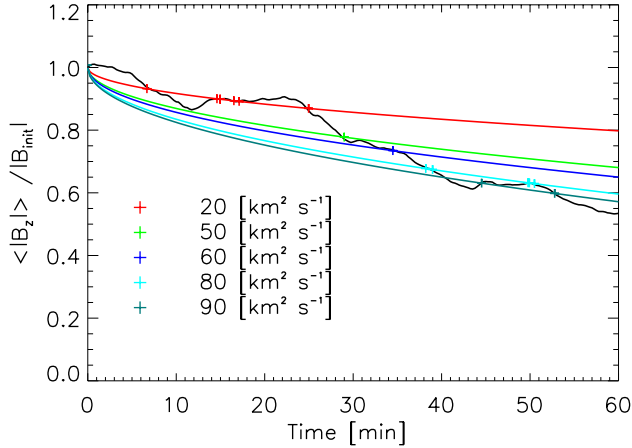


Figure 3.9: As Fig. 3.6, for box depth of 10.5 Mm.

tion zone do not feel each other due to the plasma shielding. Apparently (Fig. 3.10) a field strength of 200 G is high enough for this effect to play a dominant role in the ‘retraction’ process.

3.5 DISCUSSION AND CONCLUSIONS

One of the questions addressed with the simulation is how the effective diffusion coefficient in a mixture of polarities depends on the magnetic field configuration deeper down in the convection zone. To test this the vertical extent of the simulation box was varied, expecting that the deeper down in the convection zone the magnetic field lines were anchored, the more rigid they would act and the more the diffusion process would be delayed. Comparing a simulation extending to a depth of 10.5 Mm below the photosphere with one of 2.85 Mm depth, using the same uniform vertical magnetic field configuration of alternating polarity 3 Mm \times 6 Mm stripes as well as another configuration using 6 Mm \times 6 Mm stripes, the effective diffusion coefficients derived from the simulations of different vertical depth but same unipolar stripe length were essentially the same.

The reason for this might be that the horizontal displacement needed, for a significant restoring force due to the anchoring at the bottom layers to set in, is larger

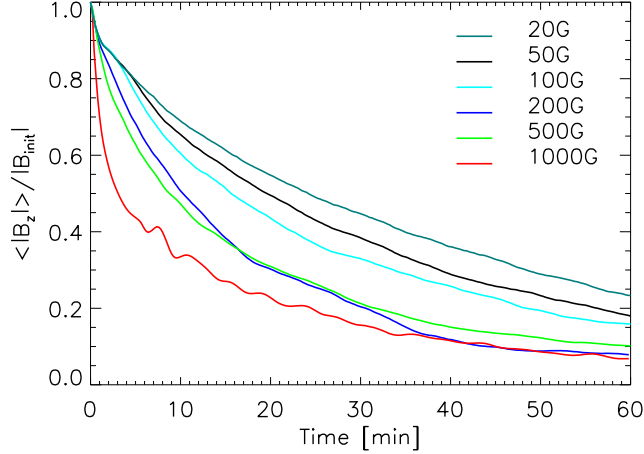


Figure 3.10: Evolution of average surface field strength $\langle |B_z| \rangle(t)$ for B_{init} of 20 G (blue-green), 50 G (black), 100 G (cyan), 200 G (blue), 500 G (green), 1000 G (red). Polarity stripe width 3 Mm, box depth 2.85 Mm/2.7 Mm.

than the width of our unipolar magnetic field stripes. It could also be that the time scales at which the restoring force acts are too long, so that the different polarities have already canceled, before the magnetic field lines can straighten out again. What we found nevertheless, was a dependence on the fragmentation level of the magnetic field. In other words if the magnetic field is fragmented into kG-flux tubes before the diffusion process starts, the diffusion process works slower and the diffusion values shift from $300 - 600 \text{ km}^2 \text{ s}^{-1}$ obtained from the uniform initial field configuration to a values of $20 - 120 \text{ km}^2 \text{ s}^{-1}$, better matching the values obtained observationally for granular flows. For simulations of 10.5 Mm depth with a initially fragmented field, slightly lower diffusion coefficients were derived compared to the 2.85 Mm simulation, but this could be due to statistical noise.

A strong dependence of the decay of the average surface field on the initial vertical field strength was found. An initially uniform magnetic field of 500 G in stripes of alternating polarity showed an initial decay rate about a factor 2 higher than at an initial field strength of 50 G. This deviation decreases asymptotically over time and approaches the diffusion coefficient from the 50 G setup after about 60 min of simulation time. This magnetic field strength dependence is even more pronounced for a magnetic field strength of 1 kG, where the diffusion coefficient is initially a factor of 5 higher

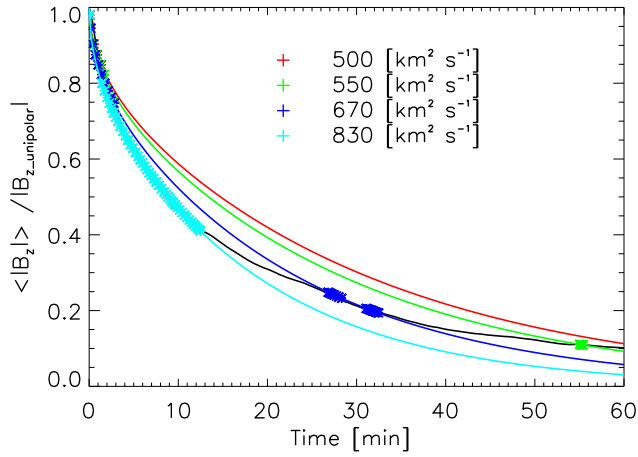


Figure 3.11: Determination of effective diffusion coefficients with the indirect analysis method for an initially uniform vertical magnetic field of 500 G in a 2.7 Mm vertically extended simulation.

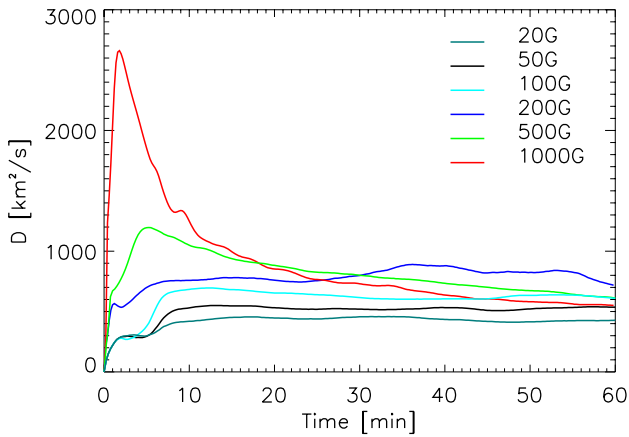


Figure 3.12: Time dependence of effective diffusion coefficients with the direct analysis method, from the data in Fig. 3.10.

than for the 50 G simulation. This behavior is explained by the mutual attraction of the different field polarities which enhanced the diffusion process according to their field strength. It plausibly explains the rapid ‘retraction’ of magnetic flux observed in active region complexes.

REFERENCES

- Afram, N., Unruh, Y. C., Solanki, S. K., Schüssler, M., Lagg, A., Vögler, A. 2011, *A&A*, 526, A120
- Beeck, B., Collet, R., Steffen, M., Asplund, M., Cameron, R. H., Freytag, B., Hayek, W., Ludwig, H.-G., Schüssler, M., 2012, *A&A*, 539, A121
- Berger, T. E., Löfdahl, M. G., Shine, R. A., Title, A. M., 1998, *ApJ*, 506, 439-449
- Bray, R. J. & Loughhead, R. E., 1984, *Science*, 226, 571
- Cameron, R., Vögler, A., Schüssler, M., 2011, *A&A*, 533, A86
- Cheung, M. C. M., Schüssler, M., Tarbell, T. D., Title, A. M., 2008, *ApJ*, 687, 1373-1387
- Fromang, S., Papaloizou, J., Lesur, G., & Heinemann, T. 2007, *A&A*, 476, 1123
- Galsgaard, K. & Nordlund, Å., 1996 *J. Geophys. Res.*, 101, 13445-13460
- Goldreich, P., & Sridhar, S. 1997, *ApJ*, 485, 680
- Gustafsson, B., 1973, *Uppsala Astron. Obs. Ann.*, 5, No.6
- Hagenaar, H. J., Schrijver, C. J., Title, A. M., Shine, R. A., 1999, *ApJ*, 511, 932-944
- Howard, R. & Labonte, B. J., 1981, *Sol. Phys.*, 74, 131-145
- Isobe, H., & Shibata, K., 2004, in *The Solar-B Mission and the Forefront of Solar Physics*, ASP Conference Series, Vol. 325, p63
- Kálmán, B. 2001, *A&A*, 371, 731
- Kubo, M., Low, B. C., & Lites, B. W. 2010a, *ApJ*, 712, 1321
- Kubo, M., Chye Low, B., & Lites, B. 2010b, 38th COSPAR Scientific Assembly, 38, 2828
- Lamb, D. A., DeForest, C. E., Hagenaar, H. J., Parnell, C. E., Welsch, B. T., 2010, *ApJ*, 720, 1405-141
- Komm, R. W., Howard, R. F., Harvey, J. W., 1995, *Sol. Phys.*, 158, 213-225
- Kubat, J. & Karlicky, M., 1986, *Bulletin of the Astronomical Institutes of Czechoslovakia*, 37, 155-163
- Leighton, R. B. 1969, *ApJ*, 156, 1
- Martin, S. F., Livi, S. H. B., & Wang, J. 1985, *Australian Journal of Physics*, 38, 929
- Martin, S. F., 1990, in *Solar Photosphere: Structure, Convection, and Magnetic Fields*, IAU Symposium, Vol. 138, p129
- Moreno-Insertis, F., Caligari, P., & Schüssler, M. 1994, *Sol. Phys.*, 153, 449
- Mosher, J. M., 1977, PhD thesis, California Institute of Technology, Pasadena.
- Nordlund, A., 1982, *A&A*, 107, 1-10
- Rabin, D., Moore, R., & Hagyard, M. J. 1984, *ApJ*, 287, 404
- Sheeley, N.R., 1992, in *The solar cycle*, ed. Harvey, K.L., Astron. Soc. of the Pac., San Francisco, (A.S.P. Conf. Series), Vol. 27, 562
- Smithson, R. C., 1973, *Sol. Phys.*, 29, 365-382

- Schekochihin, A. A., Cowley, S. C., Maron, J. L., & McWilliams, J. C. 2004, *Physical Review Letters*, 92, 054502
- Schekochihin, A. A., Iskakov, A. B., Cowley, S. C., McWilliams, J. C., Proctor, M. R. E., Yousef, T. A., 2007, *New Journal of Physics*, 9, 300
- Schrijver, C. J. & Martin, S. F., 1990, *Sol. Phys.*, 129, 95-112
- Skartlien, R., 2000, *ApJ*, 536, 465-480
- Spruit, H. C. & Zweibel, E. G., 1979, *Sol. Phys.*, 62, 15-22
- Stein, R. F. & Nordlund, Å., 2006, *ApJ*, 642, 1246-1255
- Topka, K. P., Tarbell, T. D., & Title, A. M. 1986, *ApJ*, 306, 304
- Vrabec, D. 1974, in R.G. Athay, ed., *Chromospheric Fine Structure*, IAU Symposium 56, p201
- Wang, H., 1988, *Sol. Phys.*, 117, 343-358
- Wang, Y.-M., Sheeley, N. R., Jr., & Nash, A. G. 1991, *ApJ*, 383, 431
- Yang, S., Zhang, J., Li, T., & Liu, Y. 2012, *ApJ*, 752, L24
- Zwaan, C. 1978, *Sol. Phys.*, 60, 213
- Zwaan, C. 1985, *Sol. Phys.*, 100, 397
- Zwaan, C. 1987, *ARA&A*, 25, 83-111

Chapter 4

Small Scale dynamos on the solar surface: dependence on magnetic Prandtl number

Irina Thaler & H. C. Spruit
submitted to A&A

4.1 INTRODUCTION

In laboratory experiments and numerical simulations of hydrodynamic turbulence, it is found that at sufficiently high Reynold's numbers the statistical properties of the flow become independent of the value of the viscosity (ν). This observation has been enshrined in the standard cascade picture for three-dimensional (but not two-dimensional) turbulence (Kolmogorov 1941). The addition of a magnetic field introduces a second dissipative mechanism, the magnetic diffusivity η . By analogy with the hydrodynamics case, an assumption suggesting itself is that a turbulent magnetic flow would also be insensitive to the value of η , such that it would affect only the small scales in the magnetic field. Experience with numerical MHD simulations, however, has shown this assumption to be unexpectedly problematic. The behavior of turbulent MHD flows, including their bulk transport efficiency and the presence or absence of small-scale dynamo action, appears to vary with details of the problem studied, with the numerical methods used, and in particular to depend on the magnetic Prandtl number of the fluid, $\text{Pr}_m = \nu/\eta$.

The magnetic field at the surface of the Sun is dominated by the sunspot cycle, which is believed to have its source near the base of the convective envelope. At sufficient spatial resolution, a weak field of mixed polarity is also observed. Though it is not clear from the observations if it is a truly separate component, rather than some sort of waste product of the spot cycle, it suggests the possibility that a local small scale turbulent dynamo process is operating near in the surface layers (Durney et al. 1993, Petrovay & Szakaly 1993). This suggestion has been addressed with a number of more idealized turbulent dynamo models and simulations (Cattaneo 1999, Cattaneo et al. 2003). In view of the poorly understood dependence of MHD turbulence on details of the problem studied, these simulations do not yield an unambiguous interpretation of the weak field observed on the Sun. With the advent and spectacular successes of realistic 3-D radiative MHD simulations developed for the solar surface layers (Galsgaard & Nordlund 1996), it has become possible to study the problem numerically for conditions much closer to the solar case, where both Vögler & Schüssler (2007) and Pietarila Graham et al. (2010) reported successful small-scale dynamo generation with such simulations. A range in magnetic Prandtl numbers and Reynolds R_m was investigated, but results were still somewhat inconclusive for the combination of large R_m and small Pr_m . In the work presented here we follow up on these results, with emphasis on the dependence on Pr_m at high resolution.

4.2 DYNAMOS, FLUCTUATING AND NON-, AT LOW Pr_m

The possibility that macroscopic behavior of MHD could depend critically on magnetic Prandtl number was noted already by Balbus and Hawley (1998), in the context of small-scale dynamo action in accretion disks. An often used model for small-scale dynamo action is the ‘fluctuating dynamo’: a flow driven by an assumed external force acting on a large scale and with a random time dependence. It is intended to be generically applicable to MHD turbulence, and believed to be sufficient to prove dynamo action (but not without controversy, see references in Iskakov et al. 2007). Numerical simulations, however (Schekochihin et al. 2002), showed that the presence of self-sustained magnetic field generation in this model depends critically on magnetic Prandtl number, with dynamo action absent when $\text{Pr}_m \leq 1$ (viscosity smaller than magnetic diffusivity). The magnetic Prandtl number divides astrophysical systems in two very different regimes. It is usually either very small, as in the case of stellar convective cores, or very large, as in the interstellar/intracluster medium (Schekochihin et al. 2007). At higher Reynolds numbers or numerical resolution, Iskakov et al. (2007) found dynamo action below $\text{Pr}_m = 1$ in the fluctuating model, at low growth rates. The growth rate found increases with magnetic Reynolds number, but at the lowest Pr_m achieved, ≈ 0.1 , it was still declining with decreasing Pr_m . The authors expressed their belief that the results indicate a flattening of the growth rate to a finite positive value for $\text{Pr}_m \downarrow 0$. Functions that decline continuously to zero would equally fit the data shown in their Fig. 3, however.

The question of dynamo action in fluctuating models therefore does not appear to be settled for astrophysically relevant magnetic Prandtl and Reynolds numbers. The question may actually be academic, however, since the assumption of a random driving force on which it is based is of unknown validity for any physically realistic MHD flow.

A physically realistic yet simple model that does not need an assumed fluctuating forcing is the shearing box model for the flow in an accretion disk. Strong ‘magnetorotational’ turbulence develops in rotating shear flows which are stable in the absence of a magnetic field (such as Keplerian shear). Lesur & Longaretti (2007) and Fromang et al. (2007)(further investigated by Fromang 2010, 2010b, Simon 2011) studied the dependence of magnetorotational turbulence on Pr_m through simulations with explicit viscosity and magnetic diffusivity. The results show that the amount of angular momentum transported increases with the magnetic Prandtl number. A crucial factor was found to be the presence or absence of a (weak) ‘mean vertical field’ (a net flux crossing the disk). In the absence of such a field no dynamo action found at the values $\text{Pr}_m < 1$ that are relevant for most accretion disks.

Since most codes used in astrophysics do not include explicit viscosity or magnetic diffusivity but leave it to the discretization errors or the stabilization algorithms of the

code, the value of $\text{Pr}_m < 1$ to be associated with a simulation is not obvious a priori. The rates of diffusion of momentum and magnetic field can be measured with independent tests of a code, however. Though neither of these represents a physically realistic diffusion coefficient, their ratio would represent an effective magnetic Prandtl number characterizing the numerics. The value found in Fromang et al. (2007) is $\text{Pr}_m \approx 2$; similar numbers have been reported for other codes. This value, in the range where dynamo action is also observed in simulations with explicit diffusivities, explains that magnetorotational turbulence has been obtained in most astrophysical codes. For the results reported below, the code used includes an explicit process for modifying its effective value Pr_m .

The reason for the strong dependence on Pr_m has been discussed in terms of the ordering of the viscous and resistive length scales (cf. Moffatt 1961). For $\text{Pr}_m \gg 1$, the viscous length scale, where the field stretching takes place, is much larger than the resistive one, which plays then a negligible role (Batchelor 1950, Schekochihin et al. 2004). The situation is quite different for $\text{Pr}_m \ll 1$, when the resistive scale is much larger than the viscous scale. In the limit of large conductivity the field stretching as well as the magnetic dissipation grow exponentially and estimating which of these processes develops faster is hardly possible (Finn & Ott 1988).

4.2.1 Transient behavior

A remarkable observation of possible relevance also for the solar case has been made by E. Rempel et al. (2010), who studied the classical shearing box model of magnetorotational dynamo action at $\text{Pr}_m > 1$, for the case where the mean field through the disk vanishes. Dynamo action saturates rapidly (a few orbital time scales) to a statistically steady state, but after a finite time switches off again on an equally fast time scale. Since onset of dynamo action requires a finite seed field to overcome magnetic diffusion, this inactive state is final. The duration of the active phase increases approximately exponentially with increasing R_m .

This kind of behavior has been observed in other chaotic systems and is called type-II supertransient behavior. The switch-off is explained as happening when decay-facilitating fluctuations are by chance simultaneously present in all statistically independent subvolumes of the simulation. This happens more readily at low spatial resolution or Reynolds number. In the presence of a finite net flux threading the disk this effect does not take place, since this flux cannot change (cf. Spruit & Uzdenksy 2005 in connection with net flux in accretion disks). Provided it exceeds the minimum value required for MRI instability to grow, it is sufficient to restart the dynamo process when it happened to start decaying in a supertransient accident. The result would just be a

large fluctuation instead of a switch-off.

Generalizing from this experience, the presence of some low level of magnetic flux from an external source may be essential for small-scale dynamo action at any value of the magnetic Prandtl number. Possible relevance for the Sun is discussed in sect. 4.5.

4.2.2 Experimental evidence

Liquid metals have low magnetic Prandtl numbers (of order 10^{-5}), conveniently in the astrophysically relevant range. Reaching the high Reynolds numbers expected to be needed for dynamo action has been more challenging. The most successful experiment so far has been reported by Monchaux et al. (2007). In a turbulent shearing flow between counter-rotating plates in liquid sodium these authors obtained dynamo action at $R_m \approx 50$ in the form of a steady field with superposed strong fluctuations. This success appeared to be related to a peculiarity of the experimental device. Dynamo action was absent until one of the rotating parts, made of stainless steel (low magnetic permeability), was replaced by an iron part (high permeability and magnetic remanence). The remanent magnetization of the iron part may have played a role. Once magnetized by the steady component of the magnetic field, the iron part would have maintained a minimum field strength in its neighborhood. This is significant in view of the experience (for example in the shearing box simulations mentioned above) that even a weak externally imposed field component strongly facilitates dynamo action. Whatever the precise interpretation, however, the relevance of this experimental result for astrophysics is questionable since astrophysical fluids with the magnetic properties of solid iron are unknown.

Situation for the Sun

Magnetic Prandtl numbers $Pr_m \approx 1$ are accessible with realistic 3D MHD solar surface simulations, and for these values small scale dynamo action has been found (Vögler & Schüssler 2007, Pietarila Graham et al. 2010). In terms of dynamo behavior, $Pr_m = 1$ still belongs to the large magnetic Prandtl number limit, however. In view of the inconclusive results discussed above, the question whether low- Pr_m small scale dynamo action is to be expected on the solar surface is still open.

4.2.3 Indications of solar small-scale dynamo action

Livingston & Harvey (1971) discovered an intrinsically weak small-scale internetwork field on the Sun. It is spread approximately uniformly across the solar disk, and seems

to be independent of the solar cycle. Its properties have been studied in detail by Martin (1988), Martin (1990) and Zirin (1985). Durney et al. (1993) and Petrovay & Szakaly (1993) suggested that this component is due to small scale dynamo action, locally near the solar surface. Alternatively, the weak field component could represent fragments of active regions rising through the convection zone, or as a by-product of the decay of active regions (e.g. Spruit et al. 1987). In this 'decay' hypothesis a correlation between the quiet sun magnetic field and the solar cycle would be expected. The fact that this is not evident in the observations would therefore require that the decay from the large scale magnetic field to the smallest scales exceeds the solar cycle time, in this interpretation (Lites 2011). Parnell et al. (2009) on the other hand find that the magnetic flux distribution between $10^{17} - 10^{23}$ Mx can be described by a single power law function. This would indicate that the whole field is produced by the same process.

Since weak fields tend to be compressed to strong fields by the granulation flow, there is the possibility that (some fraction of) the intrinsically strong small scale magnetic field is unrelated to the sunspot cycle but instead result from a small scale dynamo mechanism. The origin and possible variation of the strong field component is of special interest due to its brightness contribution to the TSI (Schnerr & Spruit 2011, Foukal et al. 2006, Afram et al. 2011, Thaler & Spruit 2014a).

4.3 CALCULATIONS

4.3.1 Numerical methods

The numerical simulations were realized with the 3D magnetohydrodynamics code STAGGER, which was developed by Galsgaard & Nordlund (1996). The code solves the time-dependent magnetohydrodynamics equations by a 6th order finite difference scheme using 5th order interpolations for the spatial derivatives, while the time evolution is done using a 3rd order Runge-Kutta scheme. For every time step the radiative transfer equation is solved at every grid point assuming local thermal equilibrium. This is done by using a Feautrier-like scheme along the rays with two μ angles plus the vertical and four ϕ angles horizontally, which adds up to nine angles in total. To incorporate the wavelength dependence of the absorption coefficient, the Planck function is sorted into four opacity bins. The equation of state table is calculated using a standard program for ionization equilibria and absorption coefficients (Gustafsson et al. 1973) and using opacity distribution functions identical with the ones used by Gustafsson et al. (1975) and are further described in Stein & Nordlund (1998), Nordlund (1982), Nordlund & Stein (1990). For a more detailed description of the STAGGER code see Beek et al. (2012). The horizontal boundaries are periodic, while on the top and

bottom we have open transmitting boundaries. To get the right effective temperature, the density and internal energy of gas flowing in at the lower boundary are kept fixed to control the entropy value. The magnetic field is kept vertical at the lower boundary, thus allowing horizontal displacements of the field lines. At the top boundary the horizontal field components are determined from the vertical component by a potential field extrapolation.

4.3.2 Setup

The setup used consists of a box with horizontal dimensions of 3 Mm \times 3 Mm and 1.3 Mm vertical, extending to 475 km above the photosphere and 836 km below. The initial magnetic field configuration consists of a checkerboard pattern with a vertical magnetic field of alternating polarity and strength of 10 mG or 1 mG. This setup is similar to the one used in Vögler & Schüssler (2007), Pietarila Graham et al. (2010), where in parts of their experiments they used a 4 \times 4 checkerboard in a box with horizontal dimensions of 6 Mm \times 6 Mm with a vertical depth of 1.4 Mm.

4.3.3 Implementation of the magnetic Prandtl parameter in the STAGGER code

The numerical magnetic Prandtl parameter Pm is defined as the ratio between hyperviscosity and magnetic diffusivity and these are implemented in the STAGGER code¹ in the following way:

$$\frac{\partial \rho}{\partial t} = -\nabla \cdot \rho \mathbf{u} \quad (4.1)$$

$$\frac{\partial \mathbf{B}}{\partial t} = -\nabla \times \mathbf{E} \quad (4.2)$$

$$\mathbf{E} = -(\mathbf{u} \times \mathbf{B}) + \eta \mathbf{J} \quad (4.3)$$

$$\mathbf{J} = \nabla \times \mathbf{B} \quad (4.4)$$

$$\frac{\partial \rho \mathbf{u}}{\partial t} = -\nabla \cdot (\rho \mathbf{u} \mathbf{u} + \underline{\underline{\tau}}) - \nabla P + \mathbf{J} \times \mathbf{B} - g \rho \quad (4.5)$$

$$\frac{\partial e}{\partial t} = -\nabla \cdot (e \mathbf{u}) - P \nabla \cdot \mathbf{u} + Q_{\text{cool}} + Q_{\text{visc}} + Q_{\text{Joule}} \quad (4.6)$$

where ρ , \mathbf{u} , \mathbf{B} , \mathbf{E} , η , \mathbf{J} , $\underline{\underline{\tau}}$, e , g , P , Q_{cool} , Q_{visc} , Q_{Joule} are the density, velocity, magnetic field, electric field, magnetic diffusivity, electric current, viscous stress tensor, inter-

¹http://www.astro.ku.dk/~kg/Papers/MHD_code.ps.gz

nal energy, acceleration of gravity, gas pressure, cooling term, viscous dissipation and Joule dissipation, respectively. Regularization of the velocity and magnetic field on small scales is implemented with a hyperviscosity and hyperdiffusion scheme already described in Stein & Nordlund (1998) for the non-magnetic case. The viscous stress is:

$$\tau_{ij} = \frac{1}{2}(e_{ij} + e_{ji}), \quad (4.7)$$

where

$$e_{ij} = \rho[v_j^{(1)}q_j(\partial_j^+ u_i) + v_j^{(2)}]\partial_j^+ u_i, \quad (4.8)$$

$$v_j^{(1)} = \Delta x_j(c_1 c_f + c_2 |u_j|), \quad (4.9)$$

$$v_j^{(2)} = \Delta x_j^2 c_3 |\nabla \cdot u|_-. \quad (4.10)$$

The ∂^+ indicates that the result of the partial derivative is half a grid point above the location of the input value. Δx_j is the grid spacing. $|\nabla \cdot u|_-$ means the absolute value of the negative part of the velocity divergence, so where local convergence occurs. The viscosity contribution $v^{(1)}$ consists of two parts, one is proportional to the fast mode wave c_f and stabilizes weak waves, while the second part prevents from ringing at sharp edges of changing quantities. $v^{(2)}$ is proportional to the velocity jump and stabilizes shocks. c_1, c_2 and c_3 are dimensionless parameters. The hyperdiffusive operator d is then defined the following way:

$$d_x^+(f) = \frac{\max_{x\pm 1} |\Delta^3 f|}{\max_{x\pm 1} |\Delta f|} \partial_x^+(f) = q_x(\partial_x^+(f)) \partial_x^+(f) \quad (4.11)$$

It is proportional to the first derivative, which guarantees positive energy dissipation, since the proportional factor q , defined as the hyperdiffusive quenching function, is positive. $\max_{x\pm 1}$ is the maximum over three points in the derivative direction, $\Delta^3 f$ is the third difference and Δf is the first difference of the variable. Making d proportional to the third derivative stabilizes waves and advection, while it damps out high wavenumber perturbations. The resistive part of the electric field is treated in the same spirit:

$$E_x^\eta = \left\{ \frac{1}{2} [\eta_y^{(1)} q_y(J_x) + \eta_z^{(1)} q_z(J_x)] + \frac{1}{2} [\eta_y^{(2)} + \eta_z^{(2)}] \right\} J_x, \quad (4.12)$$

and by cyclic permutation for the other two E-field components. Here

$$\eta_j^{(1)} = \frac{\Delta x_j}{Pm} (c_1 c_f + c_2 |u_j|), \quad (4.13)$$

$$\eta_j^{(2)} = \frac{\Delta x_j^2}{Pm} c_3 |\nabla_{\perp} \cdot u|_{-}. \quad (4.14)$$

$$(4.15)$$

In this way, the treatment of numerical stabilization and hyperdiffusivity is closely analogous for the flow field and the magnetic field. The parameter Pm is then a numerical equivalent of the magnetic Prandtl number. Its exact quantitative level cannot be identified directly with a real Prandtl number, however.

4.4 RESULTS

A set of simulations was made to investigate the dependence of magnetic field amplification on the numerical magnetic Prandtl parameter Pm . Dependence on numerical resolution, as a proxy for dependence on Reynolds number, was investigated with an additional set of three runs.

Fig. 4.1 shows the dependence on Pm found. The boundary between presence and absence of dynamo action appears to be close to $Pm = 2$. In the case $Pm = 5$ the amplitude of the field increases exponentially with a growth time of ~ 200 min saturating at $\langle B^2 \rangle^{1/2} \approx 115$ G.

Fig 4.3 shows simulation runs for an initial state of 10 mG and a numerical Prandtl parameter $Pm = 1$ for different numerical resolutions. The code uses a uniform resolution in the two horizontal coordinates (Δx in Fig. 4.3); the vertical resolution is non-uniform. It is chosen highest near the photosphere where cooling by radiation drives the flows (grid spacing at the photosphere is denoted by Δz_0 in the Figure). As the Figure shows, the decay time increases with increasing resolution, from about 50 minutes at $\delta x = 14$ km to 70 min at 7 km. At the (expensive) resolution of 3.5 km the limited time coverage of the run indicates decay at an even slower rate. Extrapolation to even higher resolution is uncertain from these data, however.

Since the dissipation built into the code decreases with decreasing grid spacing, the inverse of resolution is a numerical analog of a Reynolds number. Since the nature of the numerical dissipation is rather different from physical dissipation and depends strongly on the order of the spatial discretization used, however, it is not possible to translate the grid spacing in our simulations meaningfully into ‘effective’ magnetic Reynolds numbers. The uncertainty is less in the case of the magnetic Prandtl number,

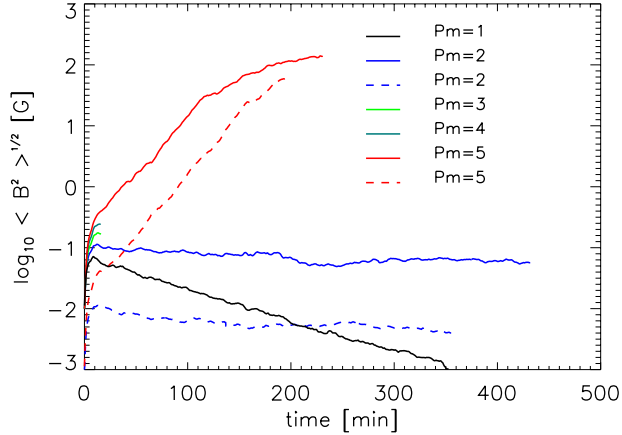


Figure 4.1: Evolution of $\langle B^2 \rangle^{1/2}$ as a function of the numerical magnetic Prandtl parameter Pm for a numerical resolution of $\Delta x = 7$ km and $\Delta z_0 = 6$ km. Solid: initial field strength 10 mG, dashed 1 mG.

since it measures the ratio of two quantities which, though both artificial, are based on the same algorithm.

4.5 DISCUSSION AND CONCLUSIONS

The results show the same trends as found in the shearing box simulations discussed in the Introduction: the growth rate of dynamo action increases with magnetic Prandtl number, and no dynamo action is detected below a critical value $Pm \approx 1$. As Fig. 4.3 shows, the growth rate appears to increase with numerical resolution, however, and the corresponding critical Pm may increase as well. The combination of high resolution and low Pm required to study this is numerically challenging.

The growth rate we find for the case $Pm = 5$ is comparable with that reported by Pietarila Graham et al. (2010) for their $P_{M,\text{eff}} \approx 2$. Since the numerical Prandtl parameter is not identical with the physical Prandtl number, but depends on the implementation of energy dissipation at small scales in the code, a dependence of the effective Prandtl number scale on code used was to be expected.

Assuming a difference of a factor ≈ 2 between the scales, the lowest $P_{M,\text{eff}} \approx 1$ reported in Pietarila Graham et al. (2010) would correspond to $Pm \approx 2$ in our simu-

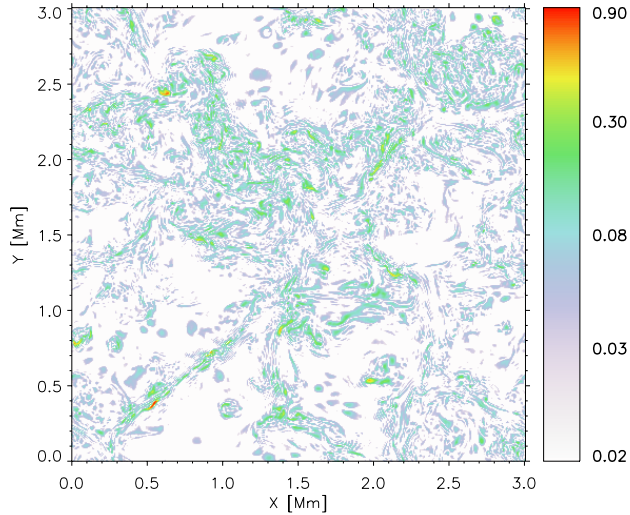


Figure 4.2: $|B_z|$ in kG at the photosphere for $Pm = 5$ after $t=231$ min for a numerical resolution of $\Delta x = 7$ km and $\Delta z_0 = 6$ km. The image scale is exponential ($val^{0.25}$) to amplify small structures and still be able to clearly identify large values

lations, which we find to be above the threshold for dynamo action. The fact that all results reported by Pietarila Graham et al. show dynamo action is thus consistent with our results.

Taken together, these results make clear that the question of small scale dynamo action in the surface layers of the Sun is still unresolved. As in the case of the fluctuating dynamo model discussed in the Introduction, the limit of a high magnetic Reynolds number (or numerical resolution) combined with low Prandtl number cannot be reliably extrapolated from currently available results.

4.5.1 Relation between intrinsically weak and strong surface fields

Given that the small scale dynamo acts and produces the weak field component, could (some fraction of) the intrinsically strong component originate from it as well? From the results obtained with our simulations this seems unlikely. Our simulation with $Pm = 5$ converged to an average absolute vertical magnetic field strength of about 30 G

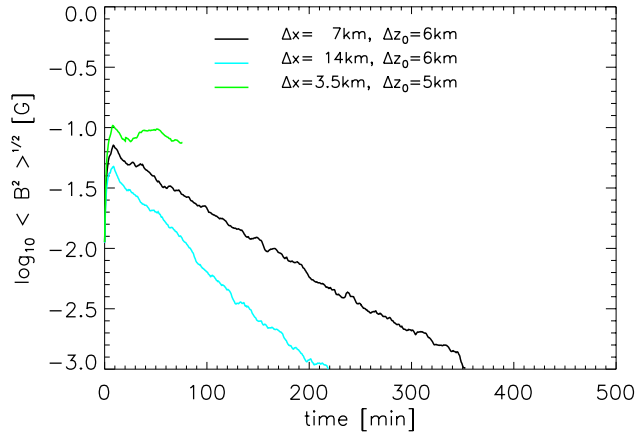


Figure 4.3: Evolution of $\langle B^2 \rangle^{1/2}$ as a function of numerical resolution, for $Pm = 1$ and initial field strength 10 mG.

at the photosphere (after 230 min simulation time) and small scale magnetic structures of surface fields up to 930 G evolved (see Fig. 4.2), nevertheless no magnetic bright points can be found in bolometric intensity maps, which has as well been reported by Vögler & Schüssler (2007). The reason for this behavior might be that in this mixed-polarity simulations magnetic features of high vertical field strength usually are surrounded by the opposite polarity field and along with the ongoing magnetic field compression process, part of the magnetic flux cancels out. This means that magnetic structures of high field strength remain too small and short lived to be seen as bright features. Contrary to that, in unipolar simulations of the same kind with the same average magnetic field strength, strong magnetic elements were detected after about 10min of simulation time, starting from a homogenous background field (Thaler & Spruit 2014a). Therefore it seems likely that a small scale surface dynamo process, even if actually takes place on the Sun, is not responsible for much of the intrinsically strong field component.

4.5.2 Role of an imposed weak net flux

If the experience with the shearing boxes studied in accretion physics are an indication, the presence of even a relatively weak mean flux density in the simulation may have

a significant effect on a dynamo process. In the case of the Sun, remnants of active regions spreading across the surface might have a similar effect, lowering the threshold for dynamo action. The behavior in the limit of low P_m and high R_m at zero mean flux would then be somewhat academic for the solar case. Simulations to address small scale dynamo action in the presence of a dispersed strong field component might then be more relevant. In this case, the issue of the ‘supertransient’ behavior discussed in section 4.2.1 might also be relevant, according to the following speculative scenario.

If it were the case that for solar conditions ($R_m \sim 10^7$, $Pr_m \sim 10^{-5}$) dynamo behavior does not occur in the absence of a mean field, the presence of a weak average field supplied by detritus from active regions could keep a small scale dynamo going. Depending on where this ‘catalytic’ field component is present, this might result in small scale dynamo action to be intermittent, with dynamo action switching off from time to time in supertransients. This would show itself in the form of patchy activity, rather than being present around each and every granule on the surface as a local convective dynamo action would predict.

REFERENCES

- Afram, N., Unruh, Y. C., Solanki, S. K., Schüssler, M., Lagg, A., Vögler, A. 2011, *A&A*, 526, A120
- Batchelor, G. K., 1950, *Royal Society of London Proceedings Series A*, 201, 405-416
- Balbus, S. A. and Hawley, J. F., 1991, *ApJ*, 376, 214
- Balbus, S. A., & Hawley, J. F. 1998, *Reviews of Modern Physics*, 70, 1
- Beeck, B., Collet, R., Steffen, M., Asplund, M., Cameron, R. H., Freytag, B., Hayek, W., Ludwig, H.-G., Schüssler, M., 2012, *A&A*, 539, A121
- Cattaneo, F., 1999, *ApJ*, 515, L39-L49
- Cattaneo, F., 2003, *ApJ*, 588, L1183-L1198
- Durney, B. R., De Young, D. S., & Roxburgh, I. W. 1993, *Sol. Phys.*, 145, 207
- Finn, J. M. & Ott, E., 1988, *Physical Review Letters*, 60, 760-763
- Foukal, P., Fröhlich, C., Spruit, H., Wigley, T. M. L., 2006, *Nature*, 443, 161-166
- Fromang, S. and Papaloizou, J., Lesur, G., Heinemann, T., 2007, *A&A*, 476, 1123
- Fromang, S., 2010, *A&A*, 514, L5
- Fromang, S. and Papaloizou, J. and Lesur, G. and Heinemann, T. 2010, *EAS Publications Series*, 41, 167
- Galloway, D. J., Proctor, M. R. E., 1992, *Nature*, 356, 691-693
- Galsgaard, K. & Nordlund, Å., 1996, *J. Geophys. Res.*, 101, 13445
- Gustafsson, B., 1973, *Uppsala Astron. Obs. Ann*, 5

- Gustafsson, B., Bell, R. A., Eriksson, K., Nordlund, A., 1975, *A&A*, 42, 407-432
- Iskakov, A. B., Schekochihin, A. A., Cowley, S. C., McWilliams, J. C., Proctor, M. R. E., 2007, *Phys. Rev. Lett.*, 98, 208501
- Kolmogorov, A., 1941, *Akademiia Nauk SSSR Doklady*, 30, 301
- Lesur, G. & Longaretti, P.-Y., 2007, *MNRAS*, 378, 1471
- Lites, B. W. 2011, *ApJ*, 737, 52
- Livingston, W. & Harvey, J., 1971, *IAU Symposium*, 43, 51,
- Martin, S.F., 1988, *Sol. Phys.*, 117, 243
- Martin, S.F., 1990, in J.-O. Stenflo (Ed.), *The Solar Photosphere: Structure, Convection and Magnetic Fields*, Proceedings IAU Symposium 138 (Kiev), Kluwer, Dordrecht, p.129
- Meneguzzi, M., Frisch, U., Pouquet, A., 1981, *Physical Review Letters*, 47, 1060
- Moffatt, H. K., 1961, *Journal of Fluid Mechanics*, 11, 625-635
- Monchaux, R., Berhanu, M., Bourgoïn, M., Moulin, M., Odier, P., Pinton, J.-F., Volk, R., Fauve, S., Mordant, N., Pétrélis, F., Chiffaudel, A., Daviaud, F., Dubrulle, B., Gasquet, C., Marié, L., Ravelet, F., 2007, *Phys. Rev. Lett.*, 98, 044502
- Nordlund, Å., 1982, *A&A*, 107, 1-10
- Nordlund, Å. & Stein, R. F., 1990, *Computer Physics Communications*, 59, 119-125
- Parnell, C. E., DeForest, C. E., Hagenaar, H. J., Johnston, B. A., Lamb, D. A., Welsch, B. T., 2009, *ApJ*, 698, 75-82
- Petrovay, K. & Szakaly, G., 1993, *A&A*, 274, 543
- Pietarila Graham, J., Cameron, R., Schüssler, M., 2010, *ApJ*, 714, 1606-1616
- Ponty, Y. and Mininni, P. D., Montgomery, D. C., Pinton, J.-F., Politano, H., Pouquet, A., 2005, *Phys. Rev. Lett.*, 94, 164502
- Rempel, E. L., Lesur, G., Proctor, M. R. E., 2010, *Physical Review Letters*, 105, 044501
- Schekochihin, A. A., Maron, J. L., Cowley, S. C., McWilliams, J. C., 2002, *ApJ*, 576, 806
- Schekochihin, A. A., Cowley, S. C., Taylor, S. F., Maron, J. L., McWilliams, J. C., 2004, *ApJ*, 612, 276
- Simon, J. B., Hawley, J. F., Beckwith, K., 2011, *ApJ*, 730, 94
- Schekochihin, A. A., Iskakov, A. B., Cowley, S. C., McWilliams, J. C., Proctor, M. R. E., Yousef, T. A., 2007, *New Journal of Physics*, 9, 300
- Schnerr, R. S. & Spruit, H. C., 2011, *A&A*, 532, A136
- Spruit, H. C., Title, A. M., van Ballegoijen, A. A., 1987, *Sol. Phys.*, 110, 115-128
- Spruit, H. C., & Uzdensky, D. A. 2005, *ApJ*, 629, 960
- Stein, R. F. & Nordlund, A., 1998, *ApJ*, 499, 914
- Thaler, I. & Spruit 2014a, *A&A* in press
- Thaler, I. & Spruit 2014b, submitted for publication in *A&A*
- Vögler, A., Schüssler, M., 2007, *A&A*, 465, L43-L46
- Zirin, H., 1985, *Australian Journal of Physics*, 38, 961-969

Chapter 5

Sunspots

5.1 WHY SUNSPOTS ARE INTERESTING?

As strong magnetic features sunspots are easy detectable indicators of global solar dynamo processes and as their temperature is about 2000 K below the average solar surface temperature, they directly have an influence the total solar irradiance. Though the current variations of the total solar irradiance during on sunspot cycle are not large enough to have any direct effect on the earth's climate we do not understand solar cycle processes well enough to extrapolate to the past or future. And therefore, understanding what determines the life time of a sunspot as well as what determines their ratio between penumbra/umbra is inevitable to be able to predict solar irradiance variations.

5.2 HOW DO SUNSPOTS LOOK BELOW THE SURFACE- THE ANCHORING PROBLEM

Because magnetic fields are divergence-free, field lines have no ends and are intrinsically three-dimensional. Field lines continue above and below the observed surface. However, different ideas exist for how the magnetic field in a sunspot looks like below the surface. One of them is that the magnetic field of a sunspot immediately fragments below the surface and is hold together only by an inward flow (Parker 1979). In this picture the excess heat due to a blocked heat flux would be minimized and therefore also the force needed to keep the sunspot together would be reduced (Spruit 1981). But the question would be, if the unobserved inward flow would be able to keep the magnetic flux together against the expected fluting instabilities (Schüssler 1984). Due to Duvall et al. (1996) Parker's model got a lot of attention again, since with helioseismic interference a huge downflow around a sunspot has been detected. Nevertheless in later measurements this downflow could not be found anymore (e.g. Gizon et al. 2009,

Gizon et al. 2010).

The more generally accepted picture is, that the sunspot persists as one magnetic flux tube which is anchored at the base of the convection zone (already implicit in Cowling 1953, and developed by Babcock 1963; Leighton 1969; Spruit 1983). From numerical simulations of emerging flux tubes the field strength at the bottom of the convection zone is thought to be around 80 kG (D'Silva & Choudhuri 1993, Caligari et al. 1995). This would mean any change at the bottom of the convection zone would need 5 days to propagate to the photosphere, as that would be the travel time for an Alfvén wave (Moradi et al. 2010). Since the conditions at the bottom of the convection zone are known to change on this time scale and small spots live around that time, the question is how large sunspots are able to survive for several months though the conditions at the bottom change. These lead several people therefore to propose that these sunspots get dynamically disconnected from the bottom (e.g. Schüssler & Rempel 2005)

5.2.1 How do sunspots appear at the photosphere?

Sunspots vary a lot in their form and size. They can extend to a diameter of 50 Mm or more where the umbra, the central dark area, is usually contributing around 20% to the total spot diameter. The intense magnetic field present in the umbra blocks convection, so that the vertical upflow velocities are around 25 m/s compared to 1 km/s in the case of normal granulation (Beckers 1977). This leads to a luminosity which is around $\approx 20\%$ to that of the quiet sun and corresponds to an effective temperature of 4000K. This luminosity is still too high to be entirely explained by the radiative heating by the surroundings. The missing heat flux is now known to be transported by umbral dots, which are according to Parker's umbral gap model (Parker 1979) gaps in the magnetic field just below the surface in a way that field free convection transports heat up. Umbral dots usually have sizes of half an arcsecond or less and upflow velocities of a few hundred m/s. Furthermore the magnetic field in the umbral dots is much weaker than in the umbral background (Socas-Navarro et al. 2004; Rimmele 2004, Rimmele 2008; Bharti et al. 2007).

The penumbra is seen as a brighter ring surrounding the dark umbra, having around 75 % of the heat flux of the normal granulation, leading to a temperature of 5275K. Although lots of observations are available from this region, there is still a lot of debate going on about the theoretical understanding of the penumbra structure based on observations. The reason for that are rapid changes of the inclination angle of the magnetic field (Beckers & Schröter 1969; Lites et al. 1990; Schmidt et al. 1992; and Title et al. 1993) as well as of the Evershed flow with depth (SanchezAlmeida et al. 1992). Apart from that, the Evershed flow seems to be locally transient and consisting of ve-

locity packets repeating themselves irregularly in time (Shine et al. 1994, Rimmele 1994, RouppevanderVoort 2003). Furthermore the scales of the penumbral structure are quite small compared to those of most observations. Via measuring Stokes profiles and using model atmospheres which reproduce the observed profiles (inversion techniques) one could guess the penumbra subsurface structure, nevertheless there is more than one possible combination of assumptions which could lead to the observed profile. For example Westendorp et al. (2001a), Westendorp et al. (2001b) were able to reproduce observations with a model atmosphere where the magnetic field strength increases with height, while Martínez Pillet (2000) reproduced the same observations with a more vertical magnetic field strength decreasing with height. The observed velocities in the penumbra are mainly horizontal and the vertical upflow velocities are much too small to explain the observed heat flux. It has been suggested that the observed magnetic structures are very shallow and therefore the observed heat flux is mainly maintained by radiation of the underlying convection zone. But since the penumbral magnetic field is not only horizontal, it must extend to deeper layers, which would then block convection. Several models have been developed to explain the observed heat flux, the striation and the origin of the radial outflow in the penumbra. It is obvious that this must be subsurface processes which are still lacking theoretical understanding. Spruit & Scharmer (2006) extended the idea of gap field free convection originally developed by Parker (1979) to explain the umbral heat flux to further explain the observed intensity-velocity correlation of the penumbra. In their model they picture the penumbral filaments caused by convection in field-free, radially aligned gaps just below the visible surface of the penumbra, which gives an explanation of the large heat flux and the low vertical velocities observed in the penumbra. Schlichenmaier et al. (1998) modeled the filamentary structure of the penumbra using the thin flux tube approximation (based on the siphon flow of Meyer & Schmidt (1968) where a flux which is located initially at the magnetopause gets heated up by the hotter quiet sun, which makes it bend horizontally and leads to an outward flow. This model matches observations of the Evershed flow very well, but studies from Schlichenmaier & Solanki (2003) showed that it would be very hard in this model to uniformly heat up the penumbra as it is observed. Others tried to explain the observed penumbra structure by turbulent pumping (Recent magneto-convection studies by Thomas et al. (2002a), Thomas et al. (2002b), Weiss et al. (2004), and Brummell et al. (2008), which means that turbulent convection keeps the magnetic field submerged outside the spot and lead to the observed local variations of the inclination angles of the magnetic field. Nevertheless very little flux of the other polarity has been observed so far which makes it unlikely that this is the dominant mechanism. Because of all this ambiguities in the description of the subsurface processes happening in the penumbra, it would be of great advantage to be able to get a 3d picture which gets accessible when doing 3D MHD simulations of

a sunspot.

5.2.2 Sunspot modeling

Recently it has become possible to perform realistic 3d MHD simulations with a realistic equation of state of pores (Bercik et al. 2003, Cameron et al. 2007, Kitiashvili et al. 2010) as well as of a sunspot umbra (Schüssler & Vögler 2006), stripes of sunspots (Heinemann et al. 2007, Rempel et al. 2009b) as well as of whole sunspots (Rempel et al. 2009a, Rempel 2011a, Rempel 2011b). Sunspots do not form on their own in realistic solar surface simulations, just if sufficient magnetic flux is present. For them to be simulated in a self-consistent manner, one would have carry out flux emergence simulations, which has not been done yet. So far in the sunspot simulations performed an initial magnetic field configuration mimicking the magnetic field configuration present inside of a sunspot have been performed. On the solar surface they look convincingly real. They are very successful in describing the sunspot fine structure at the photosphere. Nevertheless there are quite some subsurface features which have not yet been seen in simulations so far. This is connected to the fact that simulation times are too short, as further described in the next section.

5.2.3 Life time of a sunspot in simulations

Current sunspot models do improve our understanding about the fine structure of sunspots at the solar surface, but concerning the subsurface structure of a sunspot, questions like the origin of the moat flow, which is a large scale outflow surrounding sunspots on a photospheric level (Sheeley 1969; Harvey & Harvey 1973), and its possible connection to the Evershed flow were not answered yet. The limiting factor have been very short simulation times and small box sizes. Most of the sunspot simulations done so far, extend vertically to a depth of 6 Mm below the photosphere and are stable for around 3-6 hours simulation time (Rempel 2011a, Rempel 2012, Rempel et al. 2009a). What limits the life time of a sunspot are fluting instabilities, which lead nonmagnetic material to enter the sunspot area and finally cause the dispersion of the sunspot. The time scale at which the fluting instability works, depends on the convective timescale, and the convective time scale increases with depth. So the deeper down to the convection zone sunspot simulations extend, the more efficiently the magnetic field is anchored and therefore the longer a sunspot is expected to live. This has been shown by Rempel (2011b), where the influence of the extension of the simulation box on the life time of a sunspot has been studied. The longest simulation run was lasting for 48 h with a box which extended vertically down to 16 Mm. They compared this simulation with a

sunspot simulation which was only 6 Mm deep. Most of the flux has dispersed in the 6 Mm simulation after a run time of 6 h, while in the 16 Mm deep simulation this happens only after 48 h. But in simulations the life time of a sunspot not only depends on the depth of the convection box, but also on the initial field configuration, the bottom boundary conditions for the velocity flows, magnetic field and the pressure. The life time of a sunspot could furthermore be dependent on the presence of an penumbra, as was suggested by Meyer et al. (1977). Since the long time scale simulation of Rempel (2011b) ran at low resolution, no penumbra had developed and therefore its influence on the life time of a sunspot was not studied.

5.3 ADDITIONAL BOUNDARY FORCE INCREASES STABILITY OF A SUNSPOT?

As already mentioned in the previous section, it is desirable to have longer sunspot simulations to investigate physical processes which need longer simulation times. One way of doing so is anchoring the magnetic field lines deeper down in the convection zone by extending the vertical box dimensions. Another possibility would be to mimic the anchoring of the field lines by an additional force at the lower boundary and see if that can prolong the life time of a sunspot in the same way. This would have the advantage of saving computational power. In the upcoming section this kind of attempt has been investigated.

5.3.1 Numerical Methods

The numerical simulations were realized with the 3d magnetohydrodynamics code STAGGER developed by Galsgaard & Nordlund (1996). The code solves the time-dependent magnetohydrodynamics equations by a 6th order finite difference scheme using 5th order interpolations for the spatial derivatives, while the time evolution is done using a 3rd order Runge-Kutta scheme. For every time step the radiative transfer equation is solved at every grid point assuming local thermal equilibrium. This is done by using a Feautrier-like scheme along the rays with two μ -angles plus the vertical and four ϕ -angles horizontally, which adds up to nine angles in total. The wavelength dependence of the absorption coefficient is taken into account by the opacity binning method (Nordlund 1982, Skartlien 2000). The equation of state table used for all simulations was calculated using a standard program for ionization equilibria and absorption coefficients (Gustafsson 1973). The horizontal boundaries are periodic, while on the top and bottom we have open transmitting boundaries. The effective temperature of the

surface is controlled in the standard way (Galsgaard & Nordlund 1996) by adjusting the entropy of inflowing material at the lower boundary. The magnetic field is kept vertical at the lower boundary. At the top a potential field extrapolation is implemented as boundary condition.

5.3.2 Set-up

Initial sunspot configuration

For the sunspot simulation we took a hydrodynamical snapshot which had the horizontal dimensions of $96 \text{ Mm} \times 6 \text{ Mm}$ and 10.5 Mm vertically. The simulation box extended vertically 475 km above the photosphere and 10.0 Mm below the photosphere. The horizontal resolution was 100 km , while the vertical one is non equidistant with the highest resolution at the photosphere with 27 km and lowest at the bottom of the simulation box with 124 km . The initial sunspot configuration was computed the following way: We chose the values for the ratio of the gas pressure to the magnetic pressure, β , at the top of the simulation box to be $\beta = 0.1$ and $\beta = 20$ at the bottom of the simulation box and assumed a smooth transition of this values in between. With the beta-profile and a mean vertical gas pressure at a every depth level, an initial vertical field strength of the sunspot can be calculated. By further defining the radius of the sunspot at the photosphere, the width of the sunspot as a function of depth can be computed. Assuming this initial sunspot radius profile, a vector potential is calculated, from which further on all magnetic field components can be derived consistently. The first two components of the vector potential A_x and A_y are set to zero. The last component of the vector potential, A_z , is defined by a function which varies along the long horizontal direction of the simulation box and with depth. The function is monotonically increasing outside of the sunspot diameter, while inside the sunspot radius it is a monotonically decreasing function. The steepness of the function depends on depth, but is chosen in a way that the derivative along the long horizontal, which creates the vertical component of the magnetic field, has the desired value at the photosphere. From the vector potential the horizontal magnetic field components can be calculated, which leads to a zero horizontal magnetic field component along the short horizontal direction of the simulation box is zero. With the mean stratifications of density, temperature and pressure taken from a hydrodynamical snapshot, these quantities can as well be calculated inside the sunspot using the ideal gas law and hydrostatic equilibrium equation. Assuming a Wilson depression of 400 km , the initial vertical magnetic field strength at the photosphere is $B_z = 1.3 \text{ kG}$ and the radius of the sunspot is $r = 14 \text{ Mm}$, which leads to a magnetic flux of $\phi = 2.2 \times 10^{21} \text{ Mx}$. This initial sunspot configuration was used for three different simulation runs. Two simulations were performed with an

additional force perturbing the magnetic field configuration of the sunspot at a depth of 10 Mm below the photosphere (as further described in the next Section), while the other simulation was ran without any perturbation force as a reference case to compare to. All simulations ran for 120 min solar time. The additional force at the lower boundary was switched on only after 33 min of simulation time starting from the initial sunspot simulation.

Force description

Our goal was to increase the life time of a sunspot by artificially holding the field lines of the sunspot together at the lower boundary. This was done by modifying the Lorentz force in x-direction at every time step. The net Lorentz force acting on a fluid can be written as $F = \frac{B^2 \mathbf{n}}{8\pi} - \frac{\mathbf{B}B_n}{4\pi}$, where \mathbf{n} is the normal to the surface and B_n is the magnetic field component along \mathbf{n} . Since a sunspot only has a magnetic field component in the vertical direction at the lower boundary, and we are interested in displacements of the vertical field lines in x-direction, as they would lead to a disruption of sunspot this leads to a Lorentz force $F_{Lx} = \frac{B^2 \mathbf{e}_x}{8\pi}$. By artificially reducing this component of the Lorentz force, the force exerted by the volume on its surroundings is reduced, which leads to a compression of the magnetic field. We had two simulation runs where we applied two slightly different forces. The difference between them is illustrated in Figure 5.3.2, which shows the dependence of the modulating force on the magnetic field strength. For the ‘parable force’ F_p (black line) we considered a force dependence on the square of the magnetic field strength in form of a parable, while for the other force F_{ps} we considered a constant force value below B_0^2 (green line). Implementing the modulating force in this way, prevents from amplifying the magnetic field to very high values which would be unphysical and could lead to numerical problems. F_{max} is the maximum Lorentz force normally found in a sunspot at this depth in our simulation setup. Another consideration was, that the modulating force should not act everywhere over the horizontal layer, but only close to the sunspot, since one doesn’t want to gather magnetic field from everywhere. This was realized by the function k , which increases linearly from zero at the center of the sunspot up to 1 at a distance of 0.75 sunspot radii and then decreases to zero at 1.5 sunspot radii again. The formula for F_p is shown in equations 5.1. ε is a parameter to adjust the strength of the modulating force, while h is the width of the layer over which the Lorentz force is modulated and R is the sunspot radius. B_x , B_y and B_z are the magnetic field components in the different directions and a and b are the parable parameters. B_0 is set to 75 kG, which is the average field strength of the sunspot at 10.5 Mm at the beginning of the sunspot simulation. In Fig. 5.3.2 the Lorentz force in x-direction is shown for an example case before manipulation (black line), after manipulation (red line), as well as the modulation of the Lorentz force ΔF_{Lx}

(green line) itself. The sunspot center is at the zero point of the horizontal coordinate.

$$\begin{aligned}
 B_d &= B_x^2 + B_y^2 + B_z^2 \\
 a &= -\frac{F_{max}}{B_0^4} \\
 b &= -2a \cdot B_0^2 \\
 F_{px} &= a \cdot B_d^2 + b \cdot B_d \\
 \Delta F_{Lx} &= \frac{k \cdot \varepsilon \cdot F_{px}}{(\Delta h \cdot R)} \\
 F_{Lx_{modulated}} &= F_{Lx} - \Delta F_{Lx}
 \end{aligned} \tag{5.1}$$

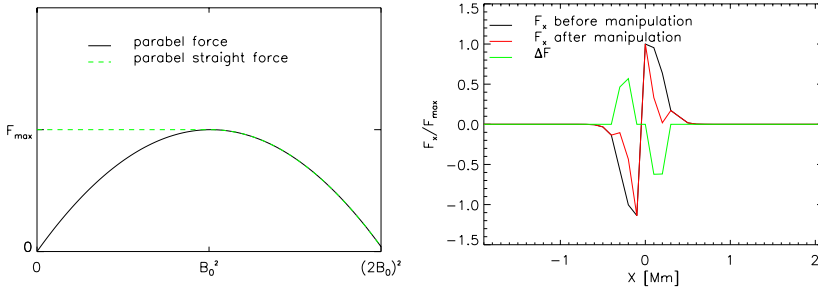


Figure 5.1: left: illustration of dependence of modified Lorentz force component ΔF_{Lx} (F_{px} component in equation 5.1) on the magnetic field strength. right: The Lorentz force in x-direction for an example case before manipulation (black line), after manipulation (red line) and ΔF_{Lx} (green line) itself. The sunspot center is at the zero point of the horizontal coordinate.

5.3.3 Results and Discussion

The effect an additional force at the lower boundary has on the simulation run compared to the unmodified reference case, is depicted in Figure 5.2. It shows the vertical magnetic field strength in kG at the lower boundary along one horizontal direction, where the zero point indicates the center of the sunspot. The different colors indicate the three different simulation runs, the dark blue line shows the simulation with a modulated Lorentz force F_{ps} , the light blue dashed line shows the same for a modulated F_p and the black line points out the reference case without any Lorentz force

manipulation. On the left side of the figure, the situation is depicted 34 min after the additional force was switched on, while on the right hand side the situation is shown after 109 min. First of all, there seems to be exactly no difference between the two different force implementations. Secondly, in the picture on the left, it can be seen that the sunspot simulation with an additional modulation force, the vertical magnetic field gets compressed to higher values than found in the reference case. But as the simulation continues, the vertical magnetic field in the simulation run with the additional modulation force spreads out almost as much as the magnetic field in the reference case. This can be better understood when looking at Fig. 5.3. It shows the vertical magnetic field strength at the horizontal layer in 10 Mm depth, where the Lorentz force modulation is done. This figure shows from top to bottom an evolution in time, on the left hand side for the reference case and on the right hand side for the case where Lorentz force is manipulated. As seen at the top level, 9 min after implementing the force, the magnetic field is compressed to higher field strength than in the reference case. But after only 28 min of simulation time, the first of this magnetic field bundles is already starting to move outwards along the x-direction. This is continued after 30 min simulation time. During the simulation run with the modulated Lorentz force implemented, this happens more frequently than in the reference case. The reason for this behavior is the following. Initially the modulated Lorentz force amplifies the magnetic field strength, but this amplification process stops when the threshold field strength is reached, for which the Lorentz force modulation goes to zero again. The magnetic field bundles are then free to move around. When floating around in y-direction they sometimes come close enough to each other to feel their strongly repelling force and they get a kick in x-direction. This behavior actually slightly enforces the disruption of the sunspot at the lower boundary compared to the reference case due to the higher magnetic field strengths present there.

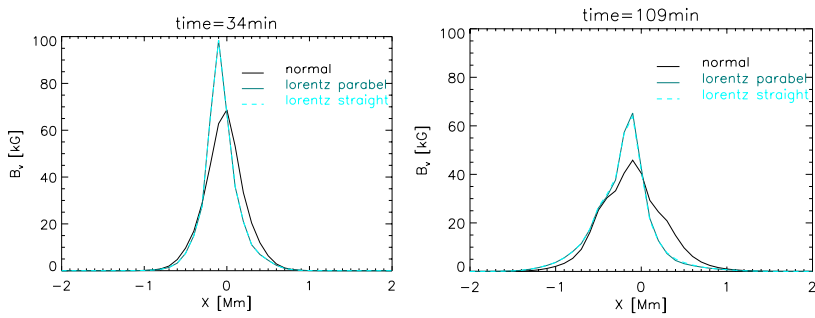


Figure 5.2: vertical magnetic field [kG] at the bottom boundary of the sunspot along one horizontal direction for the different simulations after 34 min (left) and 109 min (right). The zero point indicates the center of the sunspot

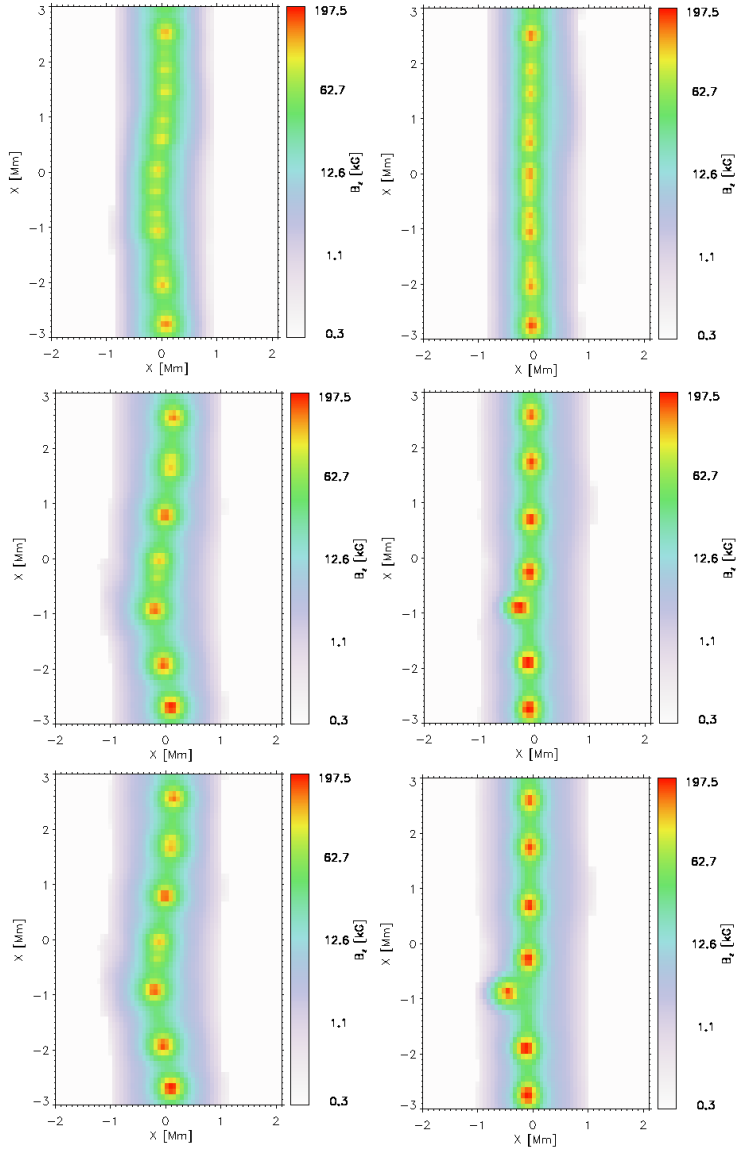


Figure 5.3: temporal evolution of vertical magnetic field at the bottom boundary for the reference case (left) and the case where an additional Lorentz force is implemented (right) for 9 min (top), 28 min (middle) , 30 min (bottom) after the force at the bottom boundary was implemented

5.4 WHAT CAUSES A SUNSPOT TO HAVE A PENUMBRA?

It is known from observations, that active regions emerge first as pores, which in some cases later develop into sunspots containing penumbras (Zwaan 1992). The smallest sunspots having primitive penumbras have fluxes of $2 \cdot 10^{20}$ Mx and radii of only 1.8 Mm, but there are as well examples of pores which survive to radii up to 3.5 Mm and magnetic fluxes of $7 \cdot 10^{20}$ Mx. This means there is a regime of magnetic fluxes and radii for which both pores and sunspots exist, though most of the pores with $R > 2$ Mm develop a penumbra (Bray 1964).

To understand under which circumstances a sunspot gets a fully developed penumbra and when it stays a pore, is not only interesting from a basic physics point of view. Total solar irradiance reconstructions use total sunspot areas and assume a constant penumbra/umbra ratio (Foukal & Lean 1990). If this assumption is not valid, there might be consequences for solar cycle theory, solar irradiance reconstruction and for the penumbra formation theory. Hathaway (2013) found a systematic variation of the penumbra area matching the 100 year Gleissberg cycle. This variation mainly affects smaller sunspot groups, where the penumbra area varies by a factor of two according to their measurements. If this variation is not due to observational errors, it can not be easily understood, since for smaller sunspots there are usually not many nearby sunspots influencing its field inclination. Therefore it would be good to have a more profound theoretical understanding of the conditions under which a penumbra forms and on what its horizontal extension depends. Simon & Weiss (1970), Spruit (1976), Simon et al. (1983) had developed pore models which assume that as soon as the magnetic flux increases, the magnetic field gets more inclined towards the vertical and finally forms a penumbra. Rucklidge et al. (1995) assume that at some critical magnetic field inclination and some critical radius, any perturbation of the pore leads to the formation of a penumbra because then its the only stable solution. Liu et al. (2005), Deng et al. (2005), who observed changes in penumbral structure associated with solar flares, proposed that the coronal magnetic field overlying sunspots has a potential feedback on the penumbra structure. Furthermore Shimizu et al. (2012) had detected a chromospheric precursor of penumbra formation. Another possibility is that the formation of a penumbra could be triggered by perturbations of the magnetic field in the subsurface of the sunspot. That the subsurface structure of a sunspot can not be imagined as a rigid, stiff magnetic flux tube is also indicated by observations, which show that larger sunspots are moving around a bit in longitude and latitude (Gizon et al. 2009, Gizon et al. 2010) before they stabilize at a certain position which can take a few days (Mazuccconi et al. 1990). The observed settling process is often interpreted as notion of anchoring in deep layers (Moradi et al. 2010).

The formation of a penumbra in simulations

Heinemann et al. (2007) were able to get filamentary structures of very reduced length and to detect signatures of the Evershed effect in their simulation of a sunspot-stripe. This has also been seen in a similar simulation of a sunspot stripe performed by Rempel et al. (2009b). Sunspot simulations by Rempel et al. (2009a), Rempel (2011a) indicate, that an elongated penumbra evolves in the case of a nearby sunspots of opposite polarity. An elongated penumbra also evolves in single sunspot simulations with a potential field, which has been modified towards the horizontal, reaching an inclination angle of over 65° against the vertical, compared to the unmodified case reaching an inclination of only 50° Rempel (2012). But in the same sunspot with an unmodified potential field only a very much shortened penumbra evolves.

5.4.1 Does a perturbation of the magnetic field in convection zone trigger the formation of a penumbra in the photosphere?

In this chapter it was investigated, if a perturbation of the magnetic field deeper down in the convection zone could trigger the formation of a penumbra in the photosphere. To test this hypothesis, we took the same sunspot simulation set-up as described in Section 5.3.2. This simulation was ran for two different cases. One is the unmodified reference run, also used in Section 5.3, while for the other simulation run, the reference run was taken after 33 min of simulation time and an additional force, acting on 6 Mm depth below the photosphere, was switched on. Both runs lasted for 120 min.

5.4.2 Perturbation force description

The force implemented, is very similar to the modification of the Lorentz force described in Section 5.3 and in equation 5.1. But in this case, the modified force is not implemented at the lower boundary, but at 6 Mm depth. Therefore we calculated F_{Lx} as described in equation 5.1 for the corresponding values of F_{max} and $B_0=27$ kG at this depth level, and modulated it with a periodic function in the other horizontal direction y as shown in equation 5.2.

$$\begin{aligned}
 F_{sin} &= \left(1 + \sin\left(\frac{2 \cdot \pi \cdot y}{4}\right)\right) & (5.2) \\
 \Delta F_{Penumbra} &= F_{sin} \cdot \Delta F_{Lx} \\
 F_{Lx} &= F_{Lx} - \Delta F_{Penumbra}
 \end{aligned}$$

5.4.3 Results and Discussion

The effect the ‘penumbra perturbation force’ acting at a depth of 6 Mm has on the simulation run compared to the unmodified reference case, is depicted in Figure 5.4. It shows the vertical magnetic field strength difference in kG between the simulation run with the ‘penumbra perturbation force’ and the one without the penumbra perturbation force at 6 Mm depth (top) taken 25 min after force implementation. The periodic perturbation of the vertical magnetic field can clearly be seen, and this signal has traveled to the photosphere within 25 min, as shown in the middle panel. The approximate Alfvén run time for this distance at the center of our sunspot is 19 min. At the bottom panel ΔB_z is shown for the photosphere 38 min after implementing the penumbra force. With respect to the middle panel, the magnetic field variations have clearly been amplified over time. Nevertheless looking at a bolometric intensity map for this instant of time, the two simulation runs look exactly the same, similar to the example given in Figure 5.5 b). One could expect that, if waiting long enough, the photospheric magnetic field would change further, and along with that some features seen in the bolometric intensity map would change as well compared to the reference case. But the penumbra perturbation force has just been implemented, after the sunspot had already evolved for 34 min, which means that the sunspot is already disrupting about 56 min after the implementation of the penumbra force (as can be seen in 5.5 c) and d)). This time is apparently too short to measure any significant differences in the evolution of sunspot features at the photosphere. Therefore for future investigations, one would need to test, if an amplification of the perturbation force would lead to the required modification of the sunspot appearance. However, one would additionally need a sunspot simulation, which survives for longer before it gets disrupted. Furthermore any dependence on the numerical resolution would have to be tested. It is feasible to run this simulation at least at double resolution and one would have to check for changes, in both the sunspot appearance in the reference simulation as well as in the one with perturbation force implemented.

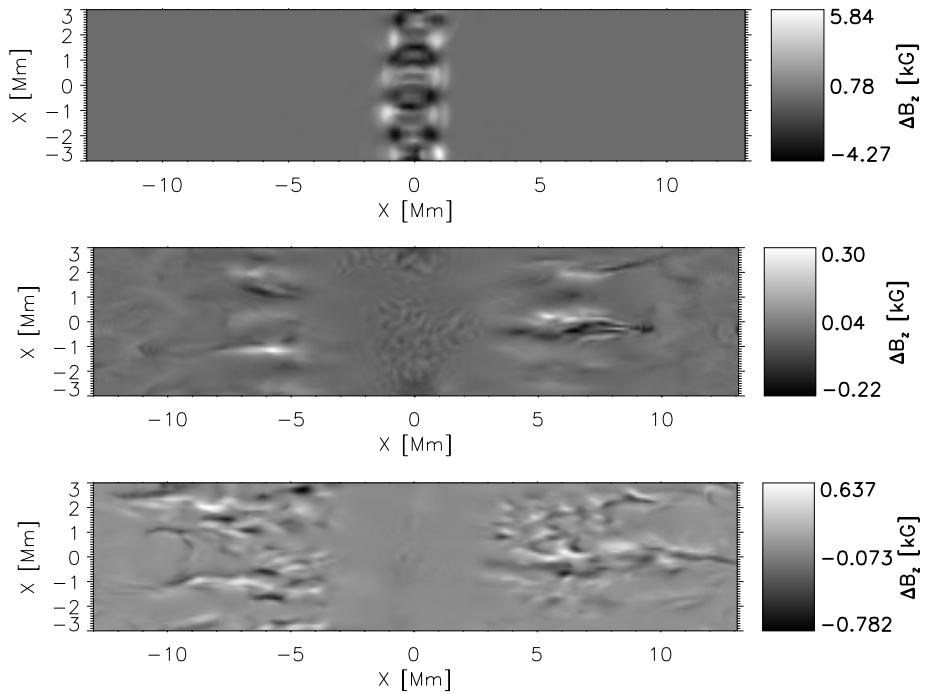


Figure 5.4: Vertical magnetic field strength difference ΔB_z in kG for simulation with ‘penumbra perturbation force’ minus simulation run without ‘penumbra perturbation force’. top: horizontal layer 6 Mm below the photosphere 25 min after penumbra force implementation; middle: photosphere 25 min after penumbra force implementation; bottom: photosphere 38 min after penumbra force implementation

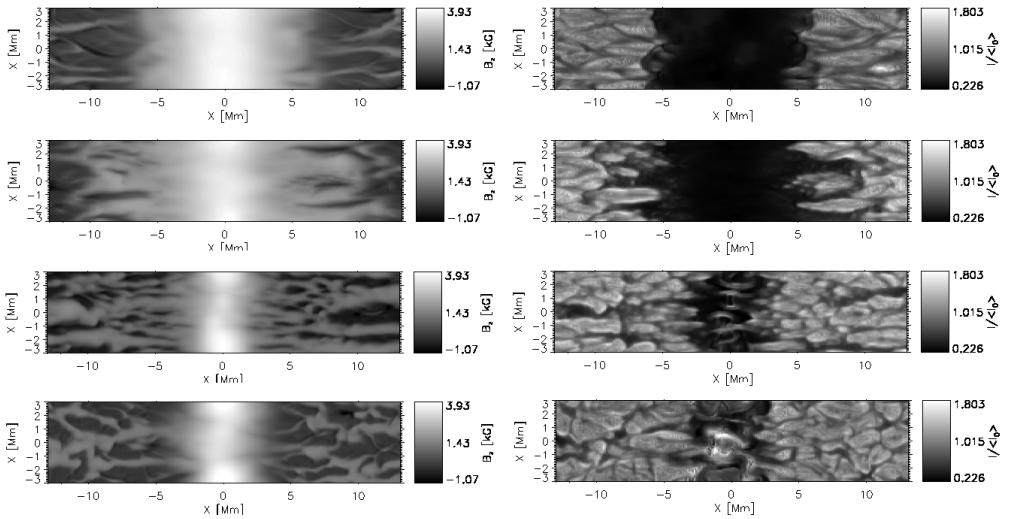


Figure 5.5: From top to bottom: temporal evolution of sunspot at the photosphere for simulation without ‘penumbra perturbation force’ after : a) 34 min b) 59 min c) 89 min d) 109 min simulation time. left: vertical magnetic field strength B_z in kG, right: bolometric intensity I normed over average intensity I_0

REFERENCES

- Babcock, H. W., 1963, *ARA&A*, 1, 41
- Bharti, L., Jain, R., Jaaffrey, S. N. A., 2007, *ApJ*, 665, L79-L82
- Beckers, J. M., 1977, *ApJ*, 213, 900-905
- Beckers, J. M., Schröter, E. H., 1969, *Sol. Phys.*, 10, 384-403
- Bercik, D. J., Nordlund, A., Stein, R. F., 2003, *ESA Special Publication*, 517, 201-206
- Bray, R. J., Loughhead, R. E., 1964, *Sunspots*
- Brummell, N. H., Tobias, S. M., Thomas, J. H., Weiss, N. O., 2008, 686, 1454-1465
- Caligari, P., Moreno-Insertis, F., Schussler, M. 1995, *ApJ*, 441, 886-902
- Cameron, R., Schüssler, M., Vögler, A., Zakharov, V., 2007, *A&A*, 474, 261-272
- Cowling, T. G., 1953, *Solar Electrodynamics*, ed. G. P. Kuiper, 532
- D'Silva, S., Choudhuri, A. R., 1993, *A&A*, 272, 621
- Deng, N., Liu, C., Yang, G., Wang, H., Denker, C., 2005, *ApJ*, 623, 1195-1201
- Duvall, T. L., D'Silva, S., Jefferies, S. M., Harvey, J. W., Schou, J., 1996, *Nature*, 379, 235-237
- Gizon, L., Schunker, H., Baldner, C. S., Basu, S., Birch, A. C., Bogart, R. S., Braun, D. C., Cameron, R., Duvall, T. L., Hanasoge, S. M., Jackiewicz, J., Roth, M., Stahn, T., Thompson, M. J., Zharkov, S., 2009, *Space Sci. Rev.*, 144, 249-273
- Gizon, L., Schunker, H., Baldner, C. S., Basu, S., Birch, A. C., Bogart, R. S., Braun, D. C., Cameron, R., Duvall, T. L., Hanasoge, S. M., Jackiewicz, J., Roth, M., Stahn, T., Thompson, M. J., Zharkov, S., 2010, *Space Sci. Rev.*, 159, 257-258
- Foukal, P. & Lean, J., 1990, *Science*, 247, 556-558
- Galsgaard, K. & Nordlund, A., 1996, *Journal of Geophysical Research*, 101, 13445-13460
- Gustafsson, B., 1973, *Uppsala Astron. Obs. Ann.*, 5
- Harvey, K., Harvey, J., 1973, *Sol. Phys.*, 28, 61-71
- Hathaway, D. H., 2013, *Sol. Phys.*, 286, 347-356
- Heinemann, T., Nordlund, Å., Scharmer, G. B., Spruit, H. C., 2007, *ApJ*, 669, 1390-1394
- Kitiashvili, I. N., Kosovichev, A. G., Wray, A. A., Mansour, N. N., 2010, *ApJ*, 719, 307-312
- Leighton, R. B., 1969, *ApJ*, 156, 1
- Lites, B. W., Skumanich, A., Scharmer, G. B., 1990, *ApJ*, 355, 329-341
- Liu, Y., 2005, in *NATO ASIC Proc. 375: Sunspots. Theory and Observations*, ed. J. H. Thomas & N. O. Weiss, 75-100
- Martínez Pillet, V., 2000, *A&A*, 361, 734-742
- Mazzucconi, F., Coveri, C., Godoli, G., 1990, *Sol. Phys.*, 125, 269-276
- Meyer, F., Schmidt, H. U., 1968, *Mitteilungen der Astronomischen Gesellschaft Hamburg*, 25, 194
- Meyer, F., Schmidt, H. U., Weiss, N. O., 1977, *MNRAS*, 179, 741-761

- Moradi, H., Baldner, C. , Birch, A. C., Braun, D. C., Cameron, R. H., Duvall, T. L., Gizon, L. , Haber, D. , Hanasoge, S. M., Hindman, B. W., Jackiewicz, J., Khomenko, E., Komm, R., Rajaguru, P., Rempel, M., Roth, M., Schlichenmaier, R., Schunker, H., Spruit, H. C., Strassmeier, K. G., Thompson, M. J., Zharkov, S., 2010 ,Sol. Phys., 267, 1-62
- Nordlund, A., 1982,A&A, 107, 1-10
- Parker, E. N., 1979, ApJ, 234, 333-347
- Rempel, M., Schüssler, M., Cameron, R. H., Knölker, M., 2009a, Science, 325, 171
- Rempel, M. , Schüssler, M., Knölker, M., 2009b, ApJ, 691, 640-649
- Rempel, M., 2011a, ApJ, 729, 5
- Rempel, M., 2011b, ApJ, 740, 15
- Rempel, M., 2012, ApJ, 750, 62
- Rimmele, T. R., 1994, A&A, 290,972-982
- Rimmele, T. R., 2004,ApJ, 604,906-923
- Rimmele, T., 2008, ApJ, 672, 684-695
- Roupe van der Voort, L. H. M., 2003, A&A, 397, 757-764
- Rucklidge, A. M., Schmidt, H. U., Weiss, N. O., 1995, MNRAS, 273, 491-498
- Sanchez Almeida, J., Lites, B. W., 1992, ApJ, 398, 359-374
- Schlichenmaier, R. Jahn, K., Schmidt, H. U., 1998, A&A, 337, 897-910
- Schlichenmaier, R., Solanki, S. K., 2003, A&A, 411, 257-262
- Schmidt, W., Hofmann, A., Balthasar, H., Tarbell, T. D., Frank, Z. A., 1992, A&A, 264, L27-L30
- Schüssler, M., Vögler, A., 2006, ApJ, 641, L73-L76
- Schüssler, M., 1984,A&A, 140, 453-458
- Schüssler, M. & Rempel, M., 2005, A&A, 441, 337-346
- Sheeley, Jr., N. R., 1969, Sol. Phys., 9, 347-357
- Shimizu, T., Ichimoto, K., Suematsu, Y., 2012,ApJ, 747, L18
- Shine, R. A. , Title, A. M., Tarbell, T. D., Smith, K., Frank, Z. A., Scharmer,G., 1994, ApJ, 430, 413-424
- Simon, G. W. & Weiss, N. O., 1970, Sol. Phys., 13, 85-103
- Simon, G. W., Weiss, N. O., Nye, A. H., 1983, Sol. Phys., 87, 65-75
- Skartlien, R., 2000, ApJ, 536, 465-480
- Socas-Navarro, H., Martínez Pillet, V., Sobotka, M., Vázquez, M., 2004, ApJ, 614, 448-456
- Spruit, H. C., 1976, Sol. Phys., 50, 269-295
- Spruit, H. C., 1981,Space Sci. Rev., 28, 435-448
- Spruit, H. C., Roberts, B., 1983, Nature, 304, 401-406
- Spruit, H. C. & Scharmer, G. B., 2006, A&A, 447, 343-354
- Thomas, J. H., Weiss, N. O., Tobias, S. M., Brummell, N. H., 2002a, Astronomische Nachrichten, 323,383-386

- Thomas, J. H., Weiss, N. O., Tobias, S. M., Brummell, N. H., 2002b, *Nature*, 420, 390-393
- Title, A. M., Frank, Z. A., Shine, R. A., Tarbell, T. D., Topka, K. P., Scharmer, G., Schmidt, W., 1993, *ApJ*, 403, 780-796
- Weiss, N. O., Thomas, J. H., Brummell, N. H., Tobias, S. M., 2004, *ApJ*, 600, 1073-1090
- Westendorp Plaza, C., del Toro Iniesta, J. C., Ruiz Cobo, B., Martínez Pillet, V. , Lites, B. W., Skumanich, A., 2001a, *ApJ*, 547,1130-1147
- Westendorp Plaza, C., del Toro Iniesta, J. C., Ruiz Cobo, B., Martínez Pillet, V., 2001b, *ApJ*, 547, 1148-1158
- Zwaan, C., 1992, in *NATO ASIC Proc. 375: Sunspots. Theory and Observations*, ed. J. H. Thomas & N. O. Weiss,75-100

Samenvatting¹

Het proefschrift onderzoekt een viertal problemen betreffende de magnetohydrodynamika van het zonsoppervlak. In het kort gaat het over: het effect van magneetvelden op de helderheid van de zon, over de manier hoe het magneetveld dat in de loop van de zonnecyclus aan het oppervlak verschijnt weer verdwijnt, de vraag of er naast de zonnevlekkencyclus ook nog een kleinschalige ‘lokale’ dynamo aan het oppervlak actief is, en tenslotte de vraag waarom sommige zonnevlekken een penumbra hebben en andere alleen een losse umbra.

Alle vier zijn vragen die niet met eenvoudige fysische modelletjes te beantwoorden zijn, zeker niet als het om kwantitatieve antwoorden gaat. En ook niet met analytische oplossingen van wiskundig behandelbare vergelijkingen, zoals die in de begintijd van de MHD bekend zijn geworden bij algemenere vragen als golfvoortplanting en stabiliteit van magneetvelden.

Het zonsoppervlak is in principe een ideaal voorbeeld van het gedrag van magneetvelden in de astrofysika: een hoop verschillende verschijnselen die in groot detail bekeken kunnen worden (vlekken, vlammen, protuberansen, plages, spikulen ...). ‘Solar dermatology’ werd dit graag buiten de zonnefysika genoemd. De geïmpliceerde vraag was: wat is het doel ervan, en wanneer gaan we dat bereiken? Het antwoord was tientallen jaren lang steeds hetzelfde: ‘de zon als laboratorium’ dat de fysische verklaringsaanpak leverde die we voor verschijnselen elders in het heelal dringend nodig hebben. Gezien de zeer uiteenlopende kwaliteit van de modellen in de zonnefysika had dit argument erbuiten weinig overtuigingskracht². Wel voldoende overigens om financiering van het zonsonderzoek zelf op gang te houden.

In de afgelopen ca 10 jaar is deze situatie sterk veranderd, zozeer dat de door de zonnefysici geïmpliceerde belofte nu werkelijk ingelost begint te worden. Dit is het gevolg van twee min of meer toevallig convergerende ontwikkelingen. De belangrijkste is wel de ontwikkeling van ‘realistische 3-D radiatieve MHD simulaties’, door het werk van vooral Åke Nordlund van de afgelopen 30 jaar. De claim van deze simulaties is dat alle relevante fysika er korrekt in zit, en het ruimtelijk oplossend vermogen

¹ (Geschreven in de niet-reaktionaire spelling van 1960-1996).

² Zo weinig dat ten tijde van Chandrasekhar als editor van ApJ het tijdschrift Solar Physics werd opgericht (door Kees de Jager) om een redelijke acceptance ratio te kunnen garanderen.

ervan voldoende is voor directe, kwantitatieve vergelijking met de waarnemingen, zonder ‘parameter tweaking’. Dat is een sterke claim, die om wat uitleg vraagt. Al eerder had Nordlund laten zien dat hydrodynamische simulaties met deze opzet (dwz zonder magneetveld) konvektie in sterren als de zon nauwkeurig kunnen reproduceren (in de orde van $\sim 1\%$, afhankelijk van de te verklaren grootte). De effectieve temperatuur van de zon bijvoorbeeld is korrekt tot ongeveer 70 K, en de granulatie ziet er zo goed uit dat ook de meest ervaren waarnemer het verschil niet vast kan stellen. Tegelijkertijd is het oplossend vermogen van de waarnemingen zo veel beter geworden ($\sim 0''.1$) dat directe vergelijking met deze simulaties mogelijk is. Dit succes is echter ook het gevolg van een bijzondere omstandigheid die niet bij veel andere astrofysische problemen optreedt. De konvektie aan het oppervlak van sterren als de zon wordt namelijk vrijwel volledig bepaald door koelingsprocessen die direkt rond het oppervlak plaatsgrijpen³. Om de effectieve temperatuur van de zon te reproduceren hoeft de simulatie niet dieper dan tot ca. 6 Mm onder het oppervlak te gaan. Dit geldt ook nog voor essentiële aspecten van de magnetische verschijnselen waar het in dit proefschrift over gaat. Het geldt echter niet meer voor dingen die veel dieper in de zon plaatsgrijpen. De vlekken-cyclus te reproduceren met dezelfde mate van fysisch realisme (waarom 11 jaar, waarom in de vorm van zonnevlekken?) is bijvoorbeeld voor de komende eeuw nog volstrekt ondenkbaar.

De succesvolle convergentie van simulatie en waarneming bij een zo complex fysisch systeem is psychologisch van niet te onderschatten belang. Het betekent namelijk dat zowel ons begrip van de onderliggende fysika als de methoden voor numerieke MHD kwantitatief korrekt zijn, en bovendien de waarnemingen nauwkeurig genoeg voor zinvolle vergelijking.

Door jarenlange ervaring met de magnetische zon is expertise in theoretische magnetohydrodynamika opgebouwd die op hoog nivo staat in vergelijking met andere gebieden in de astrofysika. Dit blijkt bijzonder nuttig bij het formuleren van zinvolle MHD simulaties en de interpretatie van de resultaten ervan. Het gebruik van astrofysische ‘general purpose’ MHD programmas zonder deze achtergrond leidt vaak tot teleurstellingen⁴.

De helderheid van de zon

Achtergrond en motivatie van dit deel van het proefschrift is de waarneming dat de helderheid van de zon een beetje met de vlekken-cyclus varieert. De maat die hiervoor in het klimaatonderzoek gebruikt wordt heet Total Solar Irradiance (TSI), de bolometrische energiestroom in de ekliptika op 1 AU van de zon. De TSI varieert met

³ Dit is niet helemaal intuïtief, het leidt ook nu nog tot aanzienlijk onbegrip in de literatuur.

⁴ Om een kollega in Shanghai te citeren: “huh? I don’t know, we just use ZEUS.”

0.08% over de zonnecyclus. Hij is hoger tijdens maximum zonnevlekkenactiviteit dan bij minimum, ondanks het feit dat vlekken donker zijn. Dit komt omdat dat er een ook heel veel kleine, elk op zich weinig opvallende, magnetische structuren zijn die helderder dan gemiddeld stralen.

De verklaring hiervoor werd geleverd in het proefschrift van promotor Spruit⁵. Wat nauwkeuriger: de voorspelling was a) dat bijdrage van het magneetveld zelf van de kleine buisjes positief is, b) in de directe omgeving ($0'1$) negatief, en c) het netto effect positief (als de buisjes kleiner dan $\approx 0'5$ zijn, daarboven worden ze donker, als in zonnevlekken). Een aanname die daarbij gemaakt werd is dat de aanwezigheid van een buisje geen invloed heeft op de konvektieve stroming in zijn omgeving. Dit was een zwak punt, want uit waarnemingen van magnetisch actieve gebieden is bekend dat de granulatie er daar wat anders uitziet: granulen zijn kleiner, de vloeistofsnelheden wat lager. Nu is het juist deze konvektieve stroming die de door de fotosfeer uitgestraalde energie levert. Ook een kleine belemmering van het konvektieve transport zou een fors effect op de netto helderheidsbijdrage van de buisjes kunnen betekenen. Waarnemingen vanaf aardoppervlak hebben onvoldoende fotometrische stabiliteit om zulke effecten op de ruimtelijke schaal van granulen te meten, en space based metingen zijn wel stabiel genoeg maar hebben net niet genoeg ruimtelijk oplossend vermogen. Door de ontwikkeling van de laatste 10 jaar is het echter mogelijk geworden dit effect met numerieke simulaties te onderzoeken. Hoofdstuk 2 van het proefschrift beschrijft het resultaat: het belemmerende effect is aanwezig; het zelfs zo sterk dat de netto helderheidsbijdrage van het kleinschalige veld negatief zou moeten zijn. Met andere woorden het verkeerde resultaat.

Het antwoord is waarschijnlijk dat het effect op de konvektieve stroming wel degelijk korrekt berekend wordt, maar dat er er nog een bijdrage is die niet goed door het numerieke experiment gerepresenteerd wordt. En wel een bijdrage uit de chromosfeer. De beweging van magneetvelden aan het oppervlak leidt tot dissipatie van magnetische energie in de atmosfeer, die daar zichtbaar wordt in de spektraallijnen. De randvoorwaarde aan de bovenkant van de simulaties is niet op deze fysika berekend, omdat hij op een te lage hoogte in de atmosfeer is gezet. Dit is nodig omdat de simulatie anders bijna alle rekentijd voor de atmosfeer nodig zou hebben. Om dit beter te onderzoeken zijn andere berekeningen nodig, die speciaal aangepast zijn aan de fysika van de atmosfeer. Het idee dat de bron van de positieve bijdrage tot de TSI boven de continuüm fotosfeer ligt past overigens goed bij konklusies die waarnemers al eerder uit het spectrale verloop van de solar irradiance hebben getrokken (bijdrage tot TSI ligt vooral in het UV).

⁵ 1977, abstract: "small flux tubes such as are found in the quiet network act as little 'leaks' in the solar surface through which an excess heat flux escapes from the convection zone."

Terugtrekkende magneetvelden

In het verloop van de cyclus verschijnt een enorm aantal actieve gebieden aan het oppervlak, die allemaal een hoop magnetische flux bevatten. De maat die hier van belang is wordt in de literatuur de ‘unsigned flux density’ genoemd: het gemiddelde van de absolute waarde van de vertikale magneetveldkomponent $|B_z|$ over een zeker oppervlak, bijvoorbeeld de ruimtelijke oplossing van de waarnemingen. De waarnemers hebben al vroeg met verbazing vastgesteld dat de voortdurende eruptie van nieuwe flux niet tot de verwachte ophoping van magneetveld leidt. De flux verdwijnt weer. Bob Howard stelde (omstreeks 1980) vast dat nieuwe flux gemiddeld maar 10 dagen zichtbaar blijft. In anekdotische gevallen verdwijnt een van de twee polariteiten van een actief gebied van de ene op de andere waarneemdag. Er is kennelijk een zeer effectief proces aan de gang dat flux verwijdert, en dat dit op een zeer onopvallende manier doet. Vaak ziet het er uit alsof magnetische flux gewoon ter plekke (‘in situ’) verdwijnt, wat dus niet kan vanwege $\text{div } \mathbf{B} = 0$. Het proces moet een ‘canceling’ zijn (opheffing) van structuurtjes met positieve B_z tegen negatieve B_z . Bij waarnemingen met hoog ruimtelijk oplossend vermogen is hier iets van te zien: het blijkt dat de eigenlijke opheffing van flux op zeer kleine schaal in intergranulen plaats vindt, 0’3 of minder.

In de literatuur die zich bezig houdt met modellen voor de zonnecyclus wordt de verspreiding van magnetische flux over het zonsoppervlak geparametriseerd met ‘diffusiecoëfficiënten’ die het waargenomen magneetveld beschrijven als een 2-dimensionaal skalarveld op het zonsoppervlak⁶. De diffusiecoëfficiënten worden aangepast om bepaalde eigenschappen van de cyclus te reproduceren (butterfly diagram bijv.). Hiervoor is het nodig om het verschijnen van nieuwe flux aan het oppervlak van het fitting proces uit te sluiten. Want daar gebeurt het omgekeerde van diffusie: tegengestelde polariteiten, aan het oppervlak verschenen als een willekeurige kleinschalige mengeling van polariteiten, organiseren zich spontaan en zonder toedoening van externe snelheidsvelden in twee gescheiden gebieden van tegengestelde polariteit. Hiervoor is in de modellen een aparte kludge nodig, anders zouden nieuwe actieve gebieden meteen weer zelf-annihileren. Geknoei. Deze *konstruktieve* aanpak⁷ heeft een lange traditie, en is een vast onderdeel van theorieën van de zonnecyclus geworden.

Het ‘antidiffusieve’ proces waarmee nieuwe flux verschijnt is sinds Cowling (1953) begrepen: het is gewoon het opstijgen van een horizontale fluxbuis die daarbij een lus door het oppervlak maakt. Het verdwijnen van flux blijkt bij nader onderzoek niet binnen nieuwe actieve gebieden zelf plaats te vinden maar tussen de tegengestelde polar-

⁶ Hierin aangemoedigd door een traditie van astrofysische turbulentiemodellen van uitgesproken academische relevantie.

⁷ waarin het maken van modellen belangrijker is dan de houdbaarheidsdatum of plausibiliteit ervan. Dit in contrast met de analytische instelling waarbij het er om gaat vast te stellen wat het geval is en wat niet, maar die tot minder, en lastigere, publikaties leidt.

iteiten van naburige nieuwe gebieden. Voor een verklaring is het allereerst noodzakelijk het magneetveld als intrinsiek 3-dimensionaal te zien, visualiseerbaar als bestaand uit veldlijnen ‘zonder einde’. Wat er aan het oppervlak intuïtief als een 2-D verdeling van polariteiten uitziet is in werkelijkheid slechts een doorsnee door een 3-D spaghetti van veldlijnen die ergens in de diepte verankerd zijn.

In hoofdstuk 3 wordt dit aspect onderzocht: hoe hangt de snelheid waarmee naburige tegengestelde polariteiten elkaar aan het oppervlak ‘opheffen’ af van omstandigheden in dieper lagen? Hoe hangt het af van de verstreken tijd, en van de aanvankelijke ‘unsigned flux density’? In verband met de begrensde ruimtelijke schaal van dit probleem is het zeer geschikt voor de realistische radiatieve MHD simulaties die nu mogelijk zijn. Om het ‘verankerings’ effect te onderzoeken werden simulaties tot verschillende diepten onder het oppervlak gedaan. In tegenstelling tot onze verwachtingen kon er wat dit betreft geen duidelijk effect vastgesteld worden. Het vermoeden is dat verankerings effecten pas merkbaar worden in simulaties van aanzienlijk grotere horizontale afmeting dan met de beschikbare rekentijd mogelijk waren.

Wel werd een sterke afhankelijkheid van de aanvankelijke veldsterkte gevonden: de snelheid van opheffing neemt toe met de veldsterkte. In sommige modellen wordt de canceling beschreven als het gevolg van het konvektieve snelheidsveld in de granulatie, dat magneetvelden omlaag zou trekken. Dit past niet goed bij de effecten die dit snelheidsveld in waarnemingen en simulaties heeft. Het concentreert magneetveldlijnen in de intergranulen tot min of meer verticale bundels waar de stroming, parallel aan het veld, langs omlaag loopt. In het midden van de granulen kan er tussen tegengestelde polariteiten een horizontaal veld aanwezig zijn, maar daar is de konvektieve stroming omhoog, het tegengestelde van wat nodig is om het veld omlaag te transporteren. Dit konvektieve beeld past ook niet bij de gevonden afhankelijkheid van de veldsterkte. Een sterker veld oefent sterkere krachten uit en is moeilijker tegen de magnetische opwaartse kracht in omlaag te krijgen. De resultaten zijn eerder te verklaren als een gevolg van de magnetische krachten zelf: waar tegengestelde polariteiten aan het oppervlak bij elkaar liggen trekken ze elkaar op dezelfde manier aan als staafmagneetjes. Als ze eenmaal dicht genoeg bij elkaar liggen trekt de spanning in de veldlijnen zelf ze onder het oppervlak.

Een lokale dynamo aan het zonsoppervlak?

Naast de ‘fluxbuizen’ in een actief gebied, die een veldsterkte van 1-2 kG hebben wordt er nog een intrinsiek zwakkere component waargenomen (in de orde van 100 G), van gemengde polariteit en kleine lengteschaal (kleiner dan granulen). Het vermoeden bestaat dat dit een teken van een apart dynamo effect zou kunnen zijn dat in de buurt van het oppervlak werkt en onafhankelijk is van de vlekken cyclus. Dit zou passen

bij de waarneming dat deze magneetveldcomponent niet sterk met de cyclus lijkt te correleren. Dit is ook een probleem dat goed geschikt is voor realistische simulaties. In hoofdstuk 4 wordt een poging gedaan om vast te stellen of een lokaal dynamo effect waarschijnlijk is. Hierbij treden een aantal onverwachte verschijnselen op die ook elders in de astrofysische MHD opgedoken zijn. In de eerste plaats is dit een sterke afhankelijkheid van het magnetische Prandtl-getal Pr_m : de verhouding van viscositeit tot magnetische diffusiviteit. In plasmas als dat van de zonsatmosfeer is dit getal klein, in de orde van 10^{-5} . Uit simulaties van geïdealiseerde magnetische turbulentie is dynamo activiteit, dwz. de spontane groei van een kleinschalig magneetveld, tot nu toe alleen waargenomen bij relatief grote waarden van Pr_m , hoger dan $Pr_{mc} \approx 0.1$. De kritische waarde van Pr_m voor het optreden van een dynamo effect neemt af met toenemende snelheden (Reynolds getal Re), maar het is niet bekend hoe de astrofysische limiet van hoge Re en lage Pr_m er uitziet, omdat dit een extreem rekenintensieve limiet is.

Gezien deze theoretische onzekerheden is het goed mogelijk dat aanwezigheid van een dynamo nog van meer omstandigheden afhangt dan alleen van een Re en een Pr_m . Schüssler en medewerkers hebben als eerste deze vraag onderzocht met realistische simulaties voor de zon. Zij vonden dynamo activiteit voor de hogere waarden van Pr_m waar ook simulaties van andere systemen een dynamo vonden, maar zeggen niets over de interessantere lagere waarden van Pr_m . Het onderzoek in hoofdstuk 4 probeert hier antwoorden te vinden. De berekeningen werden ook hier te rekenintensief voor lage Pr_m , maar toonden wel het bestaan van een kritische waarde van Pr_m aan die afhankelijk is van de numerieke resolutie.

Een algemene konklusie uit deze experimenten is dat de magnetohydrodynamika zich ten opzichte van de mikroskopische dempingsprocessen anders gedraagt dan de gewone hydrodynamika. Daar is men eraan gewend dat makroskopische eigenschappen van turbulentie niet afhangen van de viscositeit die op de kleinste schalen werkt. In de MHD zou het wel eens kunnen zijn dat het optreden van een makroskopisch verschijnsel als een dynamo afhangt van de mikroskopische eigenschappen van het plasma! Dit probleem is intussen ook opgedoken in andere astrofysische settings, zoals magnetische turbulentie in akkretieschijven en in core kollaps supernovae.

De penumbra van een zonnevlek

Een van de spektakulaire successen van realistische radiatieve MHD simulaties betreft de fenomenologie van zonnevlekken. Heinemann et al slaagden er voor het eerst in een kleine zonnevlek te berekenen, en vonden een hele reeks verschijnselen die buitengewoon goed met de waarnemingen overeenkomen. Daaronder: het ontstaan van een Evershed-stroming, de inwaardse beweging van penumbrale filamenten, de

manier waarop de penumbra er uitziet afhankelijk van de gezichtshoek, tot en met de in waarnemingen met de Zweedse 1-m zonneteleskoop ontdekte ‘dark cores’ over de filamenten. Deze verschijnselen waren overigens in overeenstemming met de ‘gappy penumbra’ verklaring van Spruit en Scharmer van een paar jaar eerder. Intussen zijn door Rempel veel massalere simulaties (‘honderden megawatt-uur’) gedaan. Dit heeft indrukwekkende zonnevlekken geproduceerd, met maar een enkel opvallend verschil tegenover echte vlekken: de penumbra is te smal, de filamenten te kort. Dit liet zich alleen rechttrekken door een nogal artificieel manipuleren van de magnetische bovenrandvoorwaarde.

Het doel van de berekeningen die in hoofdstuk 5 beschreven worden was te onderzoeken wat de fysische oorzaak van de waargenomen lengte van filamenten is. Uitgangspunt daarbij was het vermoeden dat het niet zozeer van de bovenrand afhangt maar eerder van de veldconfiguratie op grotere diepte. Daardoor zou de oplossing van het raadsel ook een belangrijk aanknopingspunt gaan leveren voor de vraag wat een zonnevlek op grotere diepte bij elkaar houdt. Dit was het meest ambitieuze project voor het proefschrift, en moest in de koelkast gelegd worden toen duidelijk werd dat er een flink aantal experimenten bedacht zouden moeten worden die elk ook veel rekentijd zouden gaan vergen. Dit werk is niet tot het stadium van een ontwerp voor een tijdschriftartikel gevorderd, maar heeft wel een aantal interessante numerieke waarnemingen opgeleverd die in dit hoofdstuk beschreven worden.

Acknowledgements

Finishing my thesis makes me almost sentimental. It was a hard time in Munich. I had to learn to be ambitious and focused, as well as precise and patient with myself. Most of my thanks for that go to my supervisor Henk Spruit. I want to thank him for not stopping to care about my professional development, for his good advices, for his patience and for the very much inside views of the solar magnetic fields behavior he gave me. I would like to thank all my colleagues and friends who have made this time in Munich an enjoyable part of my personal life. Special thanks to Else for her support visits in my office and the chocolates. As well as to Sandra for all the nice conversations we had. To Karin for going running with me in the snow. And to our lunch group people Rob, Sandra, Jonas, Tomek, Zaz, Marcelo and Maxime for all the non-scientific fun conversations, which prevented me from losing touch to “normal life”. Thanks as well to Jesus for all the tea with lemon we had together and the cheer up conversations which came along with it. Thanks also to my Russian teacher Carola for all the breakfasts and dinners as well as the encouragement and empathy. Thanks to all my Austrian friends, especially to Alex, Chrisi, Eva, Elli, Lisa, Tatjana, Ferdi and Armin, who still haven't forgotten me, keep visiting me in Munich and phone me up. Special thanks as well to my parents, without them I would not be at MPA. Especially to my Mum for constantly supporting me over the years.

Irina Thaler
München, February 2014

